Molecular Simulation of Carbon Dioxide Adsorption for Carbon Capture and Storage

by

Craig M. Tenney

A dissertation submitted in partial fulfillment
of the requirements for the degree of
Doctor of Philosophy
(Applied Physics and Environmental Engineering)
in The University of Michigan
2009

Doctoral Committee:
      Associate Professor Christian M. Lastoskie, Chair
      Professor Raoul Kopelman
      Professor Walter J. Weber, Jr.
      Professor Steven J. Wright

If we knew what we were doing, it wouldn't be called research

— Albert Einstein

Acknowledgments

Special thanks go to...

Preface

The work described herein uses molecular simulation to study the adsorption of CO_2 and related chemical species onto heterogeneous, solid adsorbents in order to facilitate the developement of effective CO_2 emission reduction strategies, which are needed to reduce the chance of harmful global climate change. The specific goals of this work include: 1) improving understanding of adsorption onto heterogeneous, microporous solids to inform the development of future, engineered adsorbent materials, 2) evaluating the potential of novel, metal-organic framework adsorbents to capture CO_2 from fossil fuel power plants, 3) developing an efficient molecular simulation coal model suitable for studying CO_2 sequestration and enhanced methane recovery in unmineable coal seams, and 4) developing and advancing tools and methods needed for the study of adsorption in non-rigid materials.

The introductory chapter provides background information describing carbon capture and storage, metal-organic frameworks, coal, and molecular simulation. Subsequent chapters describe specific molecular simulation research pertaining to the goals described above. Each of these chapters begins with a brief summary of the work, provides details regarding the simulation methods used, and finishes with a presentation and discussion of the results. A concluding chapter summarizes the most important findings and suggests areas where further research is needed.

Table of Contents

List of Tables

List of Figures

Abstract

Capture of CO_2 from fossil fuel power plants and sequestration in unmineable coal seams are achievable methods for reducing atmospheric emissions of this greenhouse gas. To aid the development of effective CO_2capture and sequestration technologies, a series of molecular simulation studies were conducted to study the adsorption of CO_2 and related species onto heterogeneous, solid adsorbents.

To investigate the influence of surface heterogeneity upon adsorption behavior in activated carbons and coal, isotherms were generated via grand canonical Monte Carlo (GCMC) simulation for CO_2 adsorption in slit-shaped pores with several variations of chemical and structural heterogeneity. Adsorption generally increased with increasing oxygen content and the presence of holes or furrows, which acted as preferred binding sites.

To investigate the potential use of the flexible metal organic framework (MOF) $Cu(BF_4)_2(bpy)_2$ (bpy=bipyridine) for CO_2capture, pure- and mixed-gas adsorption was simulated at conditions representative of power plant process streams. This MOF was chosen because it displays a novel behavior in which the crystal structure reversibly transitions from an empty, zero porosity state to a saturated, expanded state at the "gate pressure". Estimates of CO_2 capacity above the gate pressure from GCMC simulations using a rigid MOF model showed good agreement with experiment. The CO_2 adsorption capacity and estimated heats of adsorption are comparable to common physi-adsorbents under similar conditions. Mixed-gas simulations predicted $CO_2/N_2$and CO_2/H_2selectivities higher than typical microporous materials.

To more closely investigate this gating effect, hybrid Monte-Carlo/molecular-dynamics (MCMD) was used to simulate adsorption using a flexible MOF model. Simulation cell volumes remained relatively constant at low gas pressures before increasing at higher pressure. Mixed-gas simulations predicted CO_2/N_2 selectivities comparable to other microporous adsorbents.

To study the molecular processes relevant to storage of CO_2 in unmineable coal seams with enhanced methane recovery, a representative bituminous coal was simulated using MD and a hybrid Gibbs-ensemble-Monte-Carlo/MD method. Simulation predicted a bulk

density of 1.24 g/ml for the dry coal, which compares favorably with the experimental value of 1.3 g/ml. Consistent with known coal properties, simulation models showed stacking of macromolecular graphitic regions and preferential adsorption of CO_2 relative to methane.

Chapter 1

Introduction

Atmospheric carbon dioxide CO_2 concentration is a significant driver of climate change, and anthropogenic emission of CO_2 to the atmosphere is recognized as a major contributor to potential global warming. The climate changes attendant with the accumulation of this greenhouse gas (GHG) in the atmosphere pose a long-term challenge to achieving energy sustainability, and significant reductions in CO_2 emission during the 21st century are needed to stabilize atmospheric GHG concentrations (Houghton et al., 2001). Increased international social and political concern about global warming are driving efforts to reduce anthropogenic CO_2 emissions. Although improvements in energy efficiency and a transition to renewable or low-carbon energy sources may ultimately slow the accumulation of greenhouse gases in the atmosphere, the time required to implement these technologies, the continued abundance of fossil fuels, and the significant investment in existing infrastructure ensure the continued use of fossil fuels for at least the next several decades. Hence, there is compelling incentive to develop feasible and cost-effective methods to curb CO_2 emissions through the capture and long-term sequestration of carbon in geologic or oceanic reservoirs. Anthropogenic emissions of CO_2 originate mainly from the combustion of fossil fuels, with approximately one third of the total coming from electric power generation (EIA Energy Information Administration, 2003; Aaron and Tsouris, 2005). Being large-scale point sources, these power plants are attractive candidates for engineered capture and sequestration of CO_2.

1.1   Carbon Capture and Storage

In carbon capture and storage (CCS), CO_2 is collected, concentrated and transported to a storage medium, where it is sequestered from the atmosphere for geologically long time

periods (Capehart, 2007). Figure 1.1 depicts several proposed capture and storage storage systems. To take advantage of economies of scale, CCS will be most effectively applied to large, stationary CO_2 point sources, such as coal- or gas-fired electric power plants. For nations such as the United States that possess abundant geological formations suitable for CO_2 storage, such as depleted oil and gas reservoirs, unmineable coalbeds, and deep saline aquifers, CCS is an effective near- to mid-term CO_2 emissions control strategy.
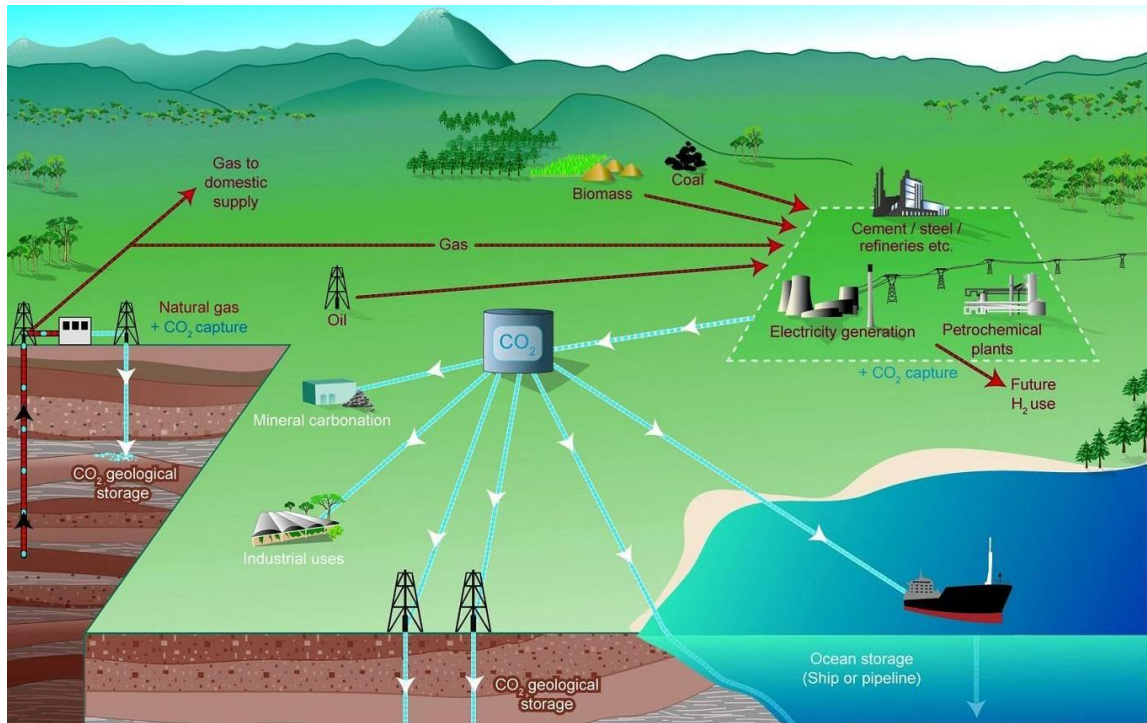
Figure 1.1   Possible carbon dioxide capture and storage systems. Adapted from Metz et al. (2005)

Current CO_2 separation technologies incur a cumulative energy penalty of 14–40%, depending on whether a pre-combustion or post-combustion approach is adopted (EIA Energy Information Administration, 2003). This represents 75–80% of the total cost of CCS (Herzog, 2001). This penalty is depicted in Figure 1.2, which shows that avoiding carbon dioxide emission requires increased energy input to the system. To make CCS economically viable, more efficient capture technologies are required. Mature technologies already exist for CO_2 transport and injection, as used for example in enhanced oil recovery and enhanced coalbed methane recovery. Rather, the main challenge to implementing CCS is the high cost of capturing and separating CO_2 from other process gases.

As depicted in Figure 1.3, CO_2 capture from power plants can generally be accomplished through two possible modes: post-combustion (e.g. CO_2 capture from flue gas in conventional power plants) and pre-combustion (e.g. CO_2 capture from syngas in IGCC plants). Unless fitted to operate with pure oxygen rather than air, which avoids the costly
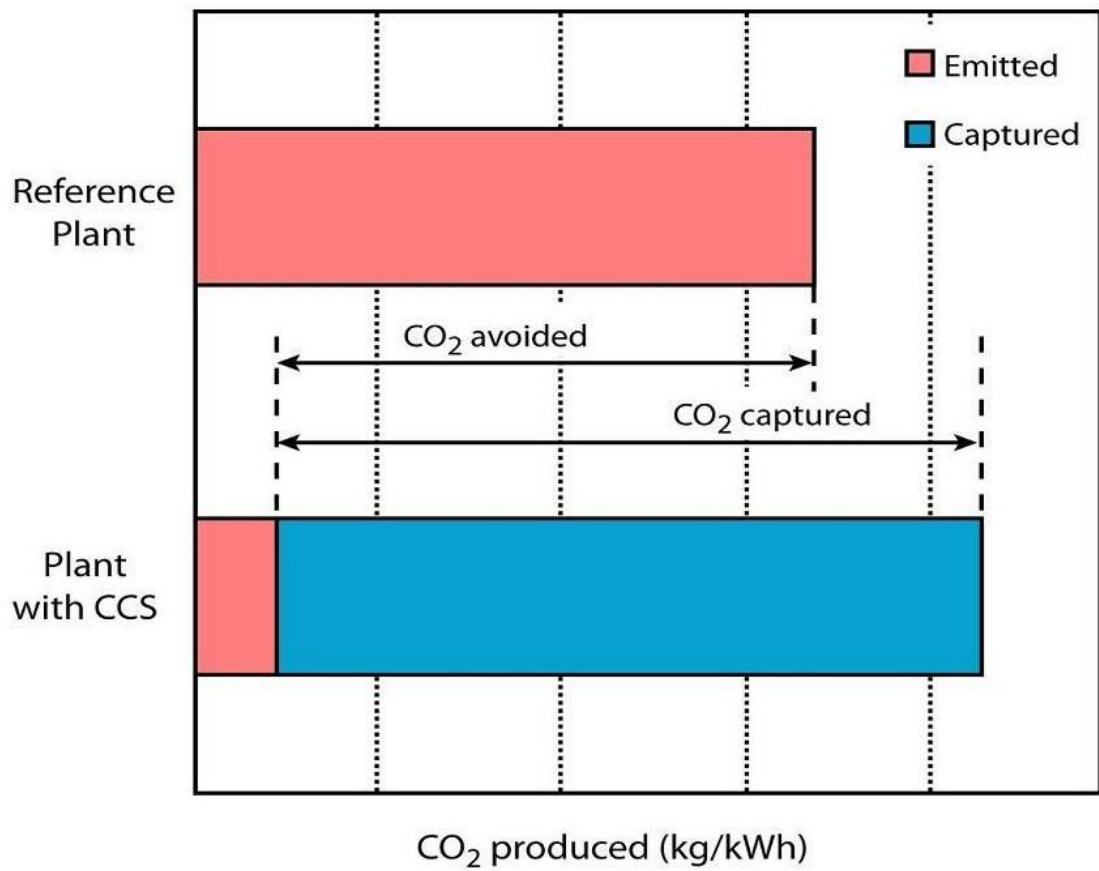
Figure 1.2 Loss of overall power plant efficiency as a result of carbon dioxide capture and storage. Adapted from Metz et al. (2005)

need to separate CO_2 from nitrogen but is a very expensive proposition overall, conventional power plants are restricted to post-combustion capture and separation. New gasification-based plants, however, have the option of either capture mode; and although conventional pulverized coal power plants produce cheaper electricity in the absence of CCS, more advanced IGCC plants may be cheaper when CCS is required (Metz et al., 2005), because CO_2 separation and capture is more efficient at the higher CO_2 pressures and concentrations found in an IGCC plant.
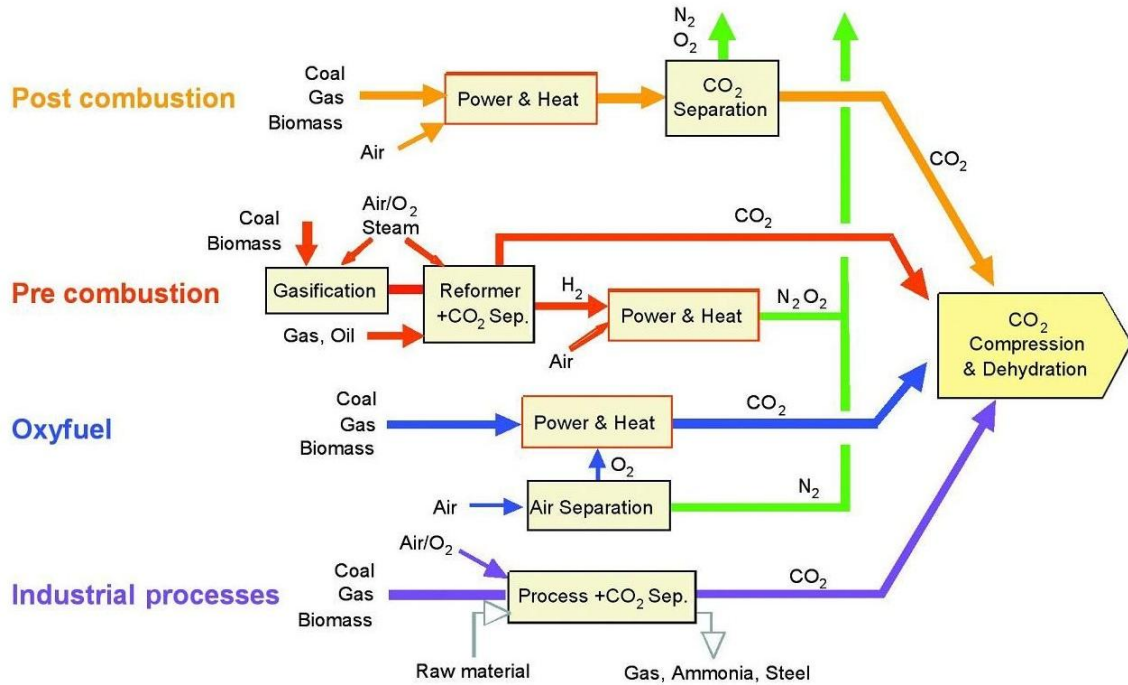
Figure 1.3 Overview of carbon dioxide capture processes and systems. Adapted from Metz et al. (2005)

Typical flue gas contains relatively low concentrations of CO_2 (5% for gas-fired plants, 15% for coal) at roughly atmospheric pressure and $\sim$400K after final cooling. This CO_2 must be concentrated to at least $\sim$95% CO_2 for efficient transport and storage. In an IGCC power plant, coal or natural gas are partially oxidized with pure oxygen to create a hydrogen-rich synthetic gas (syngas). In the case of coal, the syngas composition is approximately 15% CO_2, 46% CO and 35% H_2 by volume (Capehart, 2007). This syngas goes through conventional gas cleanup steps to remove undesired components, such as metals, alkalytes, ash and particulates. After this cleanup step the syngas can be reacted with steam in a shift reaction to convert CO to CO_2. Following cold-gas H_2S removal via absorption and prior to feeding to the gas turbine, the CO_2 can be removed from the syngas, which is now approximately 56% H_2 and 40% CO_2. Previous studies have shown that CO_2 can

4

be captured from a cool ($\sim$300–320K), high-pressure (2–8MPa) gas stream via physical absorption scrubbing, using for example Rectisol or Selexol (Capehart, 2007; Rie, 1998), but the process requires costly solvent regeneration and has corrosion problems.

Current methods for removal of CO_2 from process streams generally use chemical absorption into aqueous amine solutions. This is a well-understood and mature technology, but solvent regeneration requires very energy-intensive heating and cooling steps, and solvent degradation creates highly corrosive by-products that are harmful to process equipment (Aaron and Tsouris, 2005). Due to these problems with amine absorption, capture of CO_2 using selective membranes or adsorbent solids, which may use similar microporous materials to induce separation, have been proposed as potentially attractive alternatives. Because adsorption can perform well at low CO_2 concentrations ($<$2%) (Audus, 1997), adsorption could also be used as a final polishing step in a lower-cost, hybrid CO_2 capture system (Aaron and Tsouris, 2005). Efficient capture of CO_2 using adsorption requires solid adsorbents with high CO_2 selectivity and capacity and easy regenerability. Unfortunately, these desirable properties do not generally occur in tandem.

1.2   Metal-Organic Frameworks

Prior studies investigating microporous adsorbents have demonstrated selective adsorption of CO_2 over H_2 and N_2 (Goj et al., 2002; Akten et al., 2003). At this time, however, conventional high-performance commercial adsorbents (e.g. zeolites and activated carbon) cannot achieve sufficiently economic CO_2 separation for wide-scale implementation of CCS (Aaron and Tsouris, 2005). Fortunately, new classes of high-surface-area adsorbent materials are being developed that can potentially be tailored to provide improved performance under the desired conditions. Metal-organic-frameworks (MOFs) represent one of these new classes of advanced adsorbents. The self-assembled geometric structure of a MOF is characterized by vertices containing metal cations connected by edges composed of organic linker molecules. MOFs are of interest because their pore structure and chemistry can be tuned by changing the metal and organic building blocks used in their construction. The use of different vertex groups and linking molecules has led to the creation of literally hundreds of different MOFs with many exciting possibilities for specialized functionality. Adsorption behavior can vary significantly between different MOFs due to differences in pore size, structural arrangement, and surface functionality. In this study we focus on a novel, flexible, copper-based MOF, $Cu(BF_4)_2(bpy)_2$(bpy=bipyridine) (Blake et al., 1997), which is composed of stacked, 2-D layers and depicted in Figure 1.4.
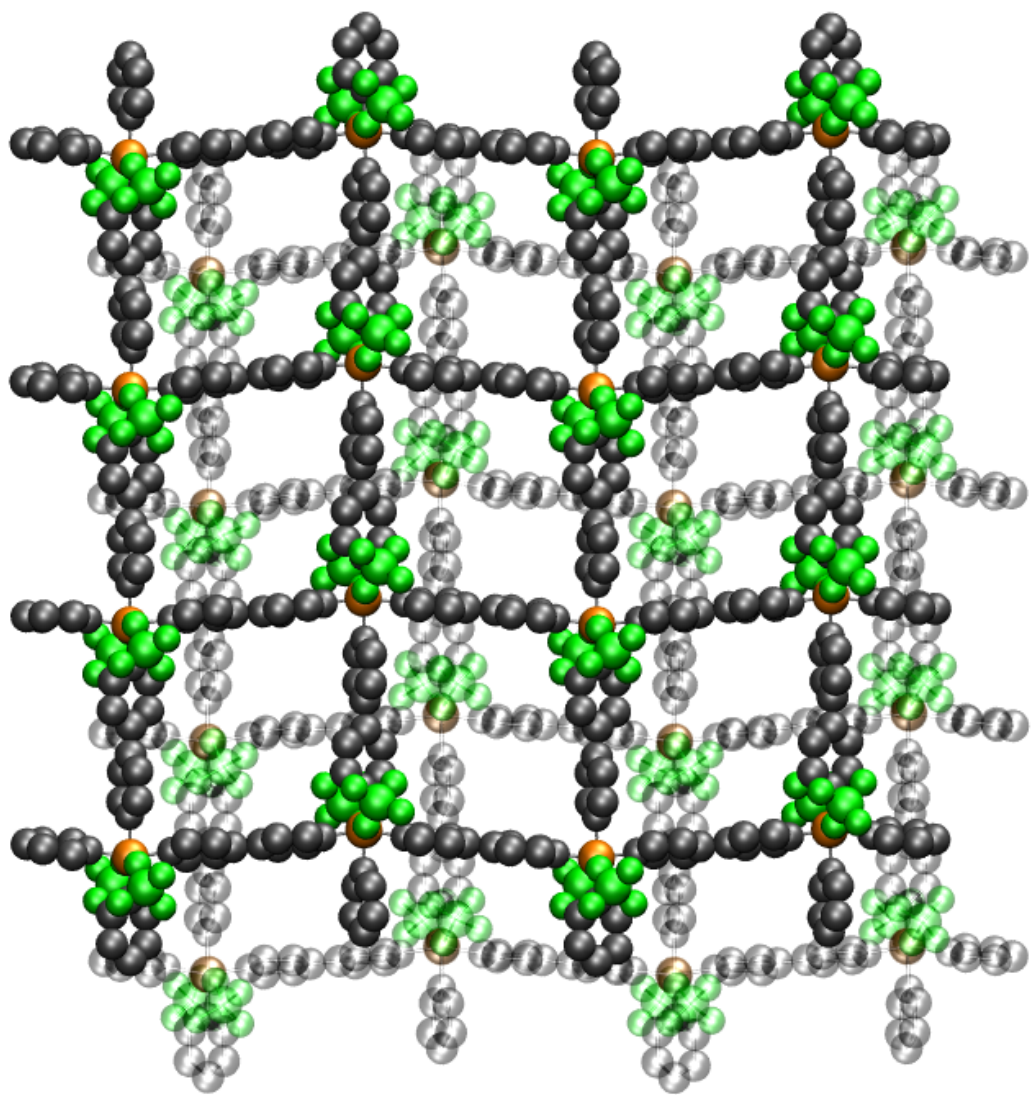
Figure 1.4 Top view of two 4x4 layers of $Cu(BF_4)_2(bpy)_2$ in its CO_2-expanded form (Kondo et al., 2006). The crystal structure repeats in all directions. The bipyridine linking units are shown in gray, BF_4 groups in green, and copper vertices in orange. CO_2 molecules are omitted for clarity.

$Cu(BF_4)_2(bpy)_2$ is particularly interesting because it undergoes abrupt, reversible transitions from an empty, collapsed, non-porous state to a filled, expanded, porous state at what has been termed the gate pressure. As seen in Figure 1.5, experimental CO_2 adsorption isotherms at 273K display this abrupt transition between zero and saturated adsorption at repeatable gate pressures of ~35kPa for adsorption and ~25kPa for desorption (Kondo et al., 2006; Li and Kaneko, 2001). This transition coincides with a structural rearrangement going from nonporous to porous mode, giving rise to the term latent porous crystal (LPC). This strong interaction with CO_2 suggested the LPC would have high selectivity for CO_2 over N_2 and H_2 and might be used for efficient separation of CO_2 from flue gas in conventional power plants or from syngas in IGCC systems. Figure 1.4 shows a top view of two, stacked 4x4 layers of the CO_2-expanded form of $Cu(BF_4)_2(bpy)_2$. Each layer of the crystal is offset relative to adjacent layers to allow nesting of the BF_4 groups into the pore spaces. As can be seen in the figure, there is a one-to-one relationship between the number of rectangular pore spaces and the number of Cu atoms. Above the gate pressure and at moderate pressures, each pore can contain up to two CO_2 molecules.

The abrupt gating transition of this latent porous crystal is unlike the sub-critical vapor-liquid phase transitions observed in other microporous adsorbents in that it is induced by rearrangement of the adsorbent structure rather than pore-size effects (Li and Kaneko, 2001). Gating behavior with $Cu(BF_4)_2(bpy)_2$ has also been observed experimentally for nitrogen, oxygen, methane, and argon adsorption (Noguchi et al., 2005; Onishi et al., 2002; Li and Kaneko, 2001). It has been simulated for nitrogen at 77K using Grand Canonical Monte Carlo (GCMC) techniques by manually varying the distance between the layers of a rigid $Cu(BF_4)_2(bpy)_2$ model structure (Ohba et al., 2006).

An ideal adsorbent would simultaneosly provide high capacity, high selectivity, and easy regenerability. Adsorbents with high capacity help to reduce equipment size and cost but often require high operating pressures to induce pore-filling. Selectivity can be enhanced by strong, adsorbate-specific interactions with the adsorbent structure, but this must be balanced against the need for easy regenerability, which is impeded by excessively strong bonding. Gating behavior may help lower regeneration costs by reducing the pressure and temperature changes required between adsorption/desorption cycles. Optimization of CO_2 capture processes requires choosing adsorbents with a proper balance of capacity, selectivity, and regenerability under specific conditions of temperature, pressure, and composition. Some engineered MOF adsorbents having comparatively high CO_2 adsorption capacities have been identified experimentally (Millward and Yaghi, 2005). In a comprehensive review and extended study, however, mixed agreement was found between simulated and experimental isotherms for hydrogen, methane, argon, and helium adsorption into several MOFs
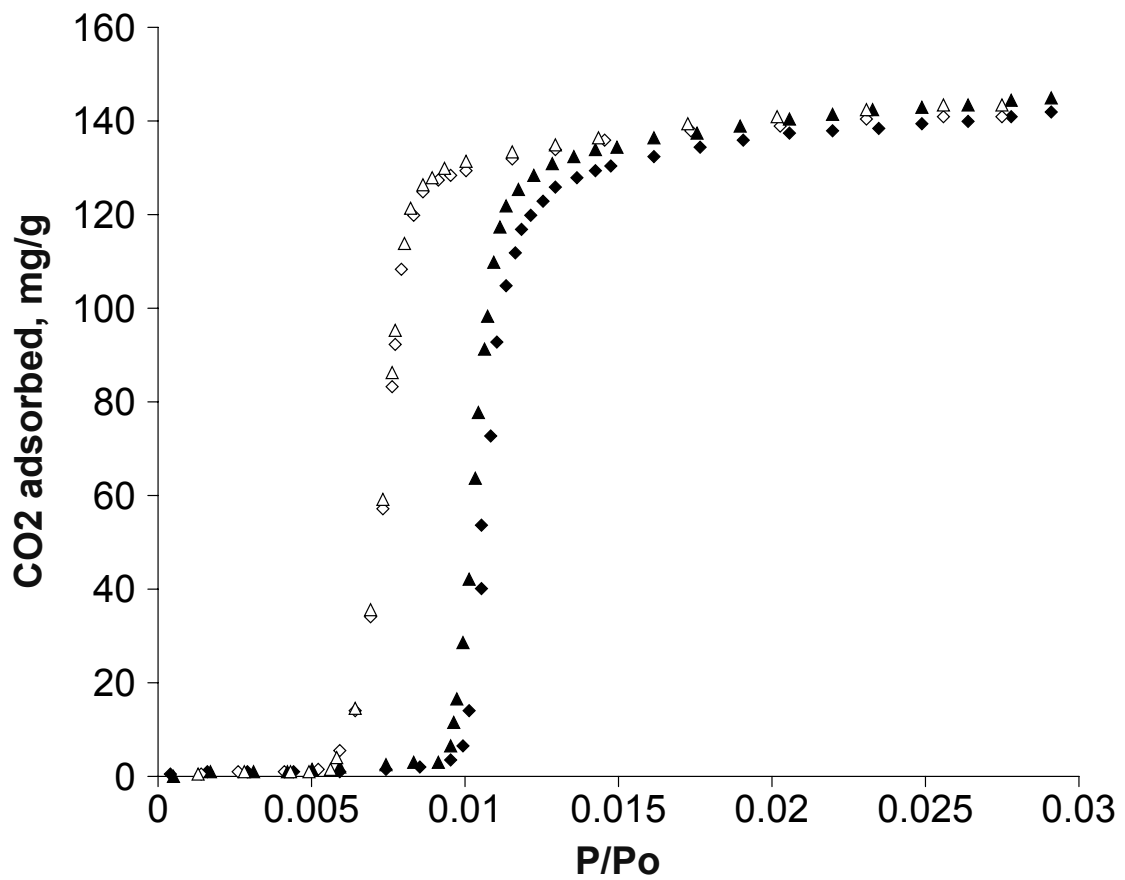
Figure 1.5 Adsorption (filled symbols) and desorption (open symbols) isotherms for $Cu(BF_4)_2(bpy)_2$ at 273K (Kondo et al., 2006; Li and Kaneko, 2001). Two adsorption-desorption cycles are shown ($\diamond$ and $\triangle$, respectively). Po is the carbon dioxide saturation vapor pressure.

(Garberoglio et al., 2005), indicating that our understanding of adsorption in MOF structures is not complete.

1.3 Coal

After capturing carbon dioxide, it must still be compressed and transported to its final storage location. Of the possible options for long-term sequestration of CO_2, deep saline aquifers will likely be most commonly used, because they are widespread, have massive storage capacity potential, and are expected to be generally safe and effective for long-term CO_2 storage. Figure 1.6 depicts carbon dioxide storage in saline aquifers and other possible geological formations. Of these other options, unmineable coal seams have received considerable attention, because they represent an opportunity to make a profit while doing environmental good.
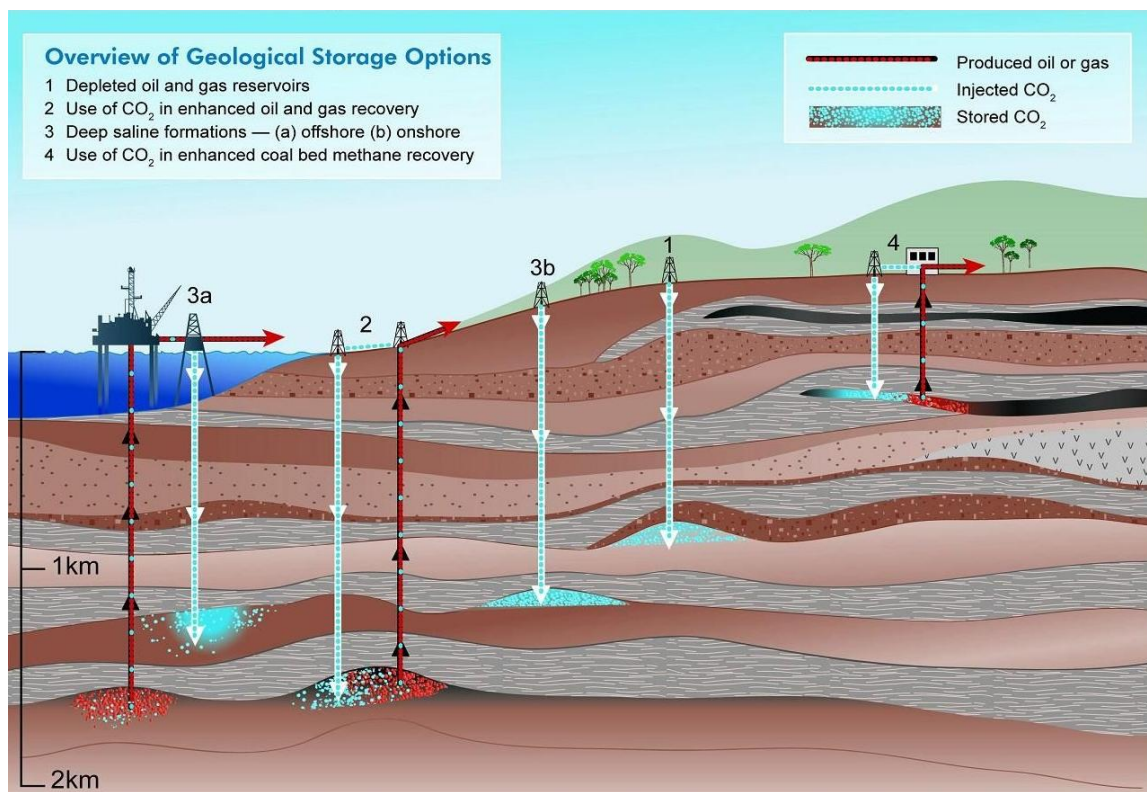
Figure 1.6 Methods for storing carbon dioxide underground in deep geological formations. Adapted from Metz et al. (2005)

Coal seams are an important geological reservoir for methane and carbon dioxide, two principal constituents of the global carbon cycle. There are multiple coal basins within the continental United States and around the world that are capable of storing significant

9

volumes of these greenhouse gases. Relative to other sequestration alternatives, long-term storage of CO_2 in unmineable coal seams is particularly attractive because it can be linked to enhanced extraction of methane, an economically valuable and relatively low-carbon fossil fuel (Gunter et al., 1997; Pashin and McIntyre, 2003). The propensity for fossil fuel-based power plants to be located in geological basins featuring such coal deposits has been identified as another factor favoring this sequestration strategy (Hitchon et al., 1999). Experiments and pilot studies using both pure CO_2 and flue gas have established that CO_2 readily displaces adsorbed methane from coal, significantly increasing coal bed methane yields compared to conventional methods (Pashin et al., 2001; Tsotsis et al., 2004; White et al., 2005). The worldwide coalbed capacity for CO_2 sequestration has been estimated to be 225 gigatons (White et al., 2005). However, the capacity estimates are uncertain due to assumptions regarding coal seam thickness and continuity, coal basin accessibility, and the CO_2 adsorption isotherm on coals.

It has proven difficult to quantify the capacity of coal adsorbents for methane and carbon dioxide storage, and to predict the selectivity for carbon dioxide sorption over methane in coal media. Coals are highly heterogeneous materials, both in physical and chemical terms, and coal matrices are known to undergo substantial swelling during the uptake of gases under pressurization. These characteristics have impeded the development of a fundamental understanding of the sorptive interactions of methane and carbon dioxide with coal media in geological settings.

A conceptual model for gas transport in coal seams has been propsed (Remner et al., 1984), in which methane extraction from a coalbed involves sequential rapid desorption from the ultramicropores of the coal matter; rate-limiting molecular diffusion to the surfaces of cleats (mm-scale cracks perpendicular to the bedding plane) within the coal matrix; and advective flow through the cleats to the production wells. Sequestration of carbon dioxide in coal seams is speculated to follow a similar sequence, only in reverse (Sams et al., 2005). To understand and predict the dynamics and the long-term fate of gases transported out of or sequestered into coal basins, therefore, one must consider adsorption and diffusion of these species within the macromolecular coal structure.

From several decades of investigation, a consensus description of the structure of coal has emerged (Marzec, 2002) in which coal is regarded as a glassy polymer mixture of largely insoluble macromolecules (1300-3500 amu) bound with smaller, more mobile substances (100-500 amu). Noncovalent associations within this coal framework can be disrupted by solvents, leading to plasticization and swelling, usually in the direction perpendicular to the bedding plane. Rearrangement due to swelling may also result in the expulsion of previously sorbed gases (Larsen et al., 1997). Coal solubility and swelling behavior varies with coal

rank and type (Karacan and Mitchell, 2003) and significantly impacts performance during extraction and injection operations.

X-ray diffraction of coals has revealed ~1 nm crystalline graphitic structures interspersed with amorphous regions (Lu et al., 2001). The extent of crystallization generally increases with rank. Coal exhibits porosity at all size scales, and multi-scale models are typically needed to describe diffusion processes (Tsotsis et al., 2004). Spatial heterogeneity in coal has been interrogated using X-ray computerized tomography (Karacan, 2003) and magnetic resonance imaging (Ramanathan and Bencsik, 2001).

Sorption experiments with confined coals (Karacan, 2003) have demonstrated that isotherm features, particularly capacity and selectivity, are dependent upon a plethora of factors including the coal rank, mineral content, temperature, pressure, moisture content, sample history and gas composition (Goodman et al., 2004). Coal densities and surface areas are lowest for mid-rank coals, and for some coal samples, the excess CO_2 isotherms display minima or negative values attributed to swelling at intermediate pressures (Krooss et al., 2002).

The Langmuir model is most frequently employed to mathematically represent methane and carbon dioxide sorption isotherms on coals, although other theory-based models have been suggested that include empirically-calculated volume-dependent terms (Ozdemir et al., 2003; Fitzgerald et al., 2003) to account for the effects of swelling and/or dissolution or simultaneous adsorption/absorption (Milewska-Duda et al., 2000). For estimation of the specific surface area and pore size distribution of adsorbents, disordered porous solids such as activated carbons and coals are frequently modeled as a collection of independent, noninterconnected slit pores with smooth, homogeneous graphitic surfaces (e.g. Lastoskie et al. (1993a,b, 1997); Quirke and Tennison (1996); Heuchel et al. (1999); Lastoskie and Gubbins (2000); Ravikovitch et al. (2000); Samios et al. (2000); Dombrowski et al. (2001); Dombrowski and Lastoskie (2002); Cao and Wu (2005)). Thermophysical properties inferred using such simplistic models for pure or mixed gas adsorption are unreliable for highly heterogeneous adsorbents (Dombrowski et al., 2000; Quirke and Tennison, 1996; Davies and Seaton, 1999; Heuchel et al., 1999; Sweatman and Quirke, 2001). For this reason, more complex models have been developed in an attempt to account for the structural and/or chemical heterogeneity of disordered porous solids (Lastoskie et al., 1994; Vishnyakov et al., 1998; Davies and Seaton, 1998; Lastoskie, 2000; Lastoskie and Gubbins, 2001; Schoen, 2002; Pikunic et al., 2002, 2003). Monte Carlo molecular simulation has been used in limited application to model sorption in coals represented as chemically homogeneous (Tsotsis et al., 2004) or heterogeneous slit-shaped carbon pores (Vishnyakov et al., 1998). Putative coal model microstructures have been assembled from compositional data on elemental and

11

functional group content, aromaticity, MS fragment analysis, and other measurable physical and chemical properties. A systematic methodology for the generation of representative coal microstructures has been proposed (Faulon et al., 1993; Faulon, 1994), but sorption simulations using these constructs are sparse (Takanohashi et al., 1999, 2000).

In addition to the uncertainty regarding the available storage volume for CO_2 in coal basins, a number of other knowledge gaps exist regarding the sequestration of carbon dioxide in coal seams. The long term fate and mobility of CO_2 injected into coalbeds is unknown; reinvasion of water into coal seams, for example, may dissolve stored CO_2 and lead to its migration back to the surface. Little information is available on the effects of sequestered CO_2 on coal mineral matter and indigenous microbiota, and whether methanogens may reduce the stored carbon dioxide to methane. To answer these questions, accurate measurements of CO_2 and methane isotherms, sorption selectivities, and diffusivities are required. However, such data are unexpectedly difficult to measure with precision, on account of the wide variability in the properties of coals, the effects of coal swelling and moisture content, and the solubility of low molecular weight, noncovalently-bound fractions of the coal macromolecule (White et al., 2005). Consequently, a wide range of estimated values have been reported for key properties such as the CO_2 surface area (110-425 m^2/g) (Mahajan, 1991) and CO_2/CH_4 sorption selectivity (1.9-5.3) (Mastalerz et al., 2004; Tsotsis et al., 2004). There is thus a strong motivation to use molecular modeling and simulation tools to investigate the fundamental interactions of carbon dioxide and methane with coal media, to impart new understanding of the mechanisms of adsorption of these gases on coal surfaces and to calculate important physicochemical properties (e.g. diffusion coefficients in coal matrices) that are difficult to obtain by direct experimental measurement.

1.4   Molecular Simulation

Modeling and simulation are complementary to experimental and theoretical analysis and play a critical role in understanding, characterizing, and developing adsorption systems. For example, using simulation, the potential of proposed but unsynthesized candidate structures can be screened without costly laboratory synthesis and adsorption measurements for underperforming materials. Further, identification via simulation of structural features and chemistries that yield adsorbents well-suited to particular conditions can help inform the rational development of new generations of engineered adsorbents specifically tailored for the desired application. Also, simulation can enable the study of phenomena that occur under conditions and at scales that are difficult to reproduce in a laboratory setting, such as

sorption and desorption in deep, unmineable coal seams.

Many of the results in this work were generated using grand canonical Monte Carlo (GCMC) simulation methods. GCMC simulations are characterized by constant system temperature, constant volume, and constant adsorbent chemical potential. Using the GCMC algorithm, random trial moves, which include molecule translations, rotations, insertions, and deletions, are accepted according to probabilistic rules that result in a distribution of states consistent with the grand canonical ensemble. Molecular dynamics (MD) methods were also used in some of this work. Unlike MC methods, which are characterized by random and generally local moves, MD steps are deterministic and global, calculating system evolution according to specific equations of motions (e.g. Newton's $F = ma$). Further details of GCMC and MD simulation are well documented in several texts (e.g. Nicholson and Parsonage (1982); Allen and Tildesley (1989); Frenkel and Smit (1996)).

The molecular models used in this work were generally built as assemblies of individual particles. Each particle was comprised of a Lennard-Jones (LJ) site to account for dispersive (van der Waals) interactions and/or a partial charge to account for electrostatic interactions. The potential energy, U_{ab}^{LJ}, between two LJ sites is calculated using the Lennard-Jones 12-6 potential

$$U_{ab}^{\mathrm{LJ}} = 4\varepsilon_{ab} \left[\left(\frac{\sigma_{ab}}{r} \right)^{12} - \left(\frac{\sigma_{ab}}{r} \right)^{6} \right] \tag{1.1}$$

and the standard Lorentz-Berthelot mixing rules

$$\sigma_{ab} = \frac{\sigma_a + \sigma_b}{2} \tag{1.2}$$

$$\varepsilon_{ab} = (\varepsilon_a \varepsilon_b)^{1/2} \tag{1.3}$$

where σ_a and ε_a are the site diameter and potential well depth for site a, respectively; and r is the distance between sites a and b. The electrostatic potential energy between two charged sites is

$$U_{ab}^{\mathrm{ch}} = \frac{q_a q_b}{4\pi\varepsilon_0 r} \tag{1.4}$$

where q_a is the charge at site a. With two exceptions, each model particle corresponded to a particular atom in the given molecule. The first exception was the use of united-atom representations, which for some adsorbent models lumped hydrogen atoms with the carbon atoms to which they are attached, thereby reducing computational costs by reducing the number of site-site interactions. Second, in the case of the three-site nitrogen and hydrogen models, there exist central, non-atomic, partial-charge sites to balance the partial charges at the atomic positions. More specific details about the molecular simulation methods and

models used in this work are contained in their respective sections.

Isoteric heats of adsorption, q_{st}, were calculated for some systems from single-component GCMC simulations using fluctuations in the adsorbed number of molecules, N, and total system energy, E, according to (Nicholson and Parsonage, 1982; Vuong and Monson, 1996; Do et al., 2007)

$$q_{st} = kT - \frac{\langle UN \rangle - \langle U \rangle \langle N \rangle}{\langle N^2 \rangle - \langle N \rangle^2}. \tag{1.5}$$

Experimental adsorption data for gas mixtures at varying temperatures, pressures, and compositions are expensive and time-consuming to generate. Approximate methods such as ideal adsorbed solution theory (IAST) (Myers and Prausnitz, 1965), which uses only single-component isotherms as input, have been used successfully to predict mixed-gas behavior for several microporous materials (Goj et al., 2002; Yang and Zhong, 2006). IAST is a classic technique to predict the equilibrium adsorption for mixture using data from pure-component adsorption isotherms on the same adsorbent. IAST assumes the adsorbate mixture behaves as an ideal solution and there is no or negligible change in the thermodynamic properties of the adsorbent. IAST has been used with various degrees of success in predicting gas mixture adsorption selectivity for several microporous materials, including zeolites, silicalites, and metal-organic frameworks (Goj et al., 2002; Akten et al., 2003; Yang and Zhong, 2006). Simulated, single-component CO_2 and H_2 isotherms were used in this work with IAST to predict adsorption of binary CO_2/H_2 mixtures. These IAST results were then compared with results from mixed-gas simulations to evaluate the accuracy of the IAST method for the $Cu(BF_4)_2(bpy)_2$ MOF.

Chapter 2

GCMC Simulation of Carbon Dioxide Adsorption in Heterogeneous Porous Carbons

Capture of carbon dioxide from fossil fuel power plants via adsorption and sequestration of carbon dioxide in unmineable coal seams are achievable near-term methods of reducing atmospheric emissions of this greenhouse gas. To investigate the influence of surface heterogeneity upon predicted adsorption behavior in activated carbons and coal, isotherms were generated via grand canonical Monte Carlo simulation for CO_2 adsorption in slit-shaped pores with underlying graphitic structure and several variations of chemical heterogeneity (oxygen and hydrogen content), pore width and surface functional group orientation. Adsorption generally increased with increasing surface oxygen content, although exceptions to this trend were observed on structurally heterogeneous surfaces with holes or furrows that yield strongly adsorbing preferred binding sites. Among the heterogeneous pore structures investigated, those with coal-like surfaces adsorbed carbon dioxide more strongly than planar, homogeneous graphitic slit pores of comparable width. Electrostatic adsorbate-adsorbent interactions significantly influenced adsorption onto model surfaces.

2.1   Simulation Details

Isotherms for CO_2 adsorption into laterally infinite slit-shaped pores were generated via grand canonical Monte Carlo (GCMC) simulation using rectangular periodic boundary conditions. All simulations were performed at a temperature of 273 K, slightly below the CO_2 critical temperature of 304 K. The three-site TraPPE CO_2 model, which was optimized to reproduce pure component bulk vapor-liquid equilibria, was used in this study (Potoff

and Siepmann, 2001). Table 2.1 lists the parameters used for this model. Each atomic site is characterized as a Lennard-Jones (LJ) sphere with a partial charge. Lennard-Jones and electrostatic fluid-fluid interactions were truncated at 2.0 nm.

Atom	Coordinate (nm)	σ (nm)	ε/k_B (K)	Charge, q (e)
C	0	0.280	27.0	0.70
O	± 0.116	0.305	79.0	-0.35

Table 2.1   Lennard-Jones and charge parameters for three-site CO_2 model (Potoff and Siepmann, 2001).

The absorbent surfaces were varied to investigate the influence of chemical and topological heterogeneity upon CO_2 adsorption. Isotherms for the 10-4-3 graphite surface (Steele, 1974) were generated for comparison. The potential energy between a Lennard-Jones site on an adsorbate molecule and a smooth, homogeneous 10-4-3 graphitic surface is

$$U_{sf} = 2\pi\varepsilon_{sf}\rho_s\sigma_{sf}^2\Delta\left[0.4\left(\frac{\sigma_{sf}}{z}\right)^{10} - \left(\frac{\sigma_{sf}}{z}\right)^4 - \frac{\sigma_{sf}^4}{3\Delta\left(z+0.61\Delta\right)^3}\right] \qquad (2.1)$$

where ε_{sf} and σ_{sf} are calculated using the Lorentz-Berthelot mixing rules, Δ is the distance between graphene layers, and ρ_s is the solid density. The potential parameters used for graphite were: $\sigma_C = 0.34$ nm, $\varepsilon_C/k_B = 28.0$ K, $\Delta = 0.335$ nm, $\rho_s = 114$ nm-3 (Steele, 1974).

One set of model surfaces used in this study was generated by (1) cleaving a graphite crystal parallel to the ($\bar{1}010$) or ($\bar{1}012$) planes (perpendicular or slanted relative to the basal plane of graphite, respectively) and (2) attaching H, OH, or COOH functional groups in varying concentrations onto the exposed graphite carbon atoms so as to maintain sp2 hybridization. In this manner, the effect of surface chemical heterogeneity (as manifested by the presence of oxygen-containing surface functional groups) was investigated for CO_2 adsorption in carbon micropores while still maintaining the periodicity and low dimensionality associated with the graphite slit pore geometry. All model surfaces were assumed to be rigid. The number of pendant OH or COOH groups and their angle of attachment to the surface were varied. Table 2.2 lists the surfaces examined in this study and provides, with the cleavage plane of the underlying carbon structure, the type and density of the appended functional group, and the attachment angle for the surface groups identified for each model surface. Where applicable, the surfaces on opposing walls of a slit pore were reversed relative to one other (i.e. not simply reflected across the center plane of the pore).

Figure 2.1 shows four of these model surfaces to a depth of ~ 0.5 nm below the cleavage plane. For the GCMC simulations, each model structure extended ~ 2.2 nm below the

Model surface name	Cleavage plane	Functional group	Attachment angle (°)	Attachment pattern
c0_H	$(\bar{1}010)$	H only	—	—
c2_H	$(\bar{1}012)$	H only	—	—
c0_OH_a0_6 × 8	$(\bar{1}010)$	OH	0	6 × 8
c0_OH_a90_6 × 8	$(\bar{1}010)$	OH	90	6 × 8
c0_COOH_a0_6 × 8	$(\bar{1}010)$	COOH	0	6 × 8
c0_COOH_a90_6 × 8	$(\bar{1}010)$	COOH	90	6 × 8
c2_COOH_a0_6 × 8	$(\bar{1}012)$	COOH	0	6 × 8
c0_COOH_a0_6 × 4	$(\bar{1}010)$	COOH	0	6 × 4
c0_COOH_a90_6 × 4	$(\bar{1}010)$	COOH	90	6 × 4
c2_COOH_a0_6 × 4	$(\bar{1}012)$	COOH	0	6 × 4

Table 2.2 Names and construction parameters for model surfaces constructed by cleaving a graphite crystal and appending H, OH, or COOH functional groups to the exposed edges of graphene layers.

cleavage plane. The simulation cells spanned $\sim$ 4.0 to 4.8 nm in the lateral directions and were sized to accommodate 12 graphene edge planes with 16 exposed carbon atoms per edge. This resulted in 4032 and 4992 aromatic carbon atoms per simulation cell for the $(\bar{1}010)$ and $(\bar{1}012)$ surfaces, respectively. The highest density arrangements of OH or COOH functional groups occupied alternating exposed carbon sites on alternating graphene layers, resulting in a maximum of 6 x 8 = 48 oxygen-bearing functional groups per simulation cell. Sites not occupied by OH or COOH groups were saturated with H atoms. Note that the resulting C:O ratio for these model surfaces is not in itself significant particularly because the thickness of the underlying graphitic structure was arbitrarily chosen.

The short-ranged nature of the dispersion and dipole-quadrupole adsorbate-adsorbent interactions in this study suggests that the carbon atoms more than $\sim$ 0.5 nm below the cleavage plane do not exert a major influence on CO_2 adsorption. The solid-fluid interaction energy includes both Lennard-Jones and electrostatic contributions. Every atom in the surface structure was represented as a Lennard-Jones site, and partial charges were assigned to each atom in the appended functional groups and to the carbon atom to which the groups are attached to the graphite surface. Table 2.3 lists the dispersion and charge parameters used to describe the atoms in these surfaces. Given the idealized nature of these surfaces, the force fields were not tuned to reproduce results from experimental adsorption measurements. The selected Lennard-Jones parameter values are comparable to values used elsewhere (Freindorf and Gao, 1996; Vishnyakov et al., 1998). The assigned partial charges were based upon results obtained from ab initio calculations for representative $\sim$ 100 atom polycyclic aromatic hydrocarbons performed using the Hartree-Fock method, 6-31g(d,p) basis set, and Mulliken charge analysis with the Gaussian 03 software package (Frisch et al., 2003).

Another model heterogeneous surface used in the molecular simulations is shown in Figure 2.2. This surface has a carbon content similar to that of a typical coal (Fitzgerald et al., 2003; Ozdemir et al., 2003), and was oriented parallel to the basal plane of the
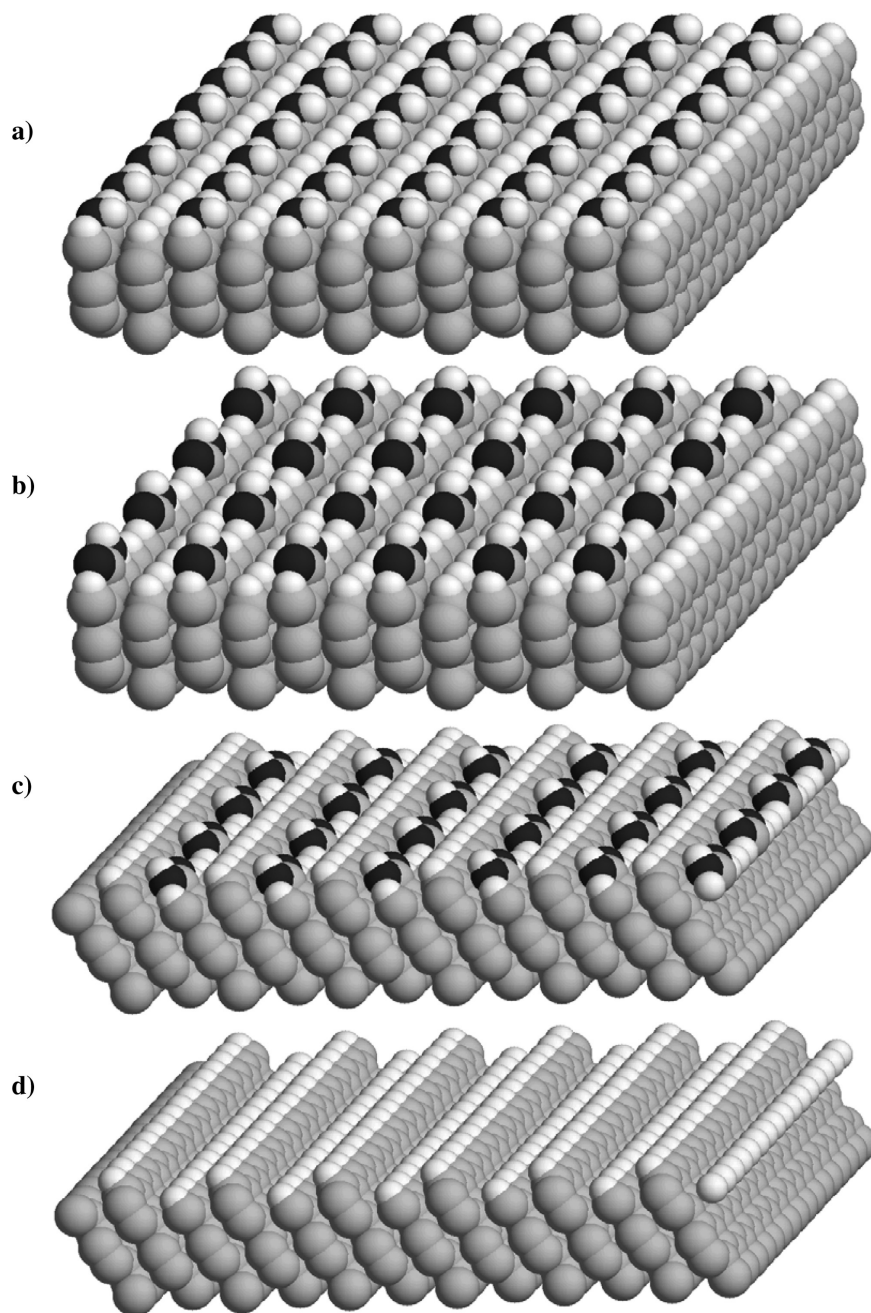
Figure 2.1 Examples of model surfaces summarized in Table 2: a) c0_OH_a90_6x8 b) c0_COOH_a0_6x4 c) c2_COOH_a0_6x4 d) c2_H. Surfaces are composed of carbon (light gray), oxygen (dark gray), and hydrogen (white) atoms.

Surface	Atom or site	σ (nm)	ε/k_B (K)	Charge, q (e)
graphite	C (aromatic)	0.340	28.0	—
cleaved graphite, H appended	C (aromatic)	0.340	28.0	−0.16
	H	0.240	12.0	0.16
cleaved graphite, OH appended	C (aromatic)	0.340	28.0	0.30
	O	0.310	79.0	−0.60
	H	0.130	30.0	0.30
cleaved graphite, COOH appended	C (aromatic)	0.340	28.0	−0.06
	C (COOH)	0.340	28.0	0.75
	O (=O)	0.310	79.0	−0.50
	O (—O—H)	0.310	79.0	−0.55
	H	0.130	30.0	0.36
coal-like surface, explicit H	C	0.340	28.0	varies
	O	0.310	79.0	varies
	H	0.130	30.0	varies
coal-like surface, implicit H	C (aromatic)	0.360	66.0	—
	CH (aromatic)	0.356	94.6	—
	CH_2	0.385	85.6	—
	C (other)	0.340	66.0	—
	O (all)	0.310	125.0	—

Table 2.3 Lennard-Jones and charge parameters used to represent atoms in model surfaces.

underlying graphite. To create a surface with both chemical and topological heterogeneity, selected carbon atoms from the top graphene layer were either removed entirely or replaced with oxygen- and hydrogen-containing functional groups, yielding a 212-atom surface structurally similar to that used by Vishnyakov *et al.* (Vishnyakov et al., 1998). Simulations for the resulting surface were performed using three models of varying complexity and computational expense. First, the most complex and computationally intensive model represented each carbon, oxygen, and hydrogen atom in the top layer of the surface with both a Lennard-Jones sphere and a point charge. To allow direct comparison with results from other model surfaces in this study, the LJ parameters chosen for this model were unchanged from those described above (see Table 2.3). Point charges for each surface atom (not listed) were obtained from ab initio calculations using the Hartree-Fock method, 6-31g basis set, and Mulliken charge analysis with the Gaussian 03 (Frisch et al., 2003) software package.

To study the importance of adsorbate-adsorbent electrostatic interactions, a second model used the same LJ parameters as the first but omitted all surface point charges. The third and least computationally expensive model omitted surface point charges and used a set of LJ parameters derived from Vishnyakov *et al.* (Vishnyakov et al., 1998) which only implicitly account for the presence of hydrogen atoms (see Table 2.3). For each of these three models, the adsorbate-adsorbent interactions for the subsurface layers in this structure were modeled using the 10-4-3 potential.

Simulations were performed for nominal pore widths H = 1.35, 1.8, and 2.4 nm, where for a graphitic slit pore, H is measured from the centers of the carbon atoms on the surface layers of the opposing pore walls. Pore widths of this size range are characteristic of the pore
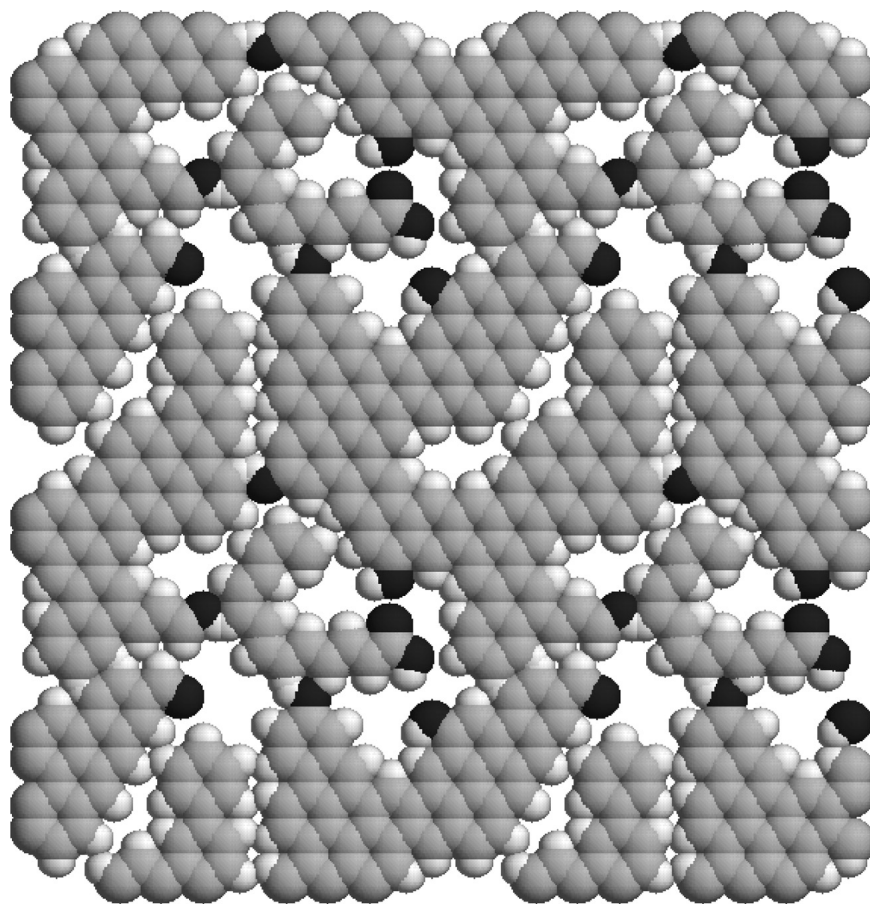
Figure 2.2 Top view of the coal-like model surface composed of carbon (light gray), oxygen (dark gray), and hydrogen (white) atoms.

size distributions obtained for typical coal samples (Tsotsis et al., 2004). The pore widths of the heterogeneous model surfaces considered in this study were adjusted slightly so that the total available pore volume matched that of a homogeneous graphitic slit pore of comparable surface area and similar nominal pore width. Available pore volume is defined here as the region of the pore volume where the Lennard-Jones portion of the adsorbate-adsorbent potential has a zero or negative value.

To reduce the computational burden required for the molecular simulations, separate three-dimensional solid-fluid potential maps were generated for the dispersion and electrostatic interactions between the adsorbate atoms and the adsorbent surface by summing over all of the explicitly represented surface atoms prior to GCMC simulation. These summations were truncated at $\sim$ 6 nm for Lennard-Jones interactions and at $\sim$ 60 nm for electrostatic interactions. The maps were discretized onto a 0.01 nm grid. The potential energy between the adsorbent and a particular CO_2 Lennard-Jones site or charge site was calculated via linear interpolation between grid points. Convergence of the simulation results using truncation and discretization was verified (results not shown). Excess adsorption versus P/P_0 was calculated from absolute adsorption versus fugacity simulation results using thermodynamic equation of state data for carbon dioxide from the NIST Chemistry WebBook (Lemmon et al., 2005).

2.2   Results

Figures 2.3, 2.4, 2.5, and 2.6 show the mean and minimum adsorbate-adsorbent Lennard-Jones potentials for an oxygen site on the CO_2 molecule as a function of the site distance above the carbon surface for various model surfaces. For the Steele 10-4-3 surface and the coal-like surface, the $z = 0$ plane passes through the centers of the carbon atoms in the top graphene layer. For the other surfaces, the $z = 0$ plane passes through the centers of the aromatic carbon atoms to which the OH or COOH functional groups were attached. The total CO_2-adsorbent potential is the sum of the potential interactions for the three constituent Lennard-Jones sites (two oxygen and one carbon), plus the electrostatic interactions, if applicable. The latter are a function of both distance and orientation relative to the surface.

Figure 2.7a presents excess adsorption isotherms for slit pores with Steele graphite surfaces and coal-like surfaces with explicit hydrogen atoms and point charges at three different pore widths. Figure 2.7b repeats the 1.35 nm slit pore results from Figure 2.7a and shows for comparison results from simulations using the uncharged explicit-H and implicit-H coal-like surface models. Figure 2.8 reports excess adsorption isotherms for 1.35
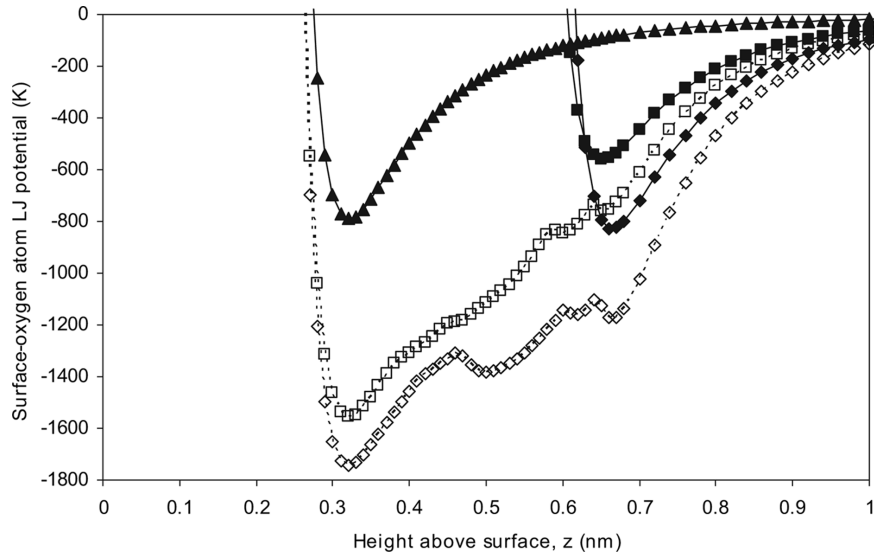
Figure 2.3 Mean (filled symbols) and minimum (open symbols) adsorbate-adsorbent Lennard-Jones potentials for a CO2 oxygen site versus distance above the surface for coal-like model surfaces with explicit hydrogen atoms (squares) and implicit hydrogen atoms (diamonds). The one-dimensional potential for the Steele surface (triangles) is shown for comparison.
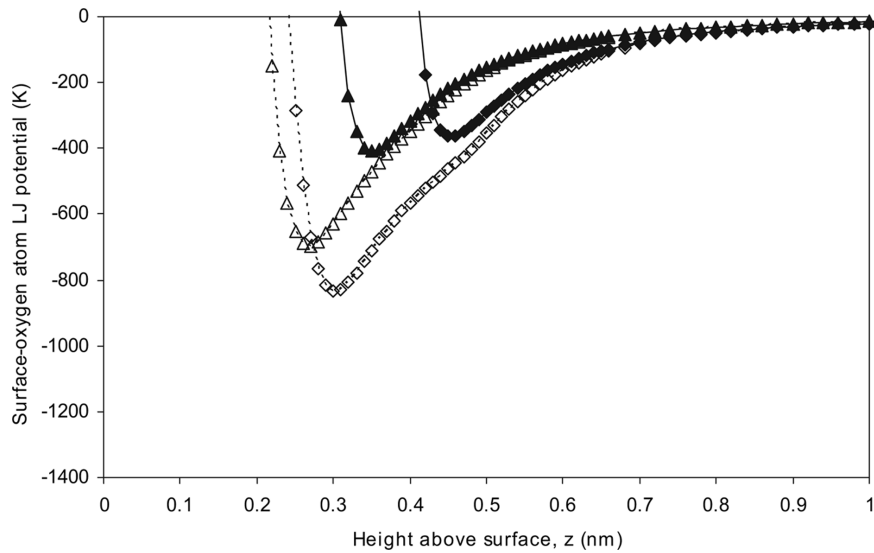
Figure 2.4 Mean (filled symbols) and minimum (open symbols) surface-fluid potential for a Lennard-Jones CO2 oxygen site versus distance above the surface for the c0_H (triangles) and c2_H (diamonds) model surfaces.
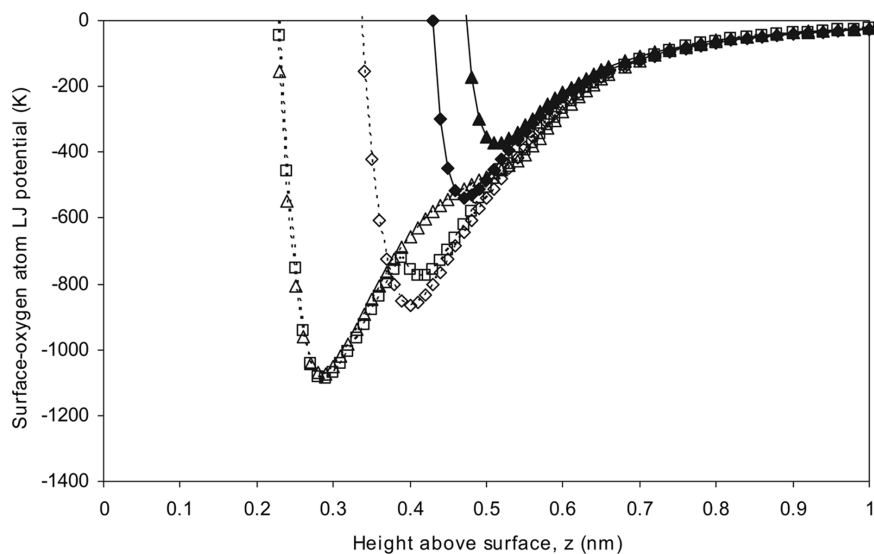
Figure 2.5 Mean (filled symbols) and minimum (open symbols) Lennard-Jones potential for an oxygen CO2 site versus distance above surface for the c0_COOH_a0_6x8 (triangles), c2_COOH_a0_6x8 (diamonds), and c0_COOH_a90_6x8 (squares) surfaces. The average potential for the c0_COOH_a90_6x8 surface coincides with that for the c0_COOH_a0_6x8 surface and is omitted for clarity.
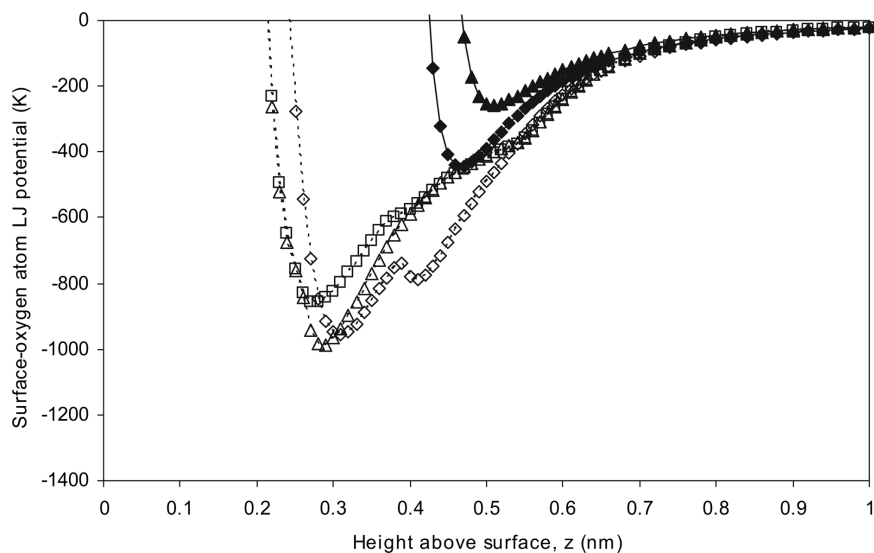
Figure 2.6 Same notation as in Figure 2.5, except for the 6 x 4 rather than the 6 x 8 surfaces.

nm slit pores with various truncated graphite model surfaces substituted with H, OH or COOH surface groups. Continuous filling rather than phase transitions were observed in the isotherms for the 1.35 nm slit pores of all surface compositions, and capillary condensation occurred only in the largest (2.4 nm) pore size considered. Adsorption/desorption hysteresis was not observed for any of the surfaces studied. Figure 2.9 shows snapshots from GCMC simulations at $P/P_0 = 0.001$, 0.1, and 0.44 for 2.4 nm slit pores with coal-like surfaces with explicit hydrogen atoms and surface charges. Figure 10 shows a snapshot at $P/P_0 = 0.1$ for one surface of a 2.4 nm slit pore with c0_COOH_a0_6x8 surfaces.

The deep trough at $z \sim 0.31$ nm in the minimum potential curves for the coal-like surfaces in Figure 2.3 is indicative of a hole or cavity in the first surface layer. The low energy at this site results from interactions with the underlying surface layer and surface atoms around the edge of the hole. The large difference between the minimum and mean potential curves for the coal-like surface is a consequence of the surface roughness. The broadness of the minimum potential curve for the coal-like surface, compared with the potential curve for the Steele surface, suggests that monolayer formation and wetting of the coal-like surface by CO_2 should occur over a wider range of pressures than for the Steele surface. This expectation is confirmed in the excess adsorption isotherms reported in Figure 2.7 for slit pores with Steele- and coal-like surfaces. Because the minimum potential for the coal-like surface is significantly lower than the Steele potential, it was expected that CO_2 adsorption would universally occur at lower pressures for the coal-like surface than for the Steele surface. This is not observed, however, in Figure 2.7b for the uncharged explicit-H surface model, for perhaps two reasons. First, it is possible that the low energy cavity sites on the coal-like surface are too few in number to compensate for the weaker mean potential interaction of CO_2 with the coal-like surface. Second, because CO_2 is a linear molecule, orientation and size exclusion play a significant role in its adsorption onto surface defect structures, and thus energetically favorable sites for the adsorption of a monatomic adsorbate (e.g. the oxygen site of CO_2) may not be accessible to the polyatomic CO_2 molecule. Adsorbate-adsorbate interactions, which increase as the surface coverage increases, also influence binding at particular surface sites.

For simulations of coal-like surfaces in which electrostatic interactions were included, electrostatic adsorbate-adsorbent interactions accounted for 60 to 70% of the total adsorbate-adsorbent potential energy at low surface coverage, which significantly increased adsorption of CO_2 relative to the uncharged case. In contrast, for simulations with the idealized heterogeneous model surfaces, the electrostatic adsorbate-adsorbent interactions accounted for only 20 to 30% of the total adsorbate-adsorbent potential energy, and CO_2 adsorbed less strongly onto these surfaces than onto the Steele surface. While the relatively large
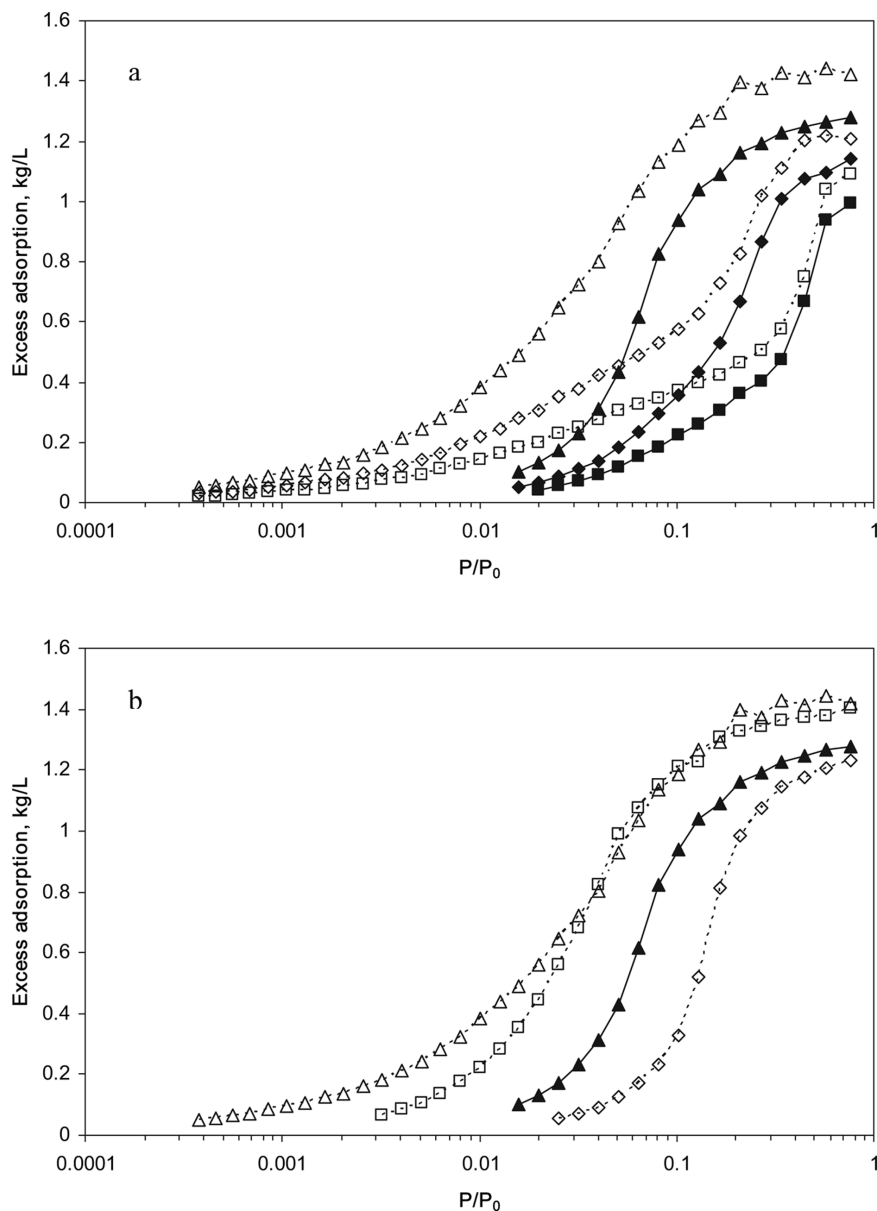
Figure 2.7 a) Excess CO2 adsorption isotherms at 273 K for 2.4 (squares), 1.8 (diamonds), and 1.35 (triangles) nm slit pores with Steele graphite surfaces (solid symbols) or coal-like surfaces with explicit hydrogen atoms and charges (open symbols). b) Excess CO2 adsorption isotherms at 273 K for 1.35 nm slit pores with Steele graphite surfaces (solid triangles), coal-like surfaces with explicit hydrogen atoms and charges (open triangles), coal-like surfaces with explicit hydrogen atoms but without charges (open diamonds), and coal-like surfaces with implicit hydrogen atoms (open squares).
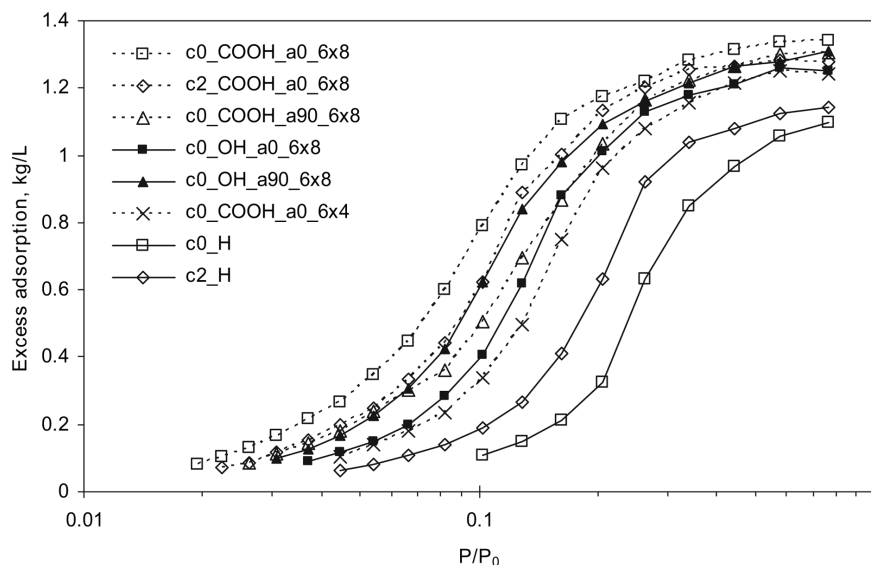
Figure 2.8 Excess CO2 adsorption isotherms for 1.35 nm slit pores for various model surfaces at 273 K.

LJ interaction potentials for the uncharged implicit-H coal-like surface resulted in high-pressure adsorption behavior similar to that for the charged explicit-H surface, low-pressure adsorption is still greatly reduced (Figure 2.7b).

A comparison of the Lennard-Jones potentials of Figure 2.4 indicates that the c2_H model surface is topologically rougher and possesses sites that bind more strongly than the c0_H surface. As shown in Figure 2.8, for the c2_H surface, the isotherm is broader and more CO_2 adsorption occurs at lower relative pressures than for the c0_H surface.

Figure 2.5 compares the mean and minimum potentials for the three model surfaces with COOH functional groups arranged in a 6 x 8 pattern. The c0_COOH_a90_6x8 and c0_COOH_a0_6x8 surfaces differ only in the attachment angle of the COOH functional group, and it is seen that the mean potentials for these surfaces overlap. In contrast, the minimum potential for the c0_COOH_a90_6x8 surface has a secondary minimum at $z =$ 0.41 nm that is not present in the minimum potential for the c0_COOH_a0_6x8 surface. Relative to the other surfaces, the c2_COOH_a0_6x8 surface is topologically smoother and energetically more uniform, with a higher minimum potential but a lower mean potential. As can be seen in Figure 2.8, CO_2 adsorption in the c0_COOH_a0_6x8 slit pore is significantly enhanced relative to the other two surfaces with the same arrangement of COOH sites. Although initial adsorption of CO_2 into the c2_COOH_a0_6x8 and c0_COOH_a90_6x8 slit pores occurs at the same relative pressure, pore filling is completed at a slightly lower pressure for the c2_COOH_a0_6x8 surface, consistent with the topological differences between the two surfaces.
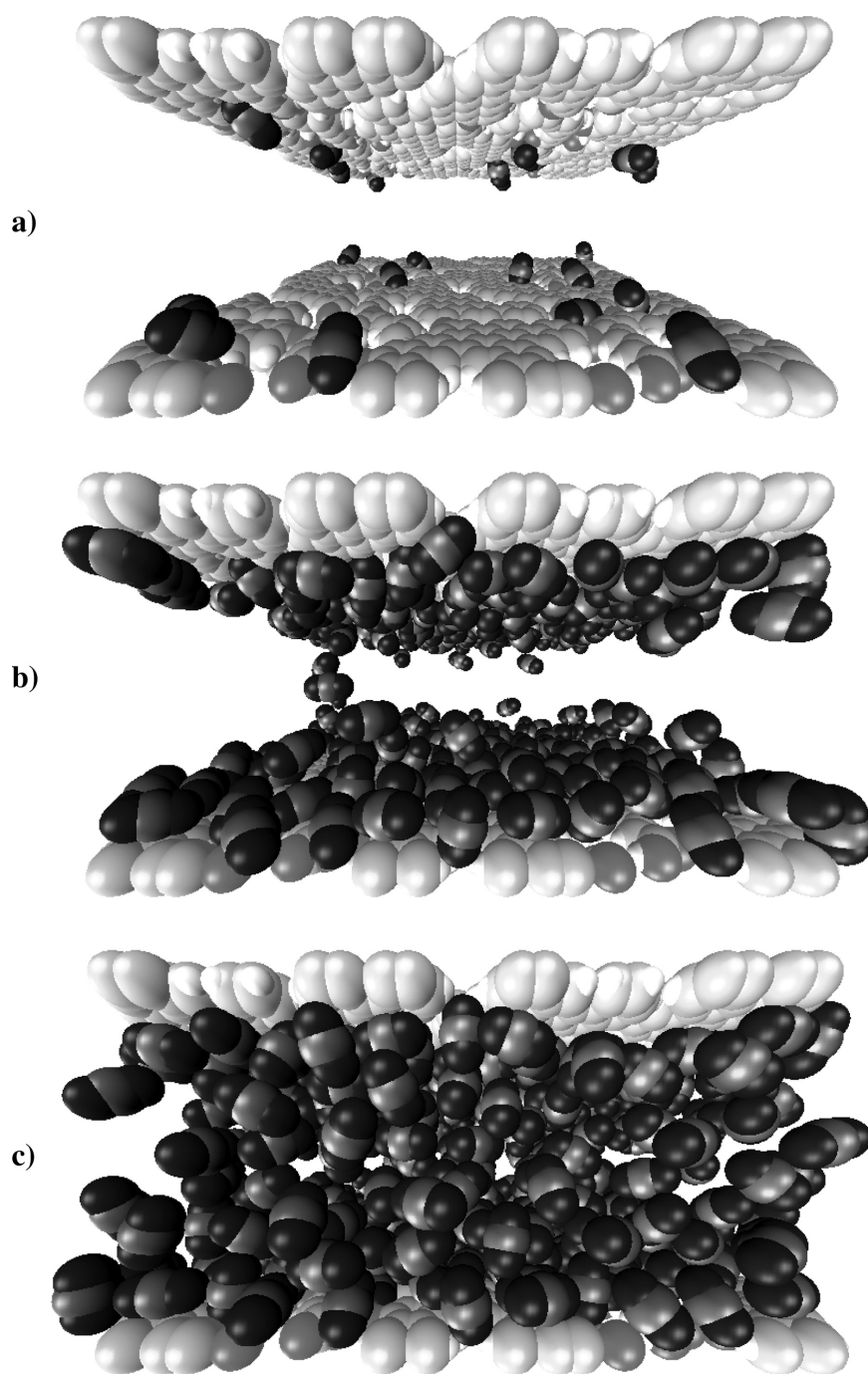
Figure 2.9 Snapshots of CO2 adsorption at 273 K and P/P_0 = 0.001, 0.1, and 0.44 (a, b, and c, respectively) in 2.4 nm slit pores having coal-like surfaces with explicit hydrogen atoms and charges.
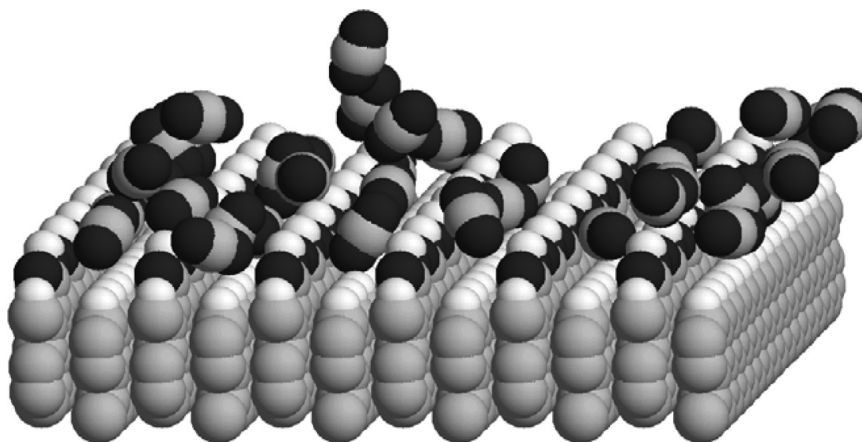
Figure 2.10 Snapshot of CO2 adsorption on a c0_COOH_a0_6x8 surface in a 2.4 nm slit pore at 273 K and $P/P_0 = 0.1$.

The surfaces represented in Figure 2.6 have half the COOH functional group site density of the surfaces represented in Figure 2.5. In general, this results in a weaker Lennard-Jones interaction potential (as indicated by Figure 2.6) and a decrease in CO_2 adsorption (as seen in the c0_COOH_a0_6x4 curve of Figure 2.8). The general ordering of the mean potentials for the various surfaces remains unchanged, with the exception of the c2_COOH_a0 surface, which acquires a secondary minimum in its potential for a 6 x 4 ordering of the functional groups that is absent in the 6 x 8 ordering; and the c0_COOH_a90 surface, which has a secondary minimum in the 6 x 8 ordering but not in the 6 x 4 ordering. These differences indicate that the orientation of surface functional groups can significantly influence the energy landscape, and hence the resulting GCMC isotherms. Figure 2.10 shows how CO_2 preferentially adsorbs in the energetically favorable valleys between the rows of COOH surface groups in the c0_COOH_a0_6x8 slit pore. This CO_2 alignment was observed for many of the model surfaces investigated in this study.

The mean and minimum adsorbate-adsorbent potentials for surfaces with OH functional groups (not pictured) featured single minima approximately 100 K higher in energy (ε/k_B) than those for corresponding surfaces with COOH sites. As seen in Figure 2.8, with the exception of the c0_COOH_a90_6x8 surface, surfaces with COOH functional groups generally adsorb CO_2 more strongly than surfaces with an equivalent number of OH groups. It was noted that the rank ordering of surfaces with OH functionality, but the same underlying cleavage plane structure, in terms of their adsorption strength was somewhat different than the rank ordering for the same surfaces with COOH functional groups. While there is significant variation among the isotherms for the various 6 x 8 surfaces, the corresponding set of isotherms (not shown) for CO_2 adsorption on the 6 x 4 surfaces were much more similar. The cleavage plane of the adsorbent surface was observed to have a significant

effect on CO_2 adsorption, particularly so in the case of unsubstituted (H-only) surfaces for which substantial differences in the isotherms of the c0_H and c2_H surfaces were noted.

Chapter 3

GCMC Simulation of Carbon Dioxide Separation from Nitrogen Using a Copper-Organic Framework Adsorbent

Adsorption of carbon dioxide and nitrogen on the metal organic framework (MOF) $Cu(BF_4)_2(bpy)_2$ (bpy=bipyridine) was simulated at temperatures, pressures, and compositions representative of flue gas streams from fossil fuel power plants. This MOF was chosen because it displays a novel CO_2 adsorption behavior in which the crystal structure reversibly transitions from an empty, zero porosity state to a fully-saturated, expanded state at what has been termed the gate pressure. Estimates of CO_2 capacity above the gate pressure from grand canonical Monte Carlo (GCMC) simulations using an experimentally-determined rigid model structure showed good agreement with experiment at 273K. CO_2 adsorption capacity ($\sim$140 mg CO_2/g) and estimated heats of adsorption ($\sim$35 kJ/mol) are comparable to common physi-adsorbents at similar process conditions. Mixed-gas simulations predict a CO_2/N_2 selectivity of $\sim$700 at 300K, which is significantly higher than common physi-adsorbents at this temperature.

3.1 Simulation Details

Isotherms for pure and mixed-gas adsorption into $Cu(BF_4)_2(bpy)_2$ latent porous crystals (LPC) were generated via grand canonical Monte Carlo (GCMC) simulation using triclinic periodic boundary conditions. Post-equilibration simulation runs were composed of 2-8 million MC moves. The open-source MCCCS Towhee software package (http://towhee.sourceforge.net) (Martin and Siepmann, 1999) was used for all GCMC simulations. The rigid model structure used for the GCMC simulations was the CO_2-expanded

form of the LPC (structure 2a in Kondo et al. (2006)). This structure was found using crystallographic methods during CO_2 adsorption above the gate pressure at 273 K (Kondo et al., 2006). Figure 1.4 shows a top view of two, stacked 4x4 layers of the expanded LPC. Each non-orthogonal simulation cell contained ten 4x4 layers, corresponding to a total of 160 Cu atoms.

Simulated pure CO_2 adsorption isotherms for comparison with experiment were generated at 273K, which is slightly below the CO_2 critical temperature of 304 K. Simulated isotherms were generated for several binary mixtures of CO_2 and N_2 at 300, 350, and 400 K to investigate adsorption under realistic process temperatures and pressures. Additional pure N_2 and CH_4 isotherms were generated for comparison with experiment in order to evaluate the applicability of the rigid LPC model structure, which was found via crystallography during CO_2 adsorption, to adsorbents other than CO_2. The three-site TraPPE CO_2 and N_2 models, which were optimized to reproduce pure component bulk vapor-liquid equilibria (Potoff and Siepmann, 2001), were used. Each atomic site in the TraPPE models is composed of a Lennard-Jones (LJ) sphere and a partial point charge. The DREIDING force field (Mayo et al., 1990) was used for the LPC and CH_4 models. The DREIDING forcefield does not include an entry for Cu2+. DREIDING does, however, include Fe2+ and Zn2+, which bracket Cu on the periodic table, and uses the same Lennard-Jones (aka dispersion or van der Waals) parameters for both Fe2+ and Zn2+. Therefore, the parameters for Fe2+ were used for Cu2+ in the MOF model. Each copper ion was assigned a charge of +2, and the immediately adjacent fluorine atoms were assigned charges of -1. LJ interactions were truncated at 1.4 nm, and long-range electrostatic interactions were calculated using Ewald summation. Excess adsorption versus pressure was calculated from absolute adsorption versus fugacity (or chemical potential) simulation results using thermodynamic equation of state data for carbon dioxide and nitrogen from the NIST Chemistry WebBook (Lemmon et al., 2005).

3.2   Pure-gas Adsorption Results

Figure 3.1 shows experimental isotherms and simulation results for CO_2 adsorption into the rigid LPC model at 273K. At pressures above the gate pressure of ∼0.35 bar (and below 1 bar) simulation predicts a saturated capacity of approximately 160g of CO_2 per mg of LPC. This corresponds to two adsorbed CO_2 molecules per pore or two CO_2 molecules per copper atom. Experimental isotherms at 273K show lower saturation amounts of ∼140 g/mg (Onishi et al., 2002), suggesting that the experimental LPC sample likely possessed

defects that deviate from the idealized crystal structure.
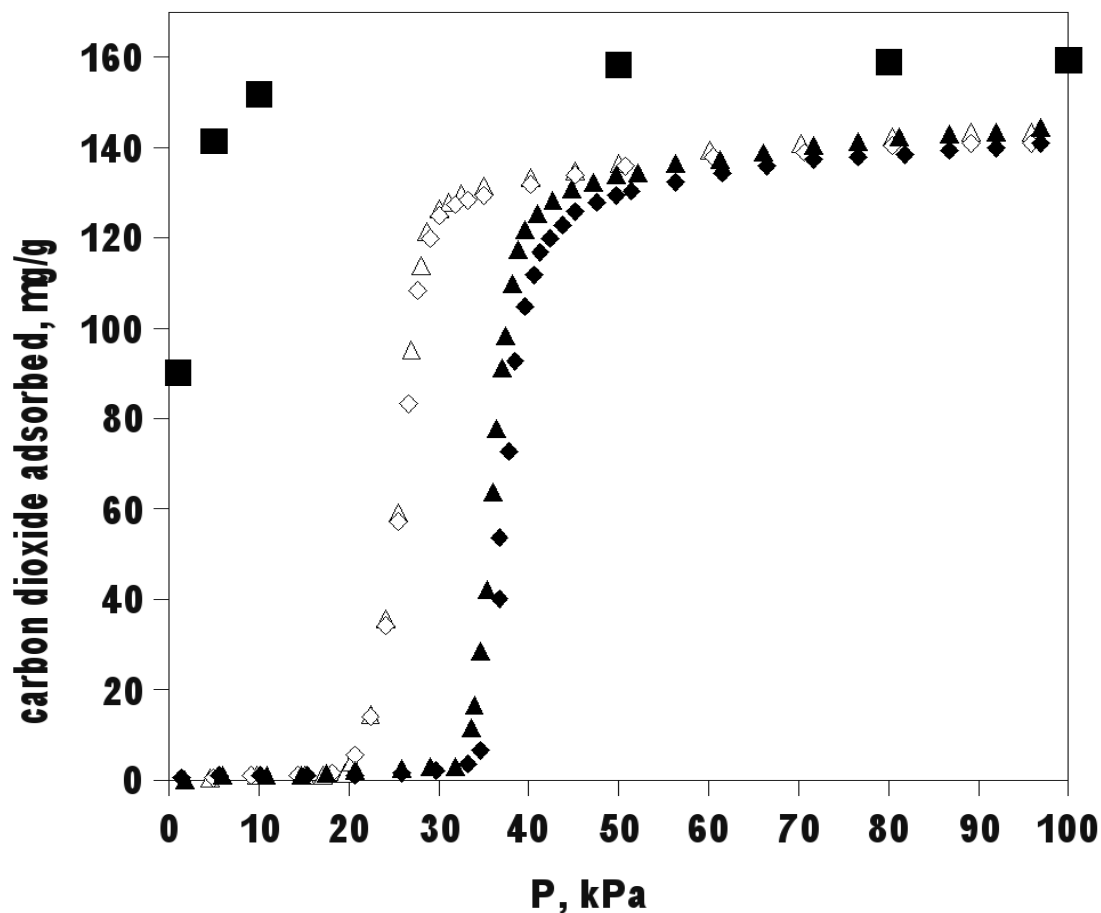
Figure 3.1 Adsorption (filled symbols) and desorption (open symbols) of CO_2 on $Cu(BF_4)_2(bpy)_2$ at 273K. Two experimental adsorption-desorption cycles are shown ($\diamond$ and $\triangle$, respectively) (Onishi et al., 2002). GCMC simulation results for CO_2 adsorption on the rigid expanded MOF model are shown for comparison ($\square$).

Figure 3.2 shows isosteric heats of adsorption, q_{st}, for CO_2 adsorption onto $Cu(BF_4)_2(bpy)_2$. Results were calculated using Equation 1.5 from single-component GCMC simulations at 300, 350, and 400K and for bulk gas pressures from 1 to 100Pa. Isosteric heat for CO_2 increases with pore loading due to increased adsorbate-adsorbate interactions. Simulations at much higher pressures show this trend continuing as loading is increased further until a plateau of $\sim$50kJ/mol is reached (results not shown). Because this heat of adsorption is calculated from simulations using a rigid $Cu(BF_4)_2(bpy)_2$ model, it is regarded as an upper-bound. Expansion of the flexible MOF structure requires an energy input, reducing the amount of energy released during adsorption and shifting simulation isotherms to lower

pressures relative to experiment. This shift can be seen in Figure 3.1. The relationship

$$\Delta q_{st} \approx RT \ln(P_{gate}/P_{fill}), \tag{3.1}$$

where P_{gate} is the experimental gate pressure and P_{fill} is the simulated filling pressure, can provide an estimate of the energy required to expand the MOF structure. The observed pressures at which the transition from zero to saturated adsorption occurs in the experimental and simulated isotherms at 273K (Figure 3.1) suggest that the actual heat of adsorption should be ~5-10kJ/mol lower than that calculated from simulation on the rigid model. Heats of adsorption for CO_2 adsorption into the actual, flexible $Cu(BF_4)_2(bpy)_2$ structure are therefore predicted to be ~33–37kJ/mol.
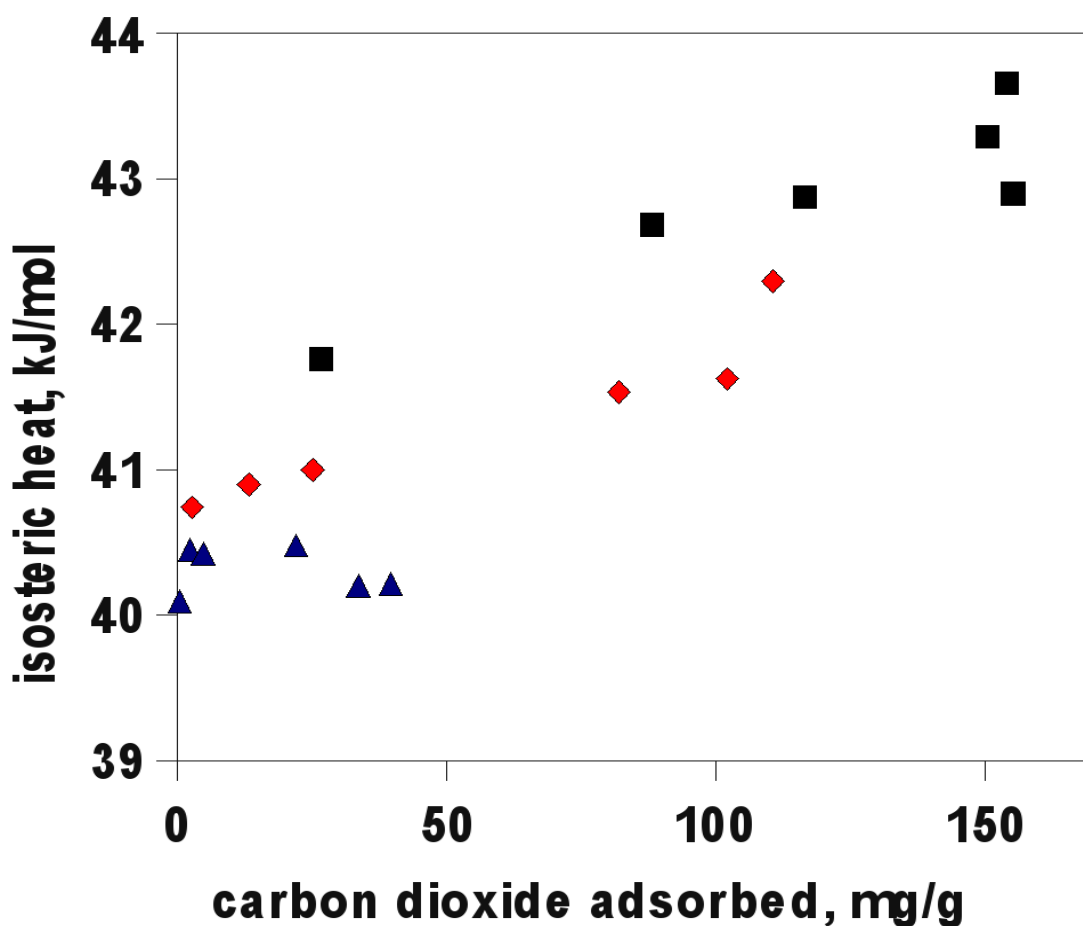
Figure 3.2 Upper-limit estimation of isosteric heats of adsorption, q_{st}, calculated using Equation 1.5 from GCMC simulations of CO_2 adsorption on the rigid model $Cu(BF_4)_2(bpy)_2$ structure at 300K-◇, 350K-□ and 400K-△ and pressures of 1 to 100kPa. Actual heats of CO_2 adsorption for the flexible LPC are expected to be 5-10kJ/mol lower.

Using the heat of adsorption and an integrated form of the Clausius-Clapeyron equation,

$$\Delta \ln \left(\frac{P_1}{P_2} \right) = \frac{q_{st}}{R} \left(\frac{1}{T_1} - \frac{1}{T_2} \right) \tag{3.2}$$

where R is the ideal gas constant, it is possible to estimate the gate pressure P_2 at temperature T_2 from an experimental gate pressure of P_1 at T_1. Assuming $q_{st} \approx 35$kJ/mol, this results in an estimate of a gate pressure of $\sim$140kPa at 300K.

To further evaluate the validity of the simulation model, Table 3.1 compares experimental and simulation results for the number of CO_2, N_2, or CH_4 molecules adsorbed per Cu atom from single-component bulk gases at pressures above their gate pressure. Simulated and experimental CO_2 adsorption capacity at 273K are in close agreement. This is expected, as the rigid model structure used in the simulations was determined experimentally during CO_2 adsorption above the gate pressure at 273K. In contrast simulation results for N_2 and CH_4 often deviate significantly from experimental values, indicating that $Cu(BF_4)_2(bpy)_2$ expands to assume different structures for different adsorbates. While this calls into question the use of this model structure for general simulation of mixed CO_2/N_2 adsorption, it is not expected to cause problems at the temperatures and pressures considered in this study. As seen in Figure 3.4, the amount of N_2 adsorbed is generally negligible relative to the amount of CO_2 adsorbed, and so structural rearrangement is expected to be dictated primarily by CO_2 adsorption, with N_2 adsorption only being possible once the structure has expanded to accomodate CO_2. At much higher pressures or very low temperatures, where N_2 adsorption can be non-negligible, a flexible simulation model would likely be necessary.

adsorbate	T (K)	P_{gate} (atm)	P (atm)	N_{ads}/Cu (exp't)	N_{ads}/Cu (sim.)
CO_2	273	0.30	1	1.8 2.1*	2.0
N_2	77	$\sim$0.07**	1	6.5	2.0
N_2	196	47	69	3.9	1.8
CH_4	258	17	59	3.5	-
CH_4	303	41	59	2.2	1.7

Table 3.1 Comparison of experimental (exp't) and simulated (sim.) adsorption capacity for adsorption of CO_2, N_2, and CH_4 into $Cu(BF_4)_2(bpy)_2$. Expressed as number of adsorbate molecules (N_{ads}) per copper atom (Cu). *varies with adsorbent pre-treatment temperature (Li and Kaneko, 2001) **gated transition from empty to saturated adsorption of N_2 at 77K is less abrupt than that observed for CO_2 at 273K (Onishi et al., 2002)

3.3   Mixed-gas Adsorption Results

Figures 3.3, 3.4, and 3.5 show results from from mixed-gas simulations at 300, 350, and 400K and bulk gas pressures of 100kPa and 200kPa as a function of the bulk phase CO_2 mole fraction. The amount of CO_2 adsorbed (Figure 3.3) decreases significantly with increasing temperature and increases slightly with increased pressure. The mole fraction of CO_2 in the adsorbed phase (Figure 3.4) remains close to unity but decreases slightly with temperature at very low bulk gas CO_2 mole fractions. The mole fraction of CO_2 in the adsorbed phase is essentially independent of pressure.

Selectivity of CO_2 over N_2 is defined as

$$S_{CO_2/N_2} = \frac{x_{CO_2}/y_{CO_2}}{x_{N_2}/y_{N_2}} \tag{3.3}$$

where x_a and y_a are the mole fractions of component a in the adsorbed and bulk gas phases, respectively. As seen in Figure 3.5, selectivity is predicted to decrease significantly with temperature and increase slightly with pressure. Within the uncertainty of the results, selectivity is essentially independent of bulk phase composition.

Figures 3.6 and 3.7 show snapshots of CO_2 and N_2 adsorption into $Cu(BF_4)_2(bpy)_2$ from a binary mixture at 273K and 100kPa. The top view (Figure 3.6) shows the regular arrangement of up to two adsorbate molecules per pore. The side view (Figure 3.7) shows that the adsorbate molecules are primarily located near the plane of the copper atoms. If there are two adsorbate molecules in a given pore, one is typically slightly above the plane of the copper atoms, the other slightly below. This arrangement results from the regular arrangement of the BF_4 groups from adjacent layers, which also occupy space in each pore.

Table 3.2 summarizes the predicted CO_2 adsorption capacity, selectivity relative to N_2, and isosteric heat of adsorption for $Cu(BF_4)_2(bpy)_2$ at 300K and 100kPa. Results for typical, high-performance commercial adsorbents under similar conditions are included for comparison. As can be seen from the table, $Cu(BF_4)_2(bpy)_2$ is predicted to display comparable adsorption capacity and heat of adsorption under these conditions, but the predicted CO_2/N_2 selectivity is much greater.
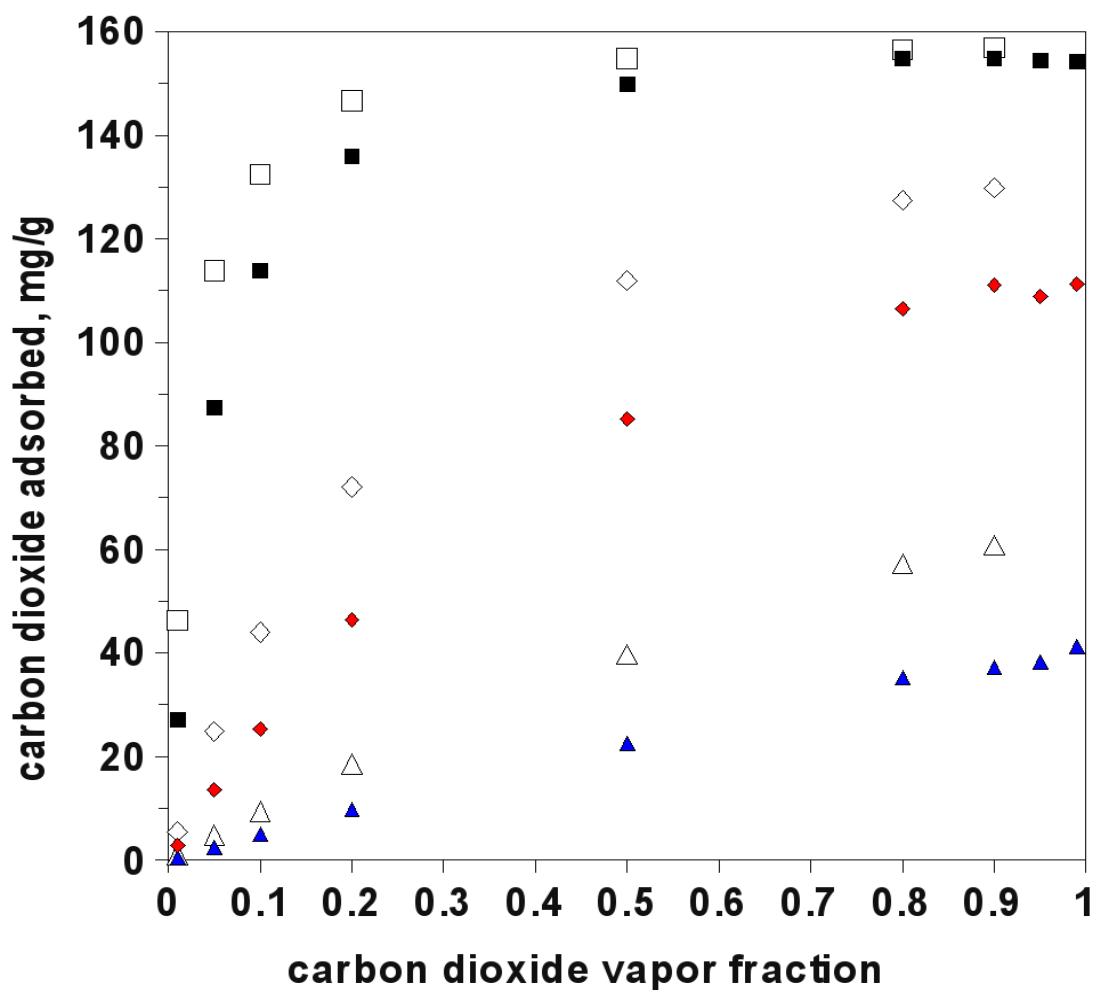
Figure 3.3 CO_2 adsorbed from binary mixtures of CO_2 and N_2 at 300-□, 350K-◊ and 400K-△ for bulk gas pressures of 100kPa (filled symbols) and 200kPa (open symbols). Standard deviation values are comparable to the size of the symbols.

adsorbent	capacity mg CO_2/g	CO_2/N_2 selectivity	q_st kJ/mol
Zeolite 13X	150*	50**	~36***
activated carbon	100*	20**	~30***
Cu(BF$_4$)$_2$(bpy)$_2$	130	600	33–37

Table 3.2 CO_2/N_2 adsorption characteristics for various porous materials at 300K and 100kPa. The predicted q_{st} values shown for Cu(BF$_4$)$_2$(bpy)$_2$ have been adjusted to account for the energy change associated with the expansion/collapse the flexible MOF structure during adsorption/desorption. *(Millward and Yaghi, 2005) **(Siriwardane et al.) ***(Chue et al., 1995)
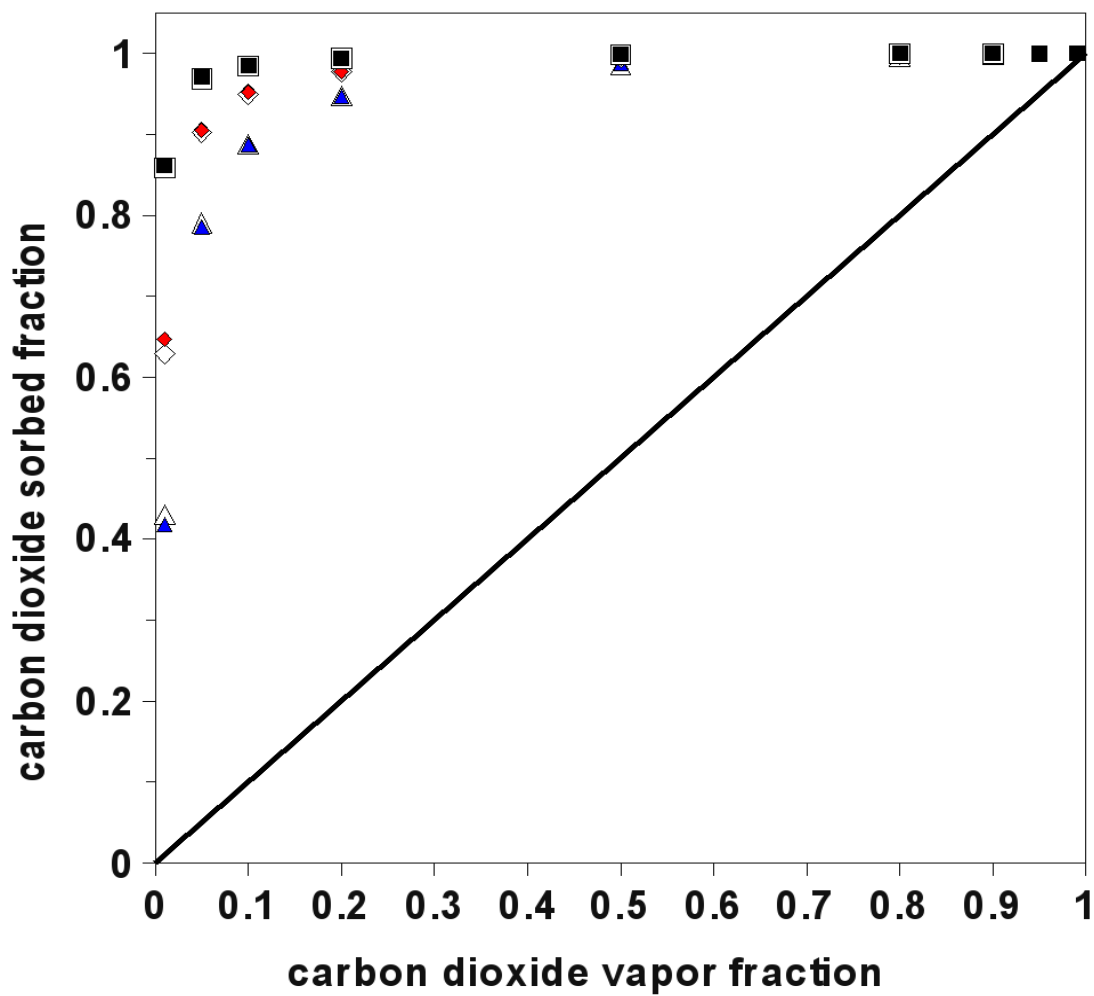
Figure 3.4 Adsorbate CO_2 mole fraction versus bulk gas CO_2 mole fraction for CO_2 adsorption from binary mixtures of CO_2 and N_2 at300-□, 350K-◇ and 400K-△ for bulk gas pressures of 100kPa (filled symbols) and 200kPa (open symbols). Standard deviaton values are comparable to the size of the symbols.
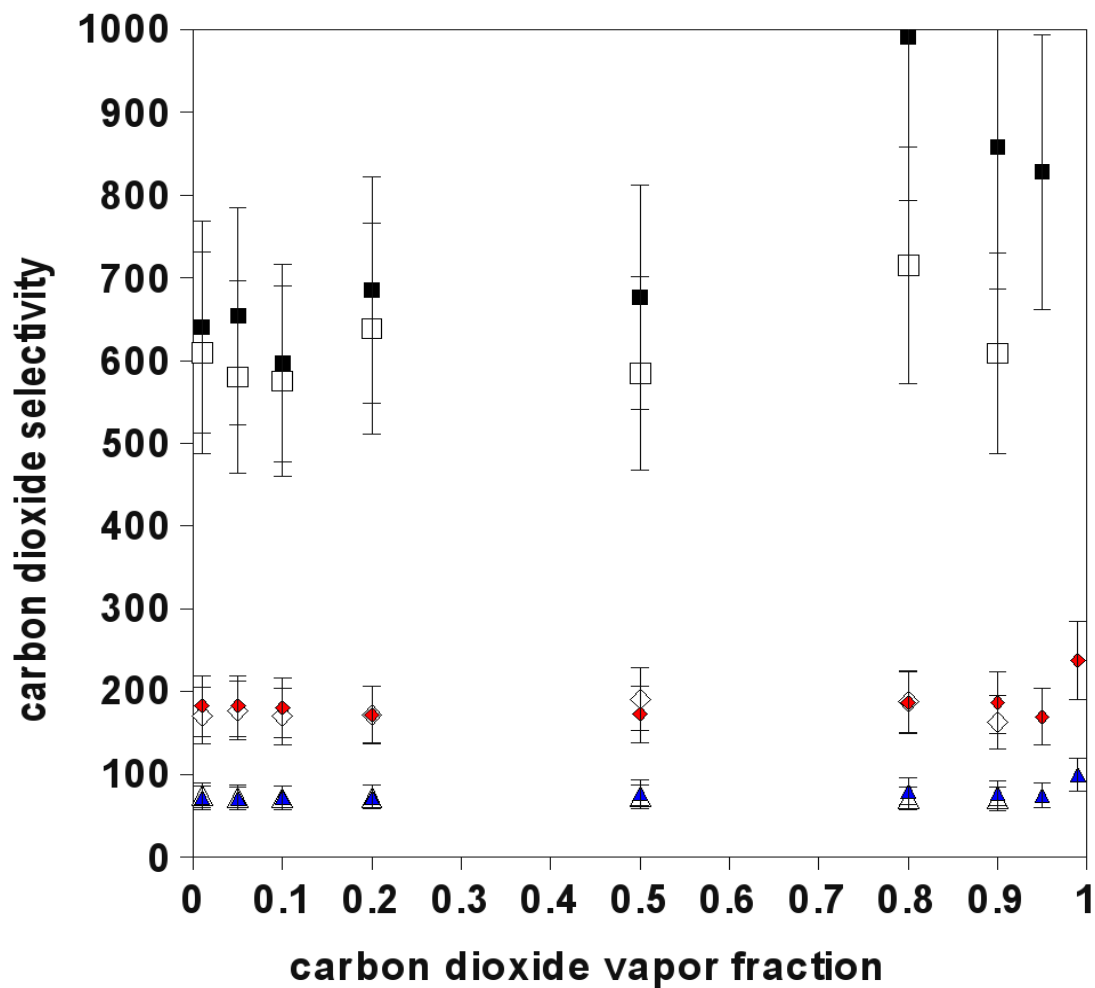
Figure 3.5 CO_2 adsorption selectivity from binary mixtures of CO_2 and N_2 versus bulk gas CO_2 mole fraction for CO_2 adsorption from binary mixtures of CO_2 and N_2 at 300-□, 350K-◇ and 400K-△ for bulk gas pressures of 100kPa (filled symbols) and 200kPa (open symbols). Error bars denote one standard deviation.
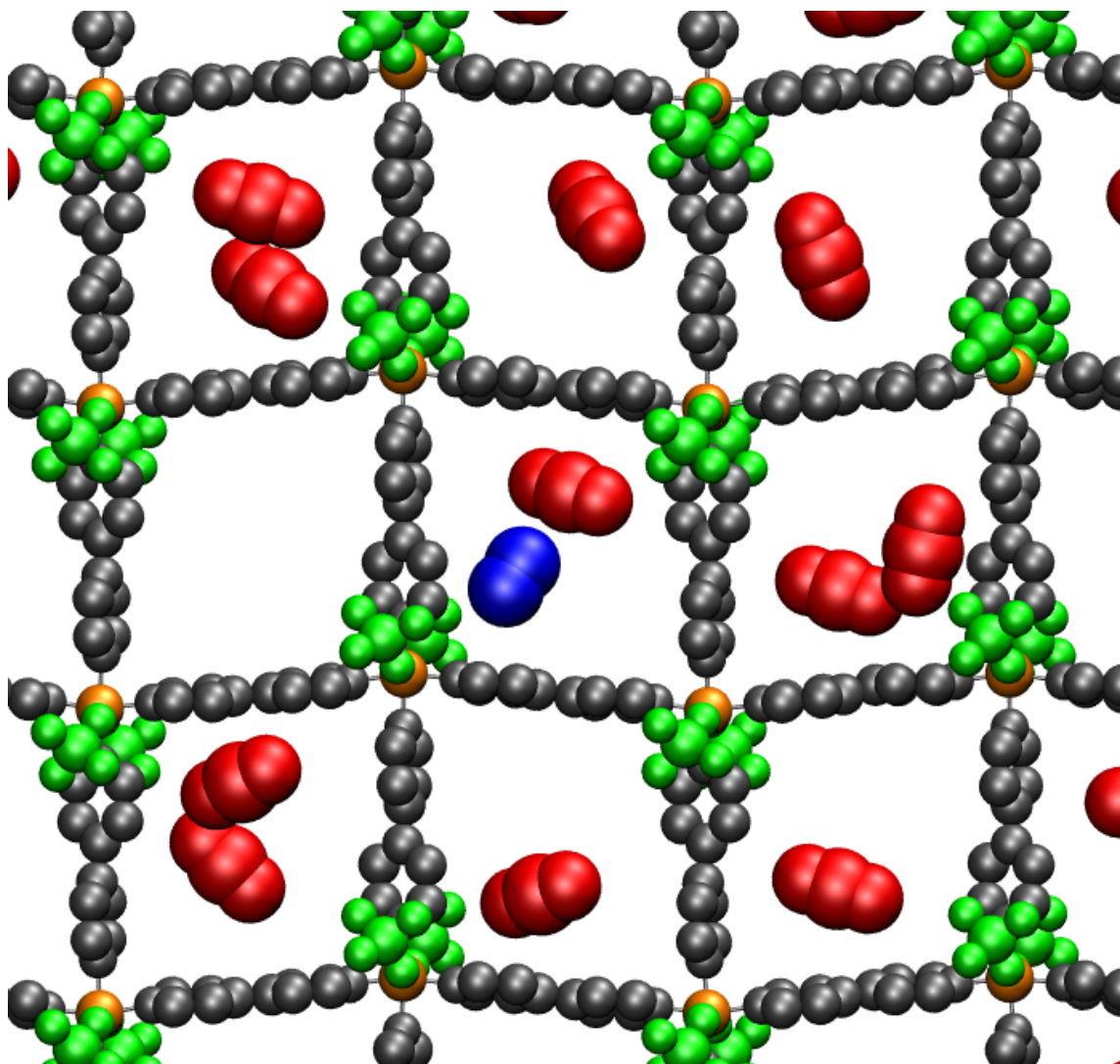
Figure 3.6 Snapshot of CO_2 and N_2 adsorption into one layer of $Cu(BF_4)_2(bpy)_2$ from a mixed gas (20 mol% CO_2) at 300K and 100kPa. One 4x4 section of one MOF layer is shown.
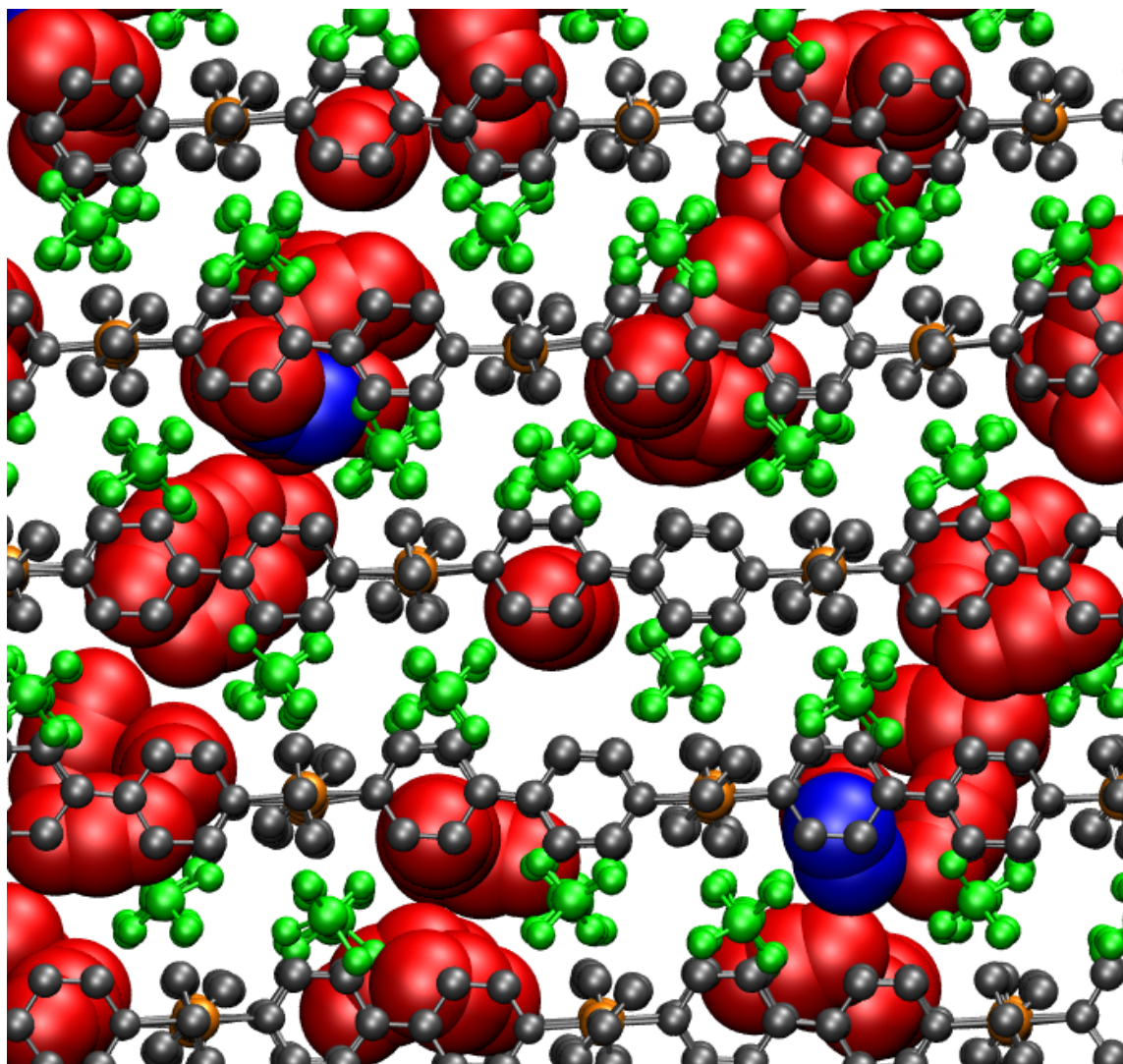
Figure 3.7   Snapshot of CO_2 and N_2 adsorption into $Cu(BF_4)_2(bpy)_2$ from a mixed gas (20 mol% CO_2) at 300K and 100kPa. Five stacked layers of the MOF are shown.

Chapter 4

GCMC Simulation of Carbon Dioxide Separation from Hydrogen Using a Copper-Organic Framework Adsorbent

Pure- and mixed-gas adsorption of CO_2 and H_2 on a novel, metal-organic framework (MOF), $Cu(BF_4)_2(bpy)_2$ (bpy=bipyridine), was simulated at temperatures, pressures, and compositions corresponding to realistic syngas processing conditions at integrated coal gasification combined cycle (IGCC) electric power plants. This MOF was chosen because it displays a novel CO_2 adsorption behavior in which the crystal structure reversibly transitions from an empty, zero-porosity state to a fully-saturated, expanded state at what has been termed the gate pressure. Grand canonical Monte Carlo (GCMC) simulation methods were used with a rigid model of the MOF in its CO_2-expanded form. Simulation results showed good agreement with experimental measurements of CO_2 capacity at 273K. Predicted CO_2 selectivity relative to H_2 for this MOF is higher than selectivities typically observed with other microporous materials. Selectivity generally decreased with increasing gas pressure at 298K and 373K. Predicted isosteric heats of adsorption are comparable to those of other common physi-adsorbing materials. Ideal adsorbed solution theory (IAST) estimates based on simulated single-component adsorption isotherms generally diverged from mixed-gas simulation results at 298K and 373K and high pressures.

4.1   Simulation Details

Isotherms for pure and mixed-gas adsorption into $Cu(BF_4)_2(bpy)_2$ latent porous crystals (LPC) were generated via grand canonical Monte Carlo (GCMC) simulation using triclinic periodic boundary conditions. Post-equilibration simulation runs were com-

posed of 2-8 million MC moves. The open-source MCCCS Towhee software package (http://towhee.sourceforge.net) (Martin and Siepmann, 1999) was used for all GCMC simulations. The rigid model structure used for the GCMC simulations was the CO_2-expanded form of the LPC (structure 2a in Kondo et al. (2006)), which was found using crystallographic methods during CO_2 adsorption above the gate pressure at 273 K (Kondo et al., 2006). Figure 1.4 shows a view of two 4x4 layers of the expanded LPC. Each non-orthogonal simulation cell contained ten 4x4 layers, corresponding to a total of 160 Cu atoms.

Simulated pure CO_2 adsorption isotherms for comparison with experiment were generated at 273K, which is slightly below the CO_2 critical temperature of 304 K. Simulated isotherms were generated for pure and mixed CO_2 and H_2 at 298, 373, and 473 K to investigate adsorption under realistic process temperatures and pressures. CO_2 was modeled using the three-site TraPPE CO_2 model, which has been optimized to reproduce pure component bulk vapor-liquid equilibria (Potoff and Siepmann, 2001). H_2 was modeled using a three-site hydrogen model (Alavi et al., 2005), for which the LJ potential has been optimized to reproduce the potential minimum of the SilveraGoldman pair potential for gas phase hydrogen (Silvera and Goldman, 1978). Each atomic site in the TraPPE CO_2 model and the Alavi model for H_2 is composed of a Lennard-Jones (LJ) sphere and a partial point charge. The DREIDING force field (Mayo et al., 1990) was used to model the LPC. The DREIDING forcefield does not include an entry for Cu2+. DREIDING does, however, include Fe2+ and Zn2+, which bracket Cu on the periodic table, and uses the same Lennard-Jones (aka dispersion or van der Waals) parameters for both Fe2+ and Zn2+. Therefore, the parameters for Fe2+ were used for Cu2+ in the MOF model. Each copper ion was assigned a charge of +2, and the immediately adjacent fluorine atoms were assigned charges of -1. LJ interactions were truncated at 1.4 nm, and long-range electrostatic interactions were calculated using Ewald summation. Excess adsorption versus pressure was calculated from absolute adsorption versus fugacity (or chemical potential) simulation results using thermodynamic equation of state data for carbon dioxide and hydrogen from the NIST Chemistry WebBook (Lemmon et al., 2005).

4.2   Pure-gas Adsorption Results

Simulation results for CO_2 adsorption in the expanded LPC model above the gate pressure of ∼0.35 bar (and below 1 bar) at 273K predict a saturated capacity of approximately 160g of CO_2 per mg of LPC. This corresponds to exactly two adsorbed CO_2 molecules per pore or two CO_2 molecules per copper atom. Experimental isotherms at 273K show saturation

amounts of ~140 g/mg (Onishi et al., 2002), suggesting that the experimental LPC sample may not be perfectly crystalline. Simulated single-component isotherms for CO_2 and H_2 on $Cu(BF_4)_2(bpy)_2$ are presented in Figure 4.1. As expected, the isotherms indicate that CO_2 interacts much more strongly with the MOF structure than H_2. The simulated CO_2 adsorption isotherms display saturation behavior at the pressures studied, while the adsorption isotherms for H_2 remain linear. The isotherms for 298 and 373K reach saturation (~3.6 mol/kg or 158 mg/g) at ~0.5 and ~4 MPa, respectively, while the 473K isotherm does not reach full saturation at the pressures studied. Because saturation in the rigid, model structure is expected to be a prerequisite for saturation in the flexible, expanding, real-world LPC, gate pressures for this MOF at temperatures above ~400K are expected to be much greater than pressures associated with typical IGCC operation.

The lines in Figure 4.1 show Langmuir model isotherms fitted to the CO_2 and H_2 simulation results. Fitting to continuous functions was done to permit the application of ideal adsorbed solution theory (IAST), which predicts multicomponent adsorption equilibrium using single-component isotherms. The Langmuir model describes the number of molecules adsorbed, N, as a function of pressure, P, according to

$$N(P) = \frac{N_{max}BP}{1+BP} \tag{4.1}$$

where N_{max} and B are the saturated adsorption amount and the Langmuir equilibrium constant, respectively, for the given adsorbate. Note that the Henry's constant, H, for the system is given by the product $N_{max}B$ and describes adsorption behavior in the linear, low-pressure, low-coverage region of the isotherm. The Langmuir model satisfactorily described both the CO_2 and H_2 isotherms within the standard deviation range of the simulated data. The fitted Langmuir parameters for H_2 and CO_2 adsorption isotherms are summarized in Table 4.1.

Temperature (K)	Adsorbate	H (mol/kg MPa)	B (1/MPa)
298	CO_2	833.33	221.33
	H_2	0.1796	0.0335
373	CO_2	30.211	7.9517
	H_2	0.0821	0.0144
473	CO_2	1.8440	0.4652
	H_2	0.0414	0.0095

Table 4.1 Fitted Langmuir parameters for single-component isotherms

Examination of values of H in Table 4.1 shows that H decreases with increasing temperature, which corresponds to a decrease in the amount adsorbed as temperature increases.
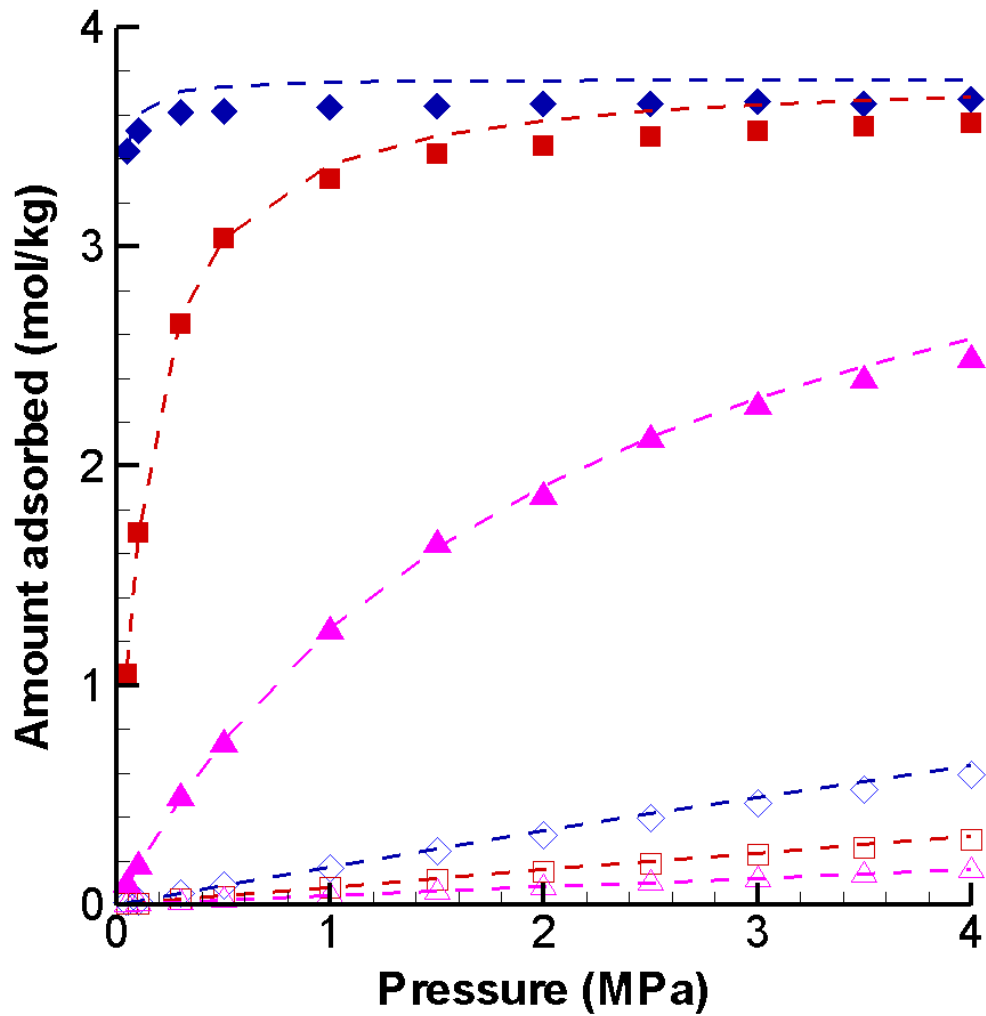
Figure 4.1 Single-component adsorption isotherms for CO_2 (filled symbols) and H_2 (open symbols) at 298K-◇, 373K-□ and 473K-△. Lines are Langmuir isotherm fits to the simulation data. Standard deviation values are comparable to the size of the symbols.

Additionally, H decreases more rapidly for CO_2 than for H_2. Because adsorption selectivity for CO_2 over H_2 can be approximated by H_{CO_2}/H_{H_2}, the H values in Table 4.1 suggest that CO_2/H_2 selectivity will decrease as temperature increases. The Henry's constants for CO_2 adsorption on this MOF are relatively high compared to other microporous adsorbents, indicating strong CO_2 interaction with the MOF structure, and suggesting that this LPC should display comparably high CO_2/H_2 selectivity relative to other adsorbents.
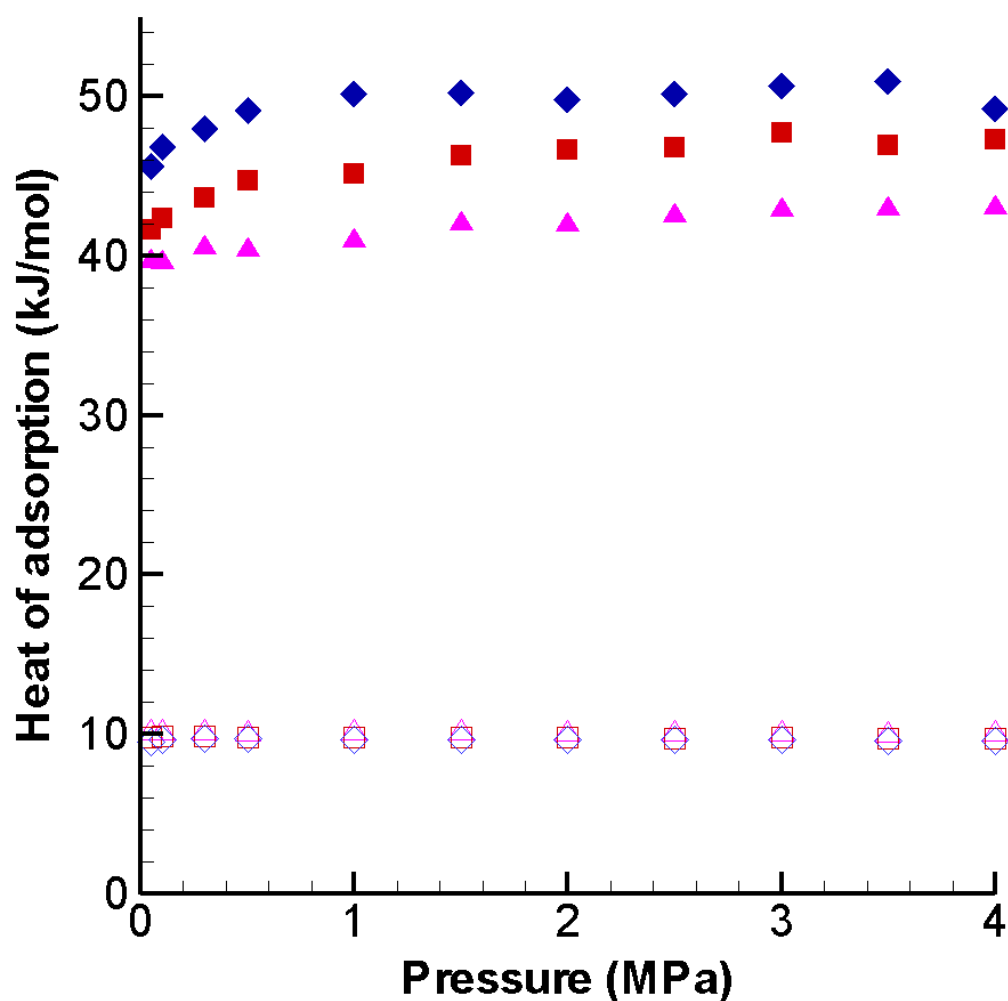
Figure 4.2   Upper-limit estimates of heats of adsorption, q_{st}, for CO_2 (filled symbols) and H_2 (open symbols) at 298K-◇, 373K-□ and 473K-△. Actual heats of CO_2 adsorption for the flexible LPC are expected to be 5-10kJ/mol lower.

Isosteric heats of adsorption, q_{st}, for CO_2 and H_2 at 298K, 373K and 473K were calculated from single-component GCMC simulations using Equation 1.5. Results are shown

in Figure 4.2. q_{st} for CO_2 increases slightly with pore loading and reaches a plateau as the pores are saturated with CO_2 molecules. This increase in q_{st} for CO_2 is attributed to adsorbate-adsorbate interactions. In contrast, q_{st} for H_2 is essentially constant over the range of pressures studied. This behavior has also been observed in other microporous materials like Zeolite Na-4A and Silicalite (Akten et al., 2003; Gallo et al., 2006) and is attributed to the small contribution of H_2-H_2 interactions when the extent of adsorption is far from saturation.

Because the heat of adsorption is calculated from simulations using a rigid $Cu(BF_4)_2(bpy)_2$ model, the results shown in Figure 4.2 are regarded as an upper-bound. Expansion of the flexible MOF structure during adsorption requires an energy input, reducing the amount of energy released during adsorption and shifting simulation isotherms to lower pressures relative to experiment. This shift can be seen in Figure 3.1. The relationship

$$\Delta q_{st} \approx RT \ln(P_{gate}/P_{fill}),$$ \hfill (4.2)

where P_{gate} is the experimental gate pressure and P_{fill} is the simulated filling pressure, can provide an estimate of the energy required to expand the MOF structure. The observed pressures at which the transition from zero to saturated adsorption occurs in the experimental and simulated isotherms at 273K (Figure 3.1) suggest that the actual heat of adsorption should be ~5-10kJ/mol lower than that calculated from simulation on the rigid model, resulting in predicted high-pressure heats of adsorption of 35–45kJ/mol.

4.3 Mixed-gas Adsorption Results

Figure 4.3 shows a snapshot of CO_2 and H_2 adsorption into $Cu(BF_4)_2(bpy)_2$ from an equimolar mixture at 298K and 1MPa. Each approximately rectangular pore contains at most two CO_2 molecules, and molecules in filled pores tend to align parallel to the co-planar pair of bipyridine rings (i.e. horizontally in the figure) in an arrangement that likely enhances adsorbate-adsorbent interaction.

CO_2 and H_2 isotherms for adsorption from equimolar mixtures are presented in Figure 4.4. The mixed-gas CO_2 isotherms are similar to those from pure CO_2 simulations with the adsorbed amount shifted to account for the reduced CO_2 partial pressure. In contrast H_2 adsorption from the equimolar mixed-gas is now essentially zero at all pressures, whereas H_2 adsorption from pure gas was proportional to pressure. The elimination of H_2 adsorption is attributed to the blocking of adsorption sites by CO_2, which interacts much more strongly with the adsorbent. Figure 4.5, which compares the pure-gas and equimolar mixed-gas
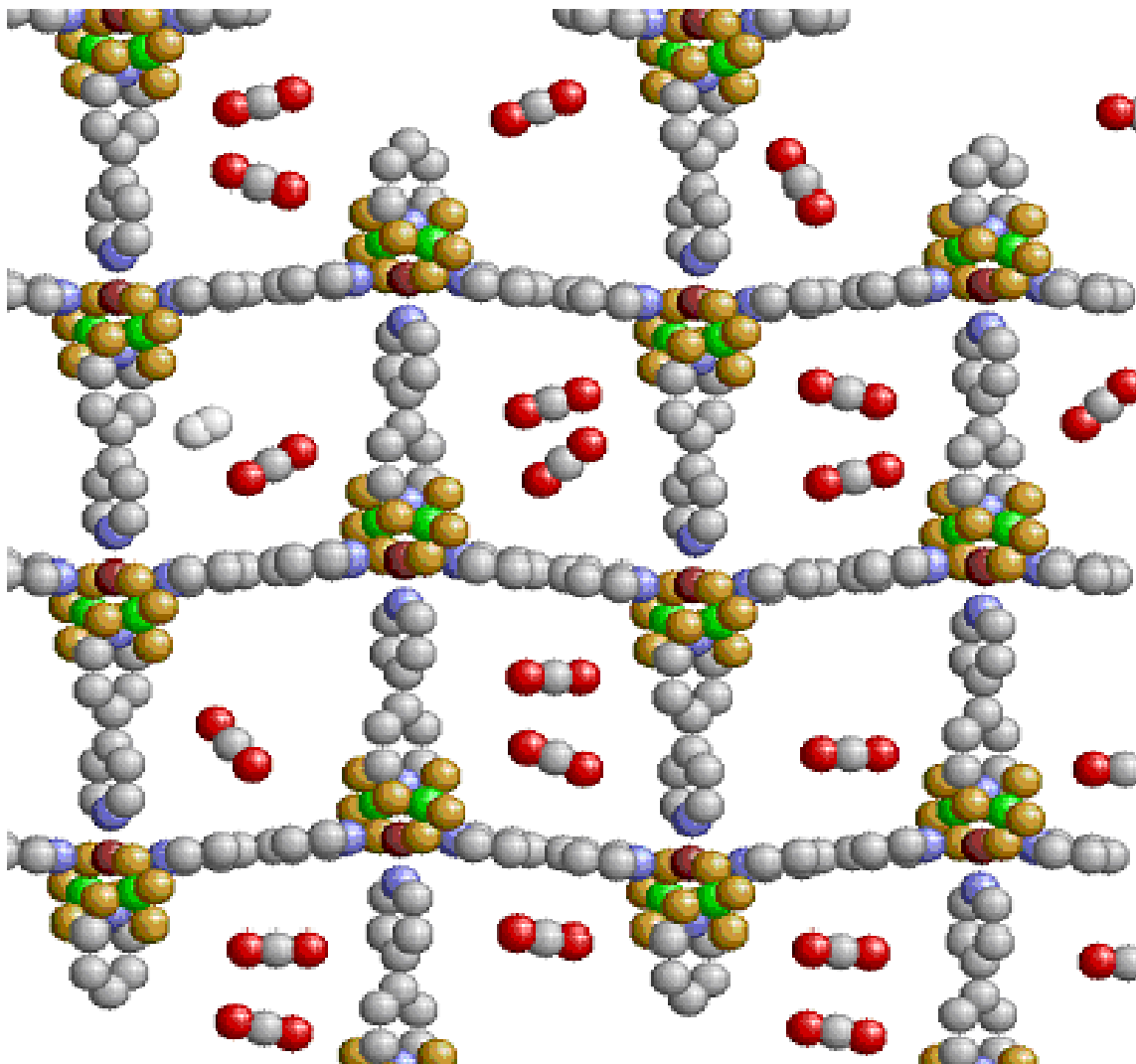
Figure 4.3 Snapshot of CO_2 and H_2 adsorption into $Cu(BF_4)_2(bpy)_2$ from an equimolar mixture at 298K and 1MPa.
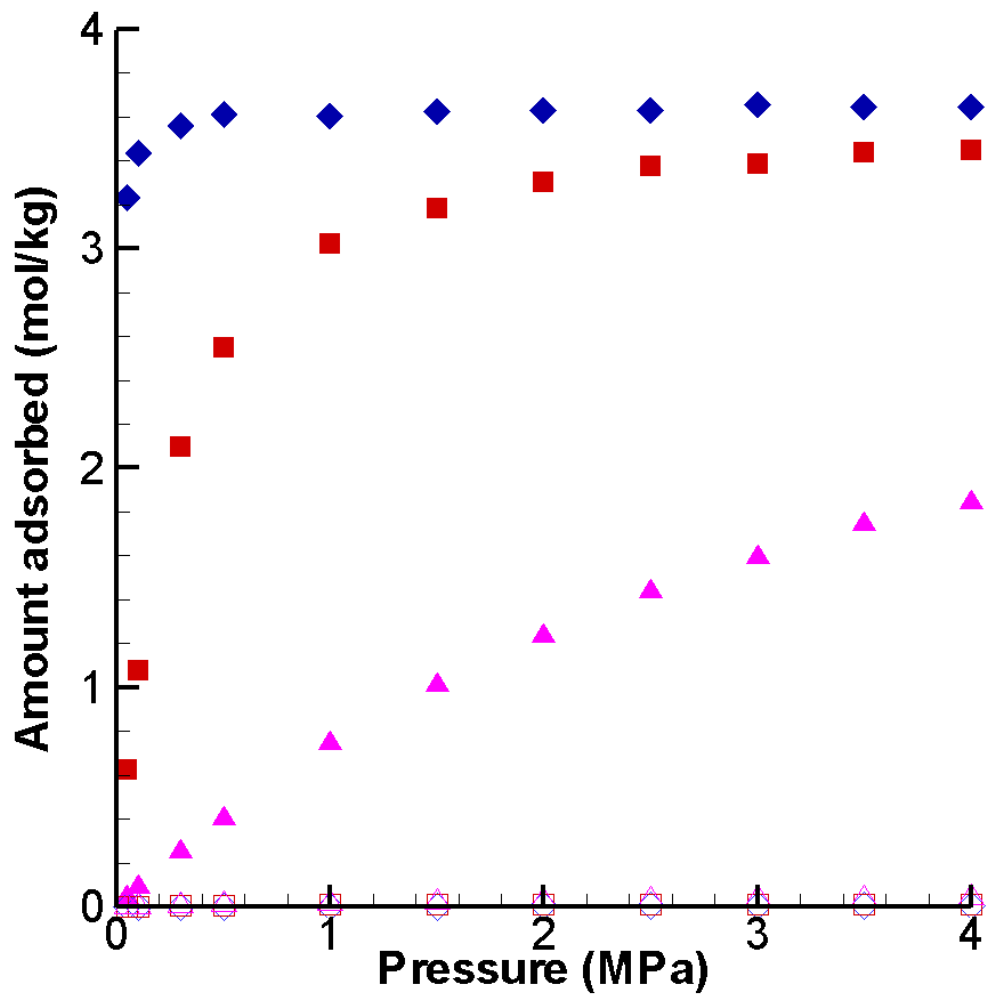
Figure 4.4 Adsorption of CO_2 (filled symbols) and H_2 (open symbols) from equimolar binary mixtures at 298K-◇, 373K-□ and 473K-△.
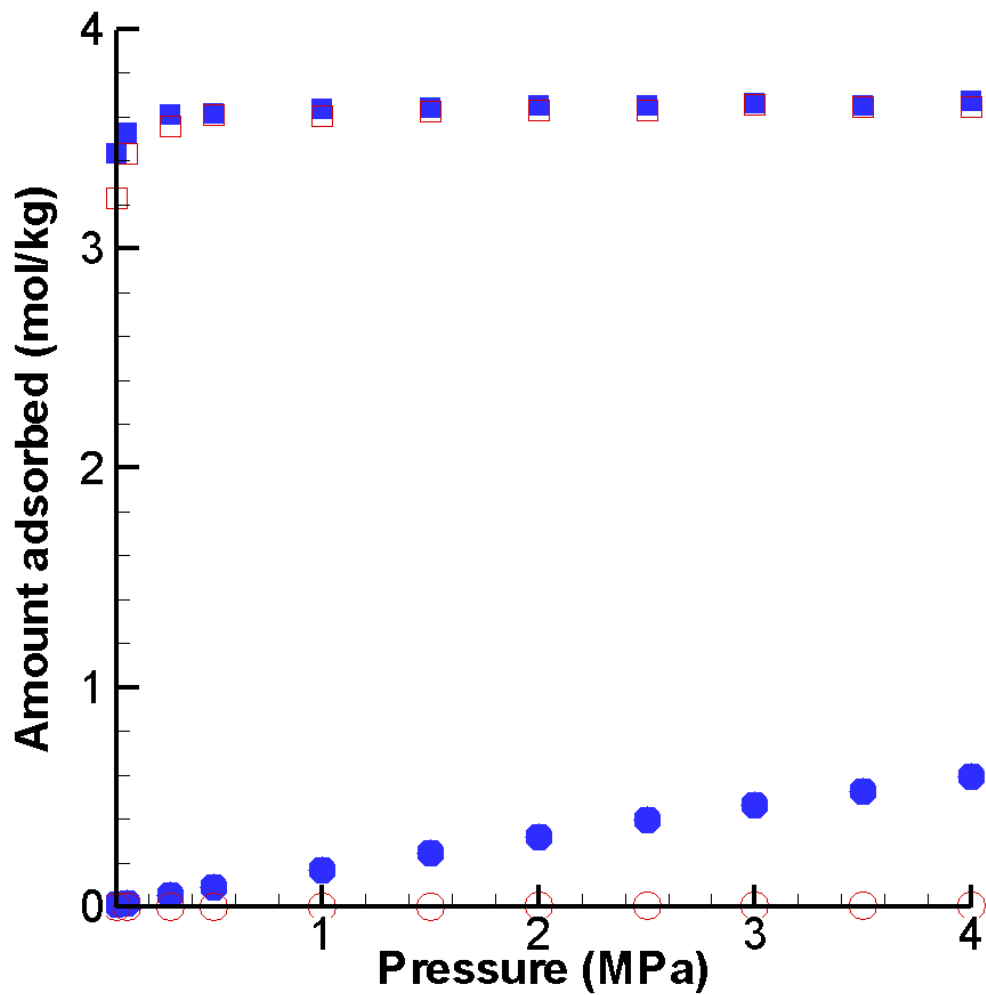
Figure 4.5 Adsorption of CO_2 (□) and H_2 (○) at 298K from pure-gases (filled symbols) and an equimolar binary mixture (open symbols).

adsorption isotherms for CO_2 and H_2 at 298K, clearly shows this effect and suggests that CO_2 selectivity calculated from mixed-gas simulations will be much higher than what might be predicted from pure-gas results alone.

Selectivity of CO_2 over H_2 is defined as

$$S_{CO_2/H_2} = \frac{x_{CO_2}/y_{CO_2}}{x_{H_2}/y_{H_2}} \tag{4.3}$$

where x_a and y_a are the mole fractions of component a in the adsorbed and bulk gas phases, respectively. Figure 4.6 plots the simulated adsorption selectivity of the MOF for the CO_2/H_2 binary mixture at three different temperatures over a pressure range typical of IGCC syngas. The selectivity is shown on logarithmic scale to capture the very different magnitudes of CO_2/H_2 selectivity at different temperatures. Also shown in Figure 4.6 are the corresponding ideal adsorbed solution theory (IAST) predictions for CO_2 selectivity from an equimolar CO_2/H_2 mixture.

The IAST predictions and GCMC simulation results agree only in the limit of low pressure and high temperature, where the assumptions of ideal solution behavior are appropriate. At low pressure for all temperatures, the IAST estimates and the mixed-gas GCMC simulation results all approach selectivity estimates calculated from the ratios of the Henry's constants. At the highest temperature investigated, 473K, where CO_2 saturation has not occurred, the IAST prediction, GCMC simulation results, and the estimate using Henry's constants yield the same, constant value for selectivity. Due to the inherently discontinuous nature of the gating transition from zero to saturated adsorption, a non-constant experimental selectivity is expected experimentally.

IAST predicts correctly the decrease in CO_2/H_2 selectivity with increasing pressure at 298K and 373K. Selectivity is consistently under-predicted at 373K, but it underpredicts and overpredicts in different ranges of pressure from 0.1-1MPa and from 2-4MPa respectively at 298K. The discrepancy between the GCMC simulation results and IAST predictions at 298K may find cause in three factors. First, while the average number of H_2 molecules adsorbed per simulation cell is considerably smaller than unity, the standard deviation is relatively large, leading to significant uncertainty in the calculation of selectivity. Second, at lower temperatures the pore loading is high so that the ideality assumption of IAST is not met, leading to deviations of IAST from GCMC mixture results. Third, the inability of the Langmuir model to fully fit the simulated isotherms (Figure 4.1) leads to inaccuracies in the IAST predictions.

The observed trends in adsorption selectivity can be attributed to the degree of saturation of the pore structure with CO_2. At high temperatures such as 473K, adsorption is far from the
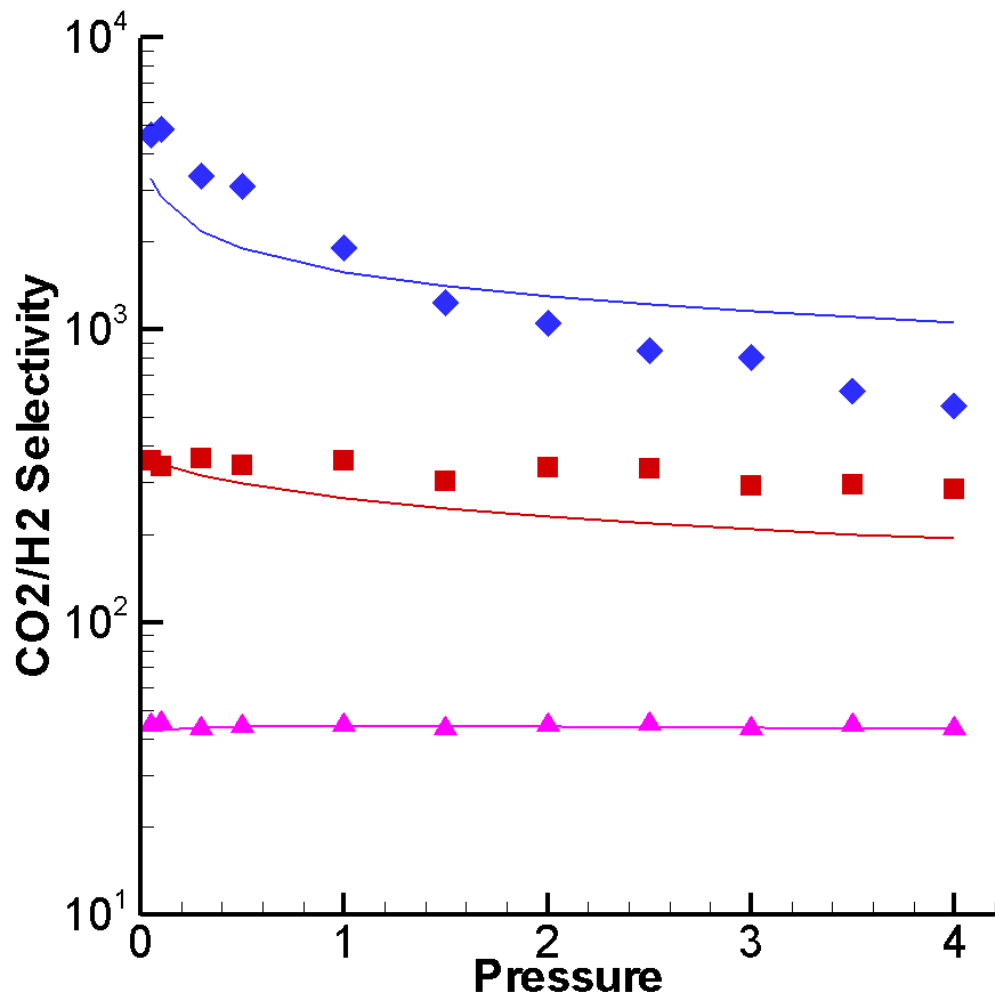
Figure 4.6 Binary mixture CO_2/H_2 selectivity from mixed-gas GCMC simulation (symbols) and IAST calculation (lines). 298K-◇, 373K-□ and 473K-△

saturation limit and the adsorption of both CO_2 and H_2 increase approximately linearly with increasing pressure, leading to selectivity being nearly independent of pressure. However, at lower temperature selectivity of CO_2 over H_2 decreases with increasing pressure. Under these conditions, the pore space is increasingly saturated with CO_2 molecules, limiting further CO_2 adsorption; and so any enhancement of H_2 adsorption via increased pressure shifts selectivity toward H_2. This effect has also been reported for the adsorption selectivity of binary mixtures of different molecular sizes on zeolite adsorbents (Akten et al., 2003; van Tassel et al., 1994).
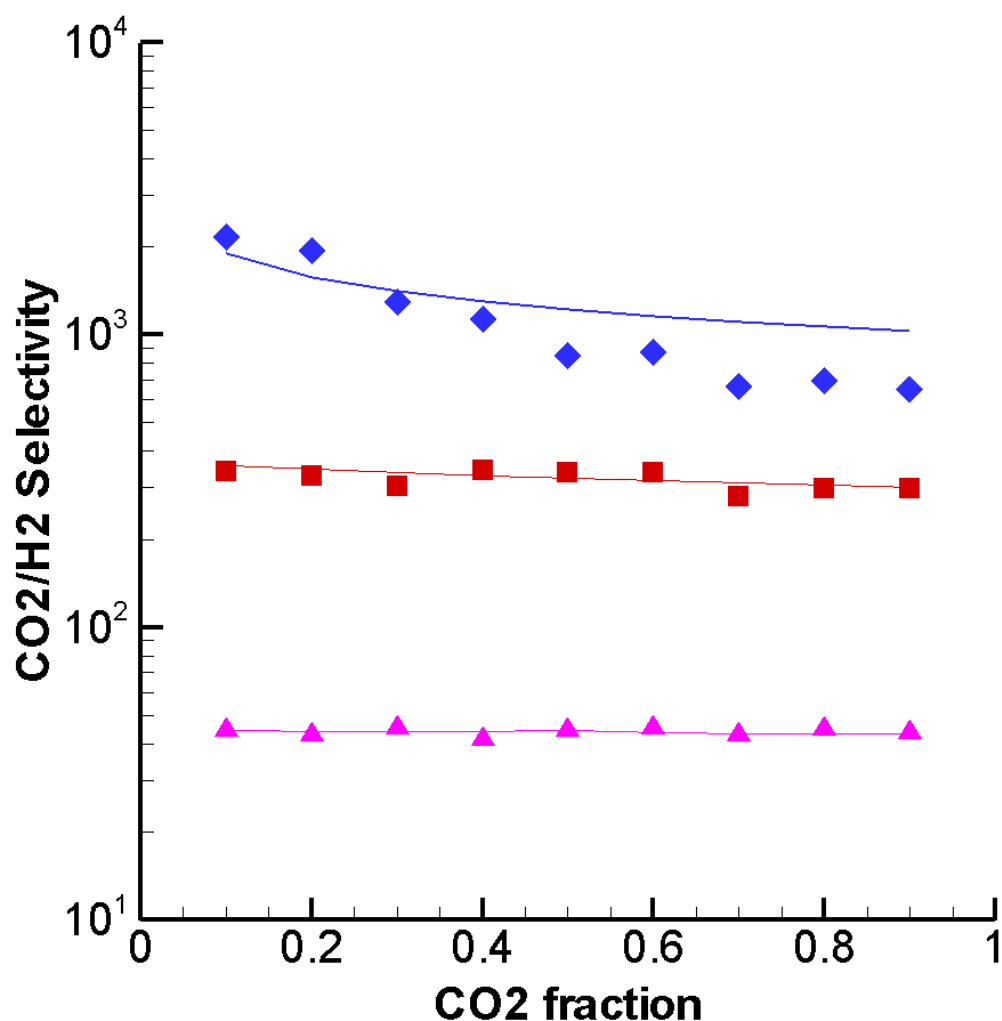
Figure 4.7 CO_2/H_2 selectivity as a function of bulk fraction of CO_2 in the mixture obtained from mixed-gas GCMC simulation (symbols) and IAST calculation (lines). 298K-◊, 373K-□ and 473K-△

The CO_2/H_2 selectivities considered so far have been for equimolar mixtures. It is

practical to examine how the selectivity varies with gas mixture composition. Figure 4.7 presents the adsorption selectivity of CO_2 over H_2 as a function of bulk phase composition at 2.5MPa for the three temperatures above. As expected, selectivity at 473K and 373K are not strongly dependent on bulk gas composition. However, at 298K the selectivity decreases with increasing CO_2 fraction due to saturation of the adsorbent with CO_2. IAST quantitatively matches mixed-gas GCMC results at 473K and 373K. As seen previously, at 298K IAST qualitatively matches the decreasing trend observed in the GCMC results but generally over-predicts the selectivity.

Table 4.2 compares CO_2/H_2 selectivity for adsorption of an equimolar mixture of CO_2 and H_2 onto $Cu(BF_4)_2(bpy)_2$ with selectivities measured for other adsorbents, including the MOFs CuBTC and MOF5. Also shown in Table 4.2 are isosteric heats, q_{st}, for CO_2 adsorption. The predicted selectivities for $Cu(BF_4)_2(bpy)_2$ are generally much higher than those observed for other adsorbents at similar temperatures and pressures, which is consistent with the generally high values predicted for q_{st}. Note, however, that while large q_{st} values promote adsorption and selectivity, they may also inhibit desorption, particularly at low temperatures, requiring careful matching of adsorbents to process conditions.

Material	CO_2/H_2 Selectivity	q_{st}; CO_2 (kJ/mol)	T (K)	P (Mpa)
Coal BPL (GAC)*	90.8	24	303	<1
activated carbon**	86	-	298	1
Zeolite 5A*	740	39	303	<1
MOF-5***	25	-	298	2
CuBTC***	150	-	298	2
$Cu(BF_4)_2(bpy)_2$	~2000	~40-45	298	1
$Cu(BF_4)_2(bpy)_2$	~1000	~40-45	298	2

Table 4.2 Comparison of CO_2/H_2 selectivity and isosteric heats of CO_2 adsorption,q_{st}, for $Cu(BF_4)_2(bpy)_2$ and various porous adsorbents. *(Sircar et al., 1996) **(Cao and Wu, 2005) ***(Yang and Zhong, 2006)

Chapter 5

Hybrid GCMC/MD Simulation of Adsorption into a Flexible Copper-Organic Framework

Using a hybrid Monte-Carlo/molecular-dynamics (GCMC-MD) method, carbon dioxide and nitrogen adsorption onto the metal organic framework (MOF) $Cu(BF_4)_2(bpy)_2$ (bpy=bipyridine) was simulated using a flexible MOF model at temperatures, pressures, and compositions representative of flue gas streams from fossil fuel power plants. This MOF was chosen because it displays a novel CO_2 adsorption behavior in which the crystal structure reversibly transitions from an empty, zero porosity state to a fully-saturated, expanded state at what has been termed the gate pressure. CO_2 adsorption behavior predicted using GCMC-MD followed experimental results much better than results from prior grand canonical Monte Carlo (GCMC) simulations, which used a rigid MOF model. As with the gating behavior observed experimentally, simulation cell volumes increased with increasing pressure, with apparent dissolution of the crystal structure occurring at the highest pressures. Mixed-gas simulations predicted CO_2/N_2 selectivities of $\sim$20-70 at 300 and 350K, which is comparable to many common adsorbents but significantly lower than selectivities predicted using GCMC. Predicted selectivity decreased with increasing CO_2 fraction in the bulk gas phase.

5.1 Simulation Details

Attempts to account for the changes in adsorbent volume associated with the gate-pressure phenomena using the Gibbs ensemble Monte Carlo (GEMC) method (Panagiotopoulos, 1987; Lastoskie et al., 1993b) alone were unsuccessful. (Note: GEMC differs from GCMC

in that GEMC uses multiple, non-rigid simulation boxes. In addition to the usual MC translation and rotation moves, chemical equilibrium between boxes is attained by allowing transfer of adsorbate molecules between boxes, and mechanical equilibrium is achieved by allowing the box volume to change according to the specified pressure.) Specifically, random volume-change moves and random displacements of single atoms or groups of atoms in the MOF did not allow efficient rearrangement and relaxation of the system. Consequently, a hybrid grand-canonical-Monte-Carlo/molecular-dynamics (GCMC-MD) scheme was developed in which blocks of grand canonical MC (GCMC) steps are interspersed with blocks of MD steps to allow for expansion, contraction, and/or relaxation of the structure. The GCMC steps randomly inserted, deleted, translated, and rotated adsorbate molecules in the MOF structure according to the usual GCMC method. After a specified number of MC steps, random velocities were assigned to each particle in the simulation cell using a distribution consistent with the desired temperature, and a specified number of MD steps were carried out. This pattern was repeated to allow equilibration of the system and collection of data.

Swelling of model polymeric gels (Escobedo and de Pablo, 1999; Kenkare et al., 2000) has been simulated using hybrid MD/GCMC methodologies. GEMC simulation has also been previously coupled with molecular dynamics in a hybrid technique (Kotelyanskii and Hentschke, 1995) to investigate swelling of polymer networks by solvents (Aydt and Hentschke, 2000) and binary Lennard-Jones mixtures (Oyen and Hentschke, 2005).

Isotherms for pure and mixed-gas adsorption into a flexible model of $Cu(BF_4)_2(bpy)_2$ were generated via the GCMC/MD method described above using triclinic periodic boundary conditions. Figure 1.4 shows a top view of two, stacked 4x4 layers of the expanded form of $Cu(BF_4)_2(bpy)_2$. Each non-orthogonal simulation cell contained ten 4x4 layers, corresponding to a total of 160 Cu atoms. The open-source MCCCS Towhee software package (http://towhee.sourceforge.net) (Martin and Siepmann, 1999) was used for the GCMC portion of the simulations. The DL_POLY software package (http://www.ccp5.ac.uk/DL_POLY/) was used for the MD portion of the simulations. Control and communication between Towhee and DL_POLY were handled by an external script developed by the author.

Typically, 1000 GCMC moves with an insertion/deletion probability of 20% were interspersed with 100-500 1fs MD steps. Note that because each MD step is a global move, whereas each MC step is typically a local move, one MD step can be taken as roughly equivalent to N MC steps, where N is the number of atoms or molecules in the simulation cell. These alternating GCMC-MD blocks were repeated several hundred times until the number of adsorbed molecules, system energy, and system volume stabilized. The MD simulations were carried out using Verlet leapfrog integration in the isothermal-isobaric

ensemble (NPT) using a Berendeson thermostat and barostat.

Simulated pure CO_2 adsorption isotherms for comparison with experiment were generated at 273K, which is below the CO_2 critical temperature of 304 K. Simulated isotherms were generated for several binary mixtures of CO_2 and N_2 at 300 and 350K and 100kPa to investigate adsorption under realistic process temperatures and pressures. The three-site TraPPE CO_2 and N_2 models, which were optimized to reproduce pure component bulk vapor-liquid equilibria (Potoff and Siepmann, 2001), were used. Each atomic site in the TraPPE models is composed of a Lennard-Jones (LJ) sphere and a partial point charge. The DREIDING force field (Mayo et al., 1990) was used for the $Cu(BF_4)_2(bpy)_2$ model. In addition to non-bonded LJ and electrostatic interactions described previously, the flexible MOF model also includes vibration, bending, and torsion terms from DREIDING to account for the energy and forces associated with covalent bonding. Because the DREIDING forcefield does not include an entry for Cu2+, the parameters for Fe2+ were used as an approximate substitute. Each copper atom was assigned a charge of +2, and the immediately adjacent fluorine atoms were assigned charges of -1. LJ interactions were truncated at 1.4 nm, and long-range electrostatic interactions were calculated using Ewald summation. Excess adsorption versus pressure was calculated from absolute adsorption simulation results using thermodynamic equation of state data for carbon dioxide and nitrogen from the NIST Chemistry WebBook (Lemmon et al., 2005).

5.2 Pure-gas Simulation Results

Figure 5.1 shows experimental and simulation results for CO_2 adsorption into $Cu(BF_4)_2(bpy)_2$ at 273K. Both GCMC-MD results for the flexible MOF model and prior GCMC simulation results for a rigid model are shown. CO_2 adsorption calculated using GCMC-MD followed experimental trends much better than results from the GCMC simulations. GCMC-MD simulations at 1MPa never attained equilibrium. Instead, accumulation of CO_2 in the simulation cell continued to increase, suggesting dissolution of the MOF structure. At pressures above the gate pressure of $\sim$0.35 bar (and below 1 bar) GCMC simulation predicted a saturated capacity of approximately 160g of CO_2 per mg of MOF. This corresponds to two adsorbed CO_2 molecules per pore or two CO_2 molecules per copper atom. Experimental and GCMC-MD isotherms at 273K and 100kPa show lower adsorption amounts of $\sim$140 g/mg (Onishi et al., 2002) and $\sim$125 g/mg, respectively. This is consistent with the experimental sample and GCMC-MD model possessing possible defects and random, pore-occluding atomic motions relative to the idealized crystal structure of the rigid GCMC model.
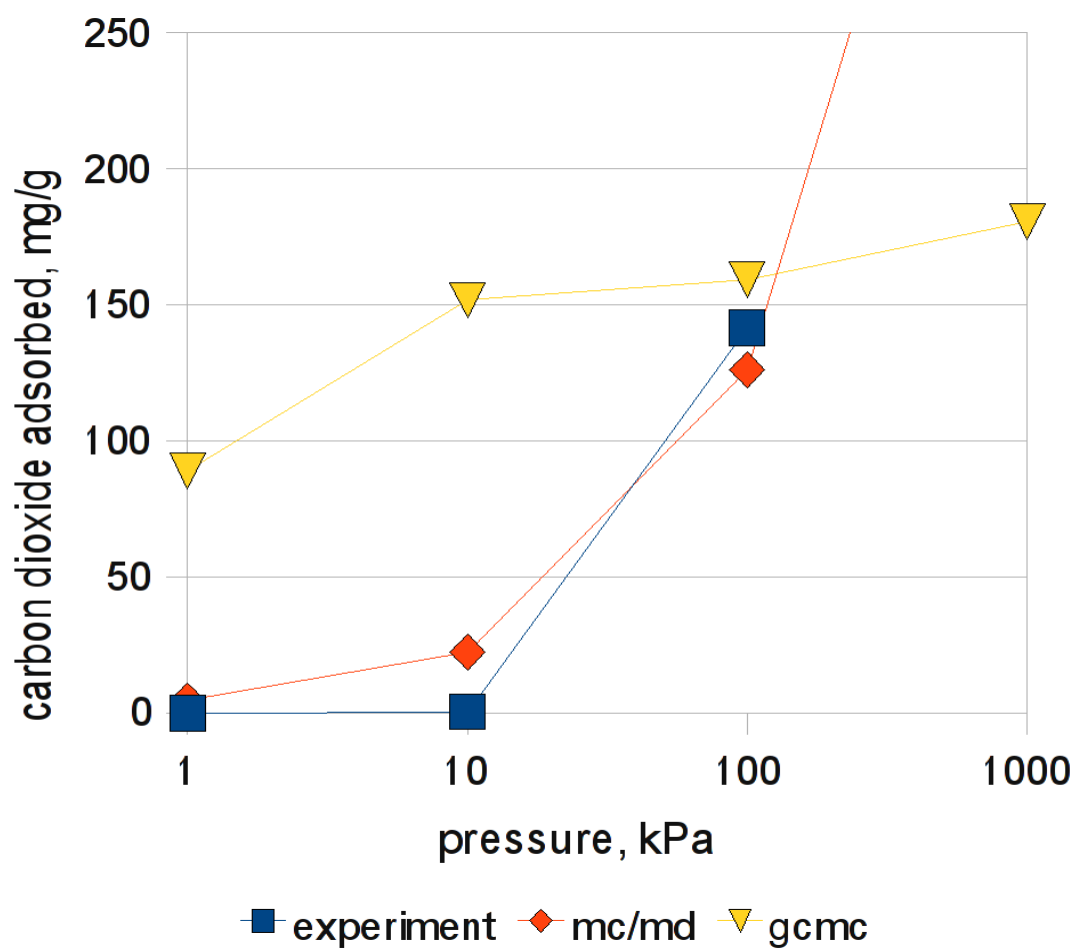
Figure 5.1 Adsorption of CO_2 on $Cu(BF_4)_2(bpy)_2$ at 273K from hybrid MC/MD simulation ($\lozenge$). Standard deviaton values are comparable to the size of the symbols. Experimental results ($\square$ (Onishi et al., 2002)) and GCMC simulation results ($\triangle$) for adsorption on the rigid expanded MOF model are shown for comparison. Lines are a guide to the eye.

Figure 5.2 shows experimentally-determined and GCMC-MD-predicted MOF unit-cell volumes. As with the gating behavior observed experimentally, simulation cell volumes remained relatively constant at low gas pressures and then increased with increasing pressure. Simulation predicted dissolution of the crystal structure at 1MPa. Experimental results were not available for comparison at pressures above 100kPa. The much greater volumes predicted by simulation relative to experiment for empty or low-pressure MOF structures suggest that the relatively simple force field used in this work is not entirely capable of modeling the behavior of $Cu(BF_4)_2(bpy)_2$. Tuning of LJ and/or partial charge parameters could likely result in more accurate behavior, but capturing specific phenomena associated with, for example, $\pi - \pi$ bonding between aromatic rings and charge transfer would likely require the use of a more complex and computationally expensive force field.

Figure 5.3 shows GCMC-MD simulation snapshots of CO_2 adsorption into $Cu(BF_4)_2(bpy)_2$ at 273K. As can be seen in the figure, minimal adsorption has occurred at 1 and 10kPa. At 100kPa significant adsorption has taken place; and at 1000kPa CO_2 molecules have begun separating layers of the MOF, indicating dissolution of the structure.

5.3   Mixed-gas Simulation Results

Figures 5.4, 5.5, and 5.6 show hybrid GCMC-MD results from from mixed-gas simulations at 300 and 350K and bulk gas pressures of 100kPa as a function of the bulk phase CO_2 mole fraction. The amount of CO_2 adsorbed (Figure 5.4) decreases significantly with increasing temperature and is approximately linear in CO_2 mole fraction or partial pressure. CO_2 adsorption capacities predicted by hybrid GCMC-MD are significantly reduced relative to prior GCMC results (Figure 3.3).

At 300 and 350K and low CO_2 partial pressures, MOF unit cell volumes (Figure 5.5) are comparable to those observed at low pressures for pure CO_2 simulations at 273K (Figure 5.2). Volumes remain relatively constant with respect to bulk composition at 350K, but show dissolution behavior at higher CO_2 fractions for 300K simulations. This could be due to 1) increased thermal mobility at 300K relative to 273K and/or 2) momentary adsorption of N_2 molecules, which are smaller than CO_2 and may act as a temporary wedge within the MOF structure to allow subsequent entry of CO_2. Experimental results under similar conditions are not available for comparison at this time.

Selectivity of CO_2 over N_2 is defined as

$$S_{CO_2/N_2} = \frac{x_{CO_2}/y_{CO_2}}{x_{N_2}/y_{N_2}} \qquad (5.1)$$
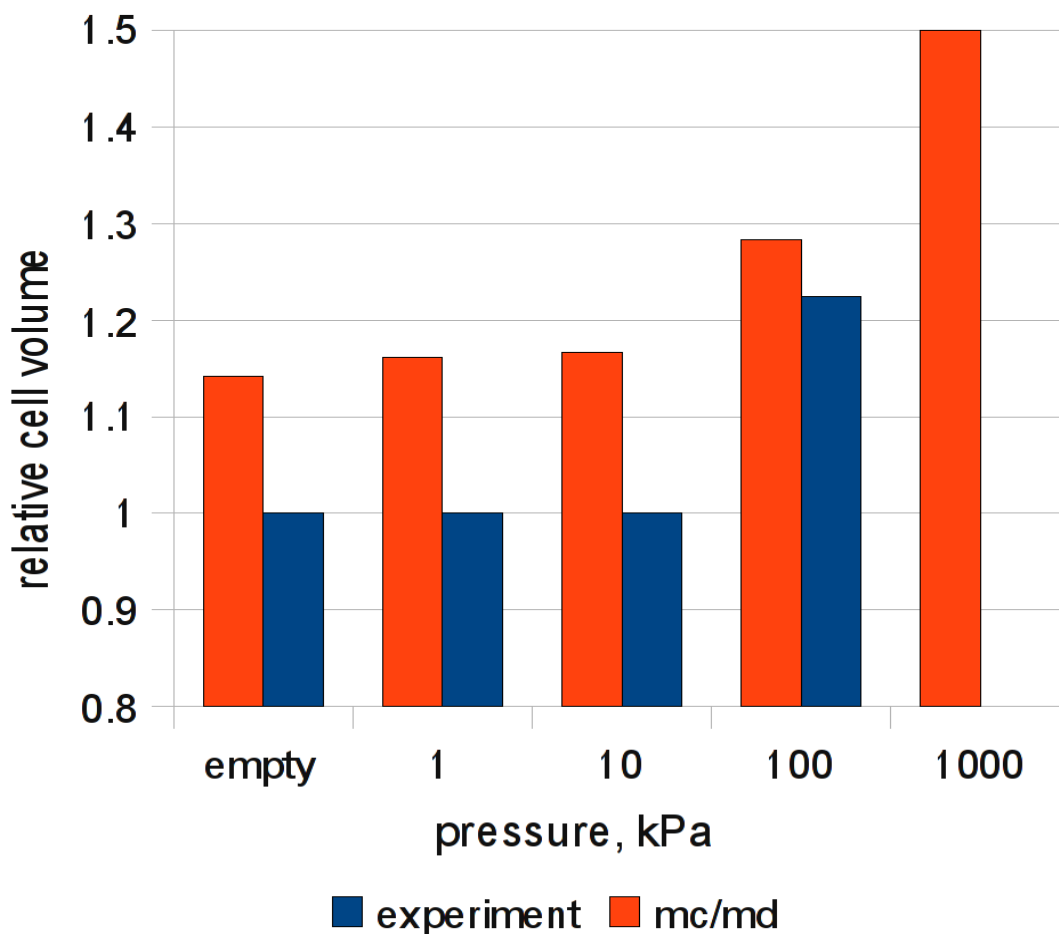
Figure 5.2 Hybrid GCMC-MD simulation cell volumes following adsorption of CO_2 on $Cu(BF_4)_2(bpy)_2$ at 273K for various bulk gas pressures. The 'empty' simulation prediction corresponds to MD relaxation of the crystal structure at 100kPa without attempted insertion of CO_2 molecules. Experimental cell volumes (Onishi et al., 2002) for the empty (non-porous, below gate pressure) and filled (porous, above gate pressure) MOF crystal structure are shown for comparison. All volumes are normalized to the experimental empty cell volume. The bar for simulation at 1000kPa is truncated, as results at this pressure suggest continued expansion and dissolution of the structure.

(a) 1kPa

(b) 10kPa

(c) 100kPa
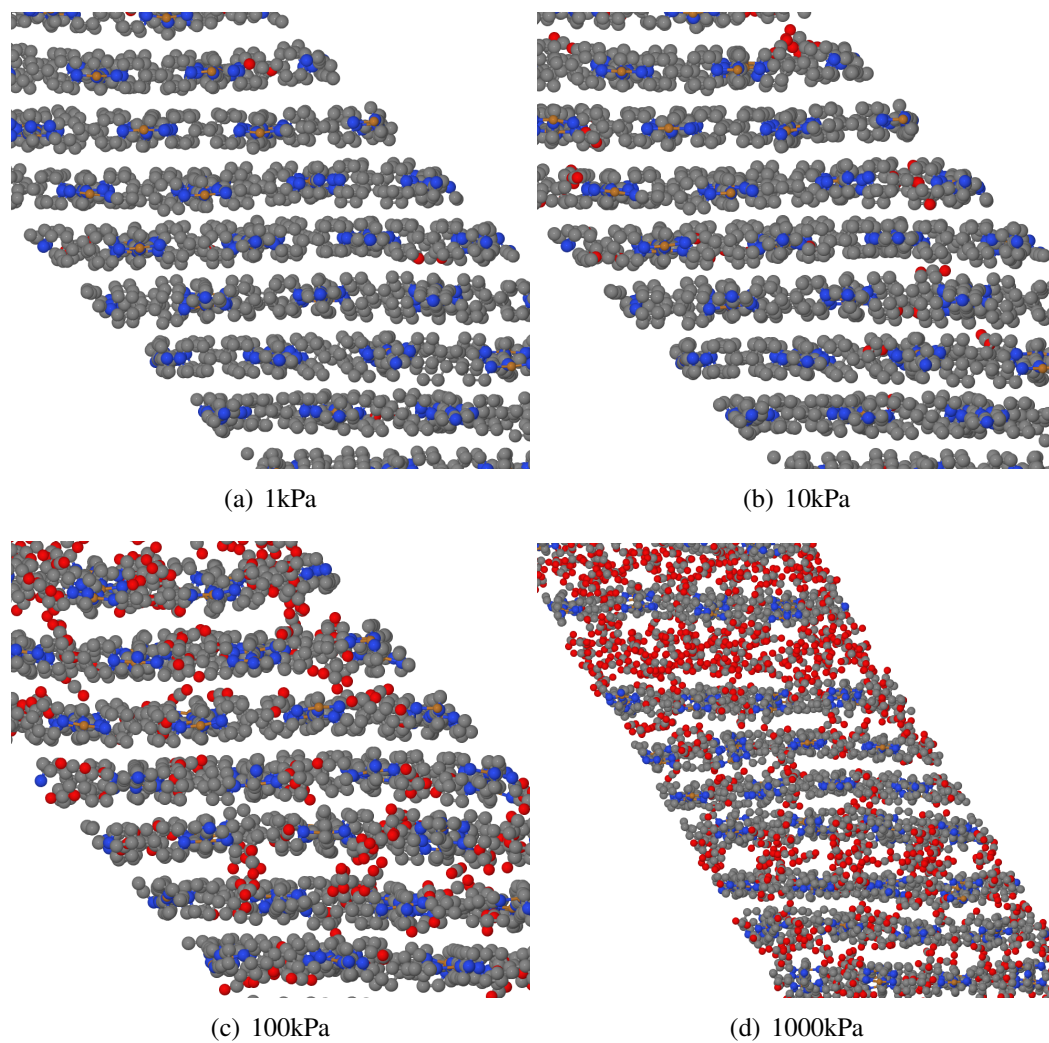
(d) 1000kPa

Figure 5.3 Hybrid GCMC-MD simulation snapshots of CO_2 adsorption on $Cu(BF_4)_2(bpy)_2$ at 273K from pure CO_2 at 1, 10, 100, and 1000kPa. BF_4 groups are omitted for clarity.
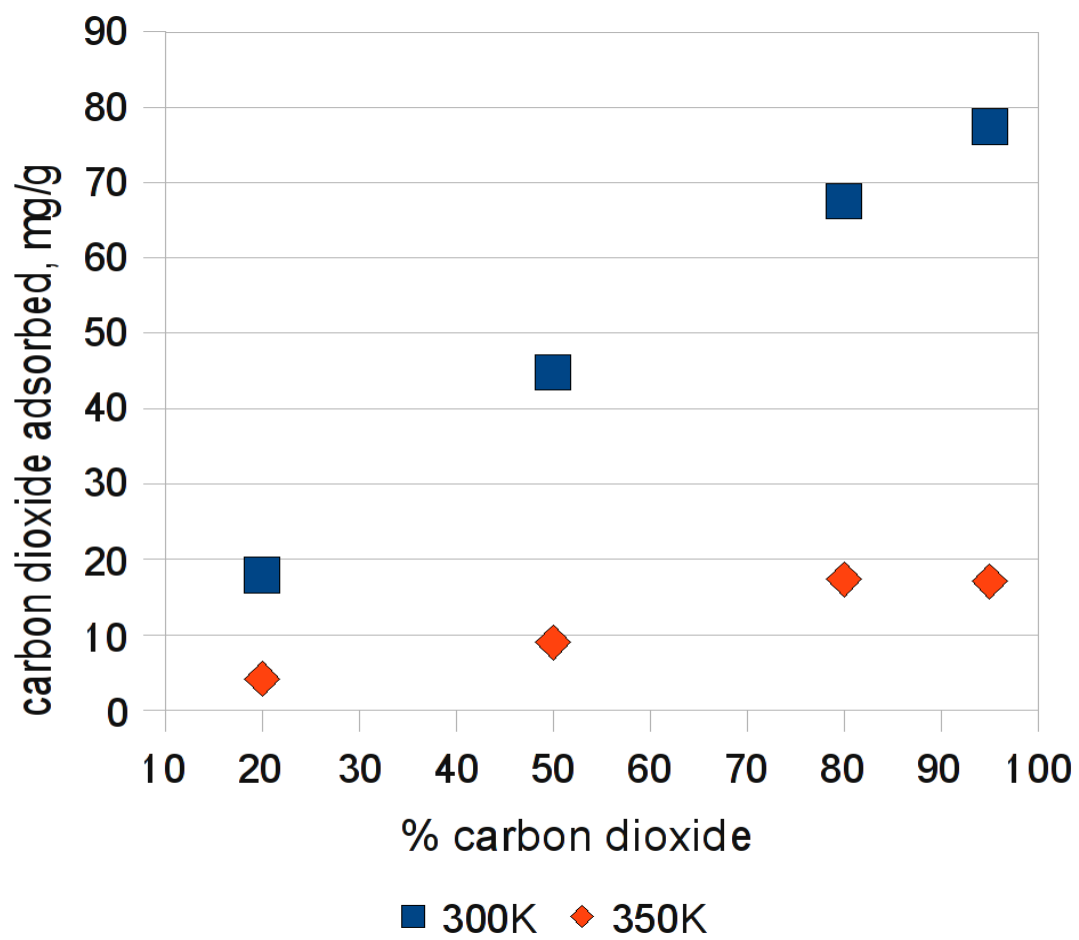
Figure 5.4 CO_2 adsorption amounts predicted by hybrid GCMC-MD simulations of binary mixtures of CO_2 and N_2 for various bulk gas CO_2 mole fractions at 300-□ and 350K-◇. Total bulk gas pressure is 100kPa.
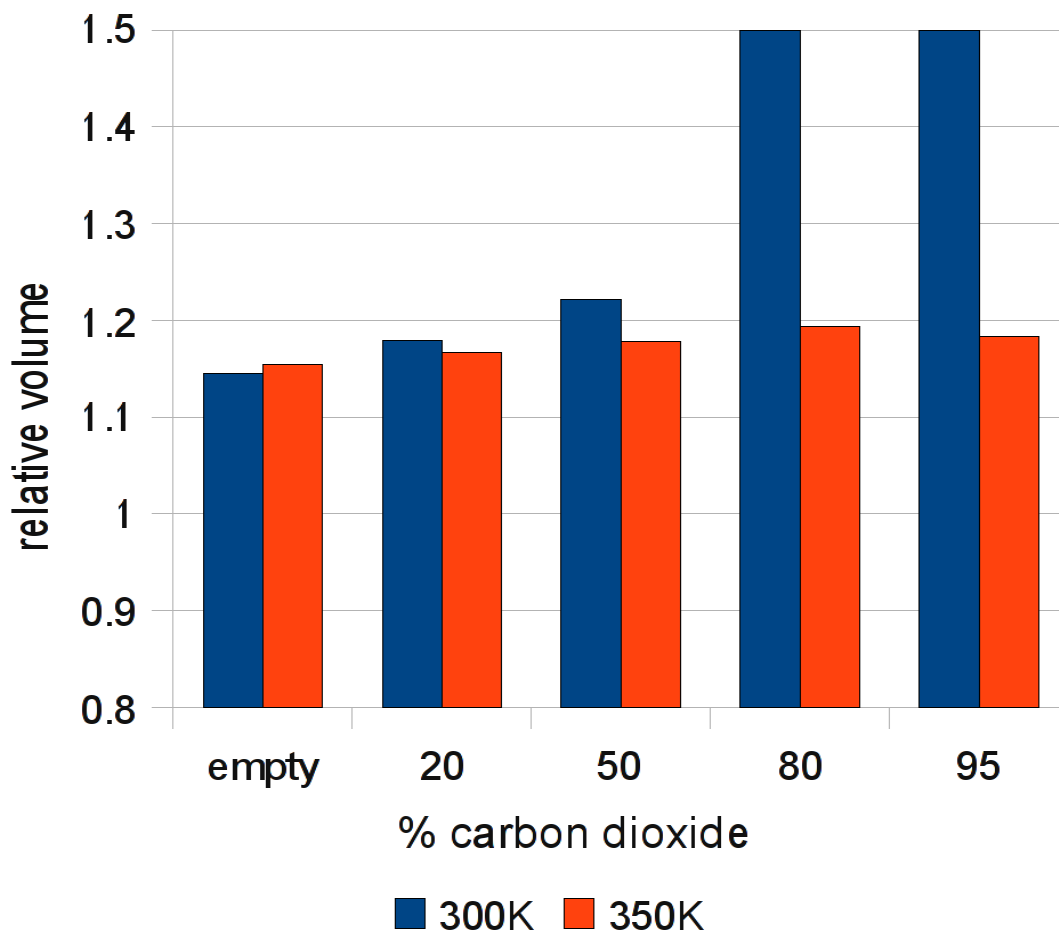
Figure 5.5 Hybrid GCMC-MD simulation cell volumes following mixed-gas adsorption of CO_2 and N_2 on $Cu(BF_4)_2(bpy)_2$ at 300 and 350K. Total bulk gas pressure is 100kPa. The 'empty' simulation prediction corresponds to MD relaxation of the crystal structure at 100kPa without attempted insertion of adsorbate molecules. Volumes are normalized to the experimental empty cell volume (Onishi et al., 2002). The bars for 80 and 95% CO_2 at 300K are truncated, as results at this pressure indicate continued expansion and dissolution of the structure.

where x_a and y_a are the mole fractions of component a in the adsorbed and bulk gas phases, respectively. As seen in Figure 5.6, selectivity is predicted to decrease slightly with temperature and significantly with increasing CO_2 fraction in the bulk phase. These results differ significantly from GCMC-calculated selectivities (Figure 3.5), which were generally much larger, very dependent upon temperature, and relatively constant selectivity with respect to CO_2 fraction in the bulk gas phase. These differences highlight the importance of model and method selection when attempting to predict adsorption behavior in complex materials. Experimental results under similar conditions are not available for comparison at this time.
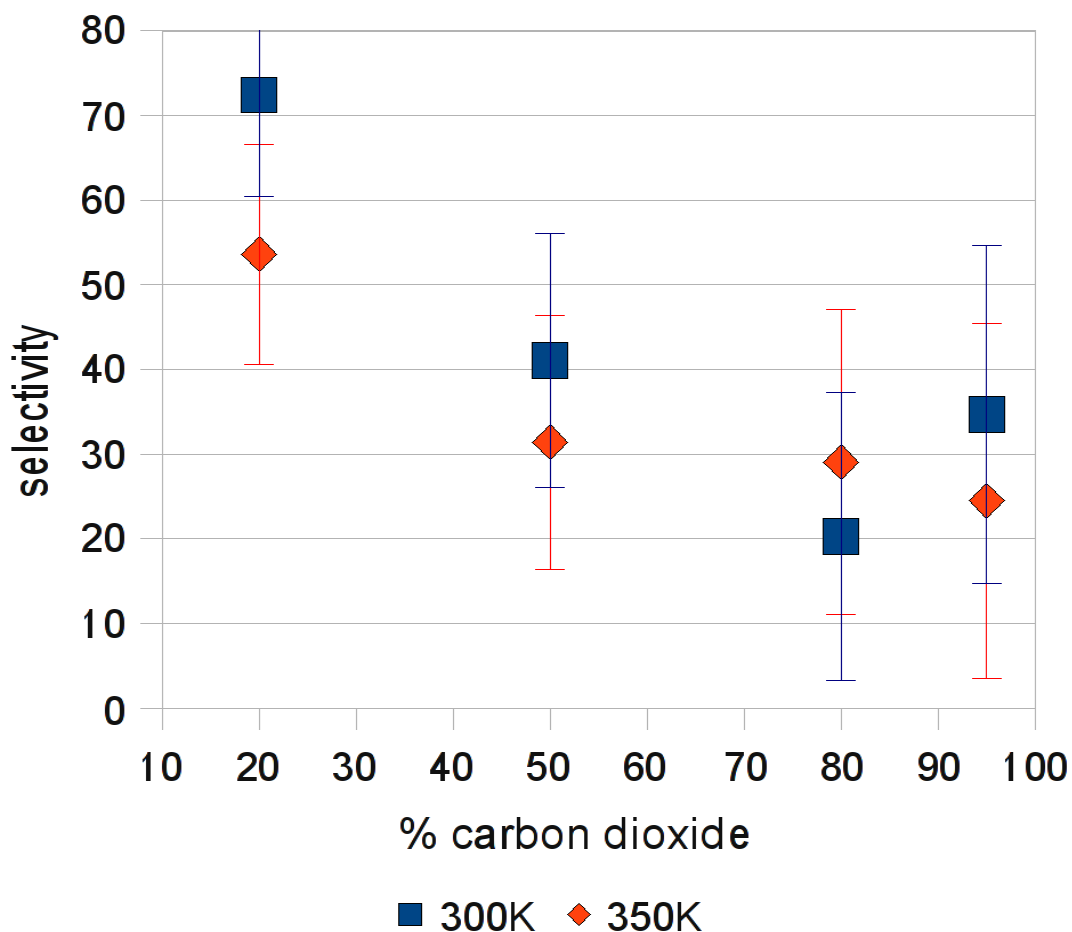
Figure 5.6 CO_2 adsorption selectivities predicted by hybrid GCMC-MD simulations of binary mixtures of CO_2 and N_2 for various bulk gas CO_2 mole fractions at 300-□ and 350K-◇. Total bulk gas pressure is 100kPa. Error bars denote one standard deviation.

Chapter 6

Hybrid GEMC/MD Simulation of Carbon Dioxide Adsorption into Coal

To improve understanding of the molecular processes involved in the storage of carbon dioxide in unmineable coal seams with enhanced coalbed methane recovery, an atomically-realistic, associated, macromolecular model of Upper Freeport bituminous coal was simulated using both molecular dynamics (MD) and a hybrid Gibbs-ensemble-Monte-Carlo/MD method. MD simulation predicted a bulk density of 1.24 g/ml for the dry coal across a wide range of temperatures and pressures associated with CO_2 storage in unmineable coal seams. This density compares favorably with experimental results. The relaxed structures predicted by MD showed evidence of association and stacking of graphitic regions on different macromolecules. Hybrid simulation results showed minimal adsorption of water into the coal matrix. These chararacteristics are both expected for coals of bituminous rank. Consistent with experimental results, carbon dioxide was predicted to adsorb preferentially with respect to methane and induce significant swelling of the structure.

6.1 Model Details

Although useful insights regarding carbon dioxide adsorption were gained from the preliminary studies on heterogeneous model adsorbents generated from modified, graphitic slit-pore structures, these structures clearly do not approach the structural and chemical heterogeneity and flexibility inherent to coal macromolecules. Therefore, in this work an atomically explicit and structurally realistic model of a low-volatile, bituminous coal was implemented to better enable the study of carbon dioxide capture with enhanced coalbed methane recovery (ECBM). A bituminous coal model was selected as coals of this rank are considered representative of those most likely to be encountered in unmineable coal

seams where enhanced coalbed methane recovery is practiced or CO_2 sequestration is contemplated (White et al., 2005). A target density of the unsolvated coal macromolecule in the neighborhood of 1.25 g/ml is desired, in accordance with experimental measurements (Takanohashi et al., 1999).

For this work the chemically-realistic associated coal model of Takanohashi and Kawashima (2002) was used to develop a molecular simulation model of coal for use in the study of CO_2 sequestration and ECBM in unmineable coal seams. The Takanohashi and Kawashima (2002) model was developed through a series of solvent extractions performed on samples of Upper Freeport coal, one of several Argonne premium standard coals commonly used in coal research. Upper Freeport coal is a mid-rank, low-volatile bituminous coal. The elemental composition of Upper Freeport coal is 86.2% carbon, 5.1% hydrogen, 1.9% nitrogen, 2.2% sulfur, and 4.6% oxygen. All of these elements are represented in the proper proportions in the final model.

As described in Takanohashi and Kawashima (2002), samples of Upper Freeport coal were initially extracted with a mixed-solvent composed of carbon disulfide and N-methyl-2-pyrrolidinone (CS_2/NMP). This extraction resulted in a mixed-solvent-soluble extract (MS) and a mixed-solvent-insoluble residue (MI). The MS fraction was then extracted with acetone, resulting in an acetone-soluble fraction (AS) and an acetone-insoluble fraction (AI). The AI fraction was further extracted with pyridine, resulting in a pyridine-soluble fraction (PS) and a pyridine-insoluble fraction (PI).

The initial mixed-solvent extract yield for MS was 59.4 wt% on a dry, ash-free (daf) basis. The extraction yield was later increased to 78-85 wt% through the inclusion of small amounts of additional solvents. This relatively high degree of extraction suggested that Upper Freeport coal is an associated structure composed of non-covalently linked macromolecules of varying molecular weight and chemical composition (Takanohashi and Kawashima, 2002).

Chemical models for the MI, AS, PS, and PI fractions were developed using their measured elemental compositions and NMR spectroscopy (Takanohashi and Kawashima, 2002). Specifically, using ^{13}C NMR for MI and ^{1}H NMR for the remaining extracts, spectra for proposed model molecules were generated and compared with experiment. This process was iterated to generate model molecules that best matched experimental knowledge of elemental compositions, atomic hybridizations, and chemical functional groups for each extract. The final result was a seven-molecule model for Upper Freeport coal with a continuous distribution of molecular weights composed of two MI macromolecules (molecular weight 1419 g/mol and 1374 g/mol), one AS macromolecule (526 g/mol), two PS macromolecules (643 g/mol and 565 g/mol), and two PI macromolecules (1292 g/mol and 886 g/mol). Figures 6.1,
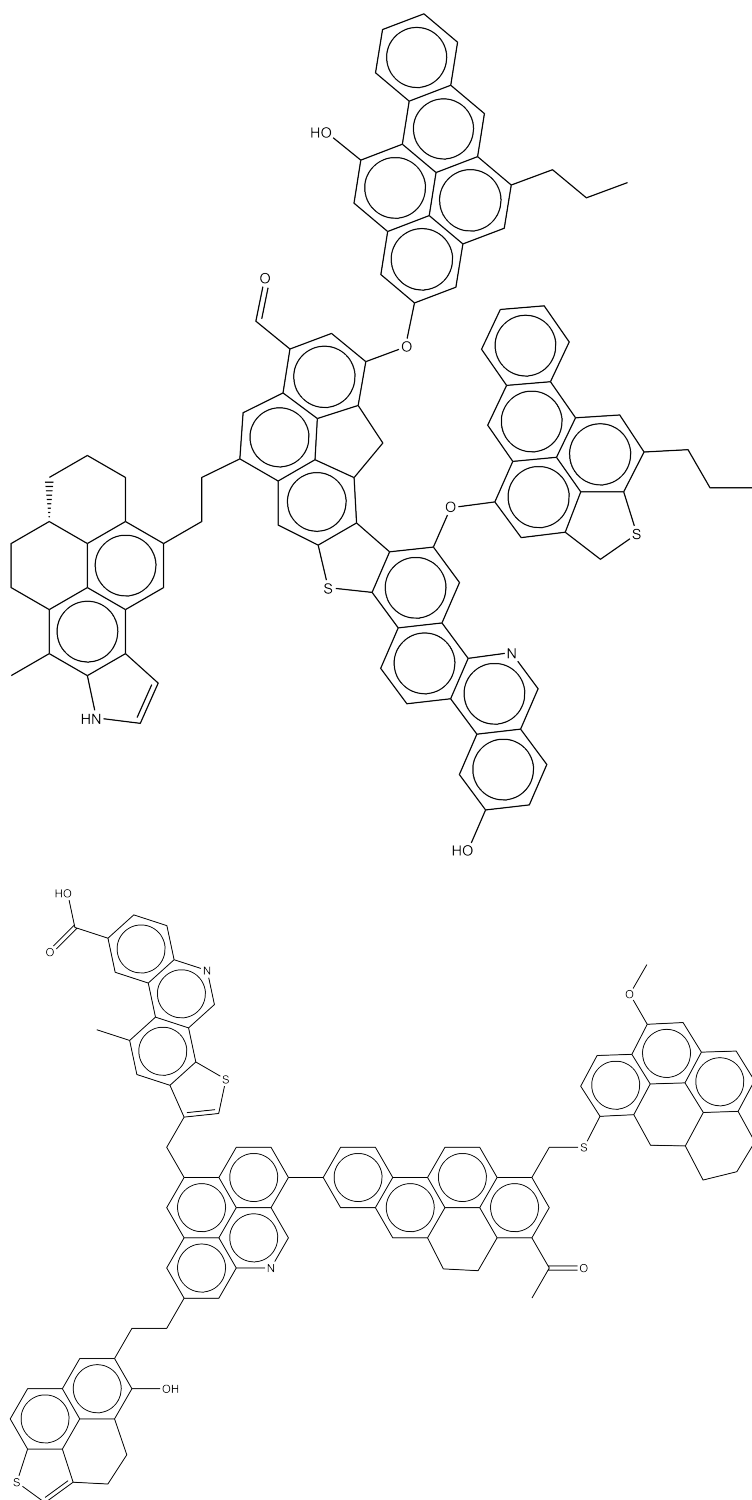
Figure 6.1 Macromolecules comprising the mixed-solvent-insoluble (MI) fraction of the associative Upper Freeport bituminous coal model. Adapted from Takanohashi and Kawashima (2002).
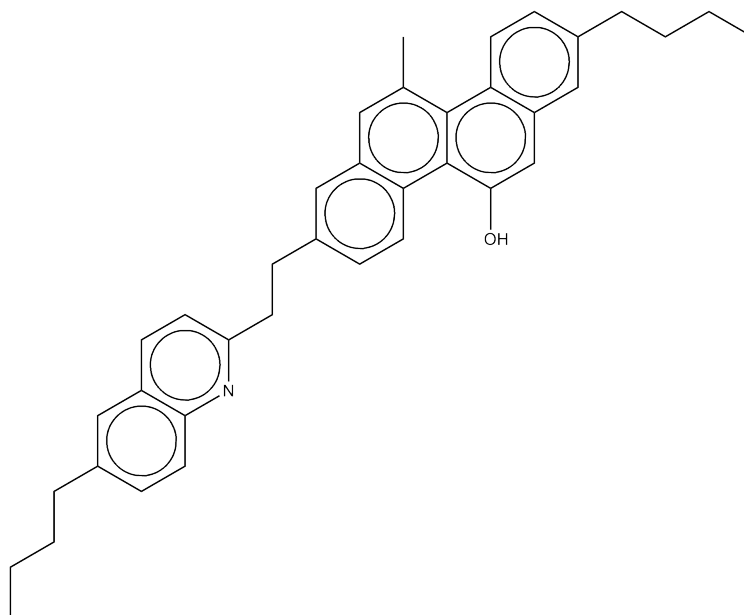
Figure 6.2 Macromolecule comprising the acetone-soluble (AS) fraction of the associative Upper Freeport bituminous coal model. Adapted from Takanohashi and Kawashima (2002).

6.2, 6.3, and 6.4 show the resulting chemical structures for the MI, AS, PS, and PI fractions, respectively.

6.2   Simulation Details

Early simulation attempts using pure Monte Carlo methods failed to relax the model coal structure to the desired density of 1.25 g/ml. Typical densities from MC simulations were instead in the neighborhood of 0.65-0.75 g/ml. As a result, the hybrid grand-canonical-Monte-Carlo/molecular-dynamics method (GCMC-MD) described previously and used to study adsorption in $Cu(BF_4)_2(bpy)_2$ was extended for use with the coal model described above. To allow efficient and simultaneous simulation of the multiple phases present *in situ* during CO_2 sequestration with enhanced coalbed methane (ECBM) extraction, a hybrid Gibbs-ensemble-Monte-Carlo/molecular-dynamics method (GEMC-MD) was implemented. GEMC was originally developed to permit direct study of phase equilibria (Panagiotopoulos, 1987; Lastoskie et al., 1993b). In order to simultaneously simulate multiple phases, GEMC uses multiple, non-rigid simulation boxes. In GEMC the system temperature and the total number of particles are held constant during the simulation. To attain thermal equilibrium, GEMC implements the usual MC translation and rotation moves. Chemical equilibrium between boxes is attained by allowing transfer of molecules between boxes. Mechanical
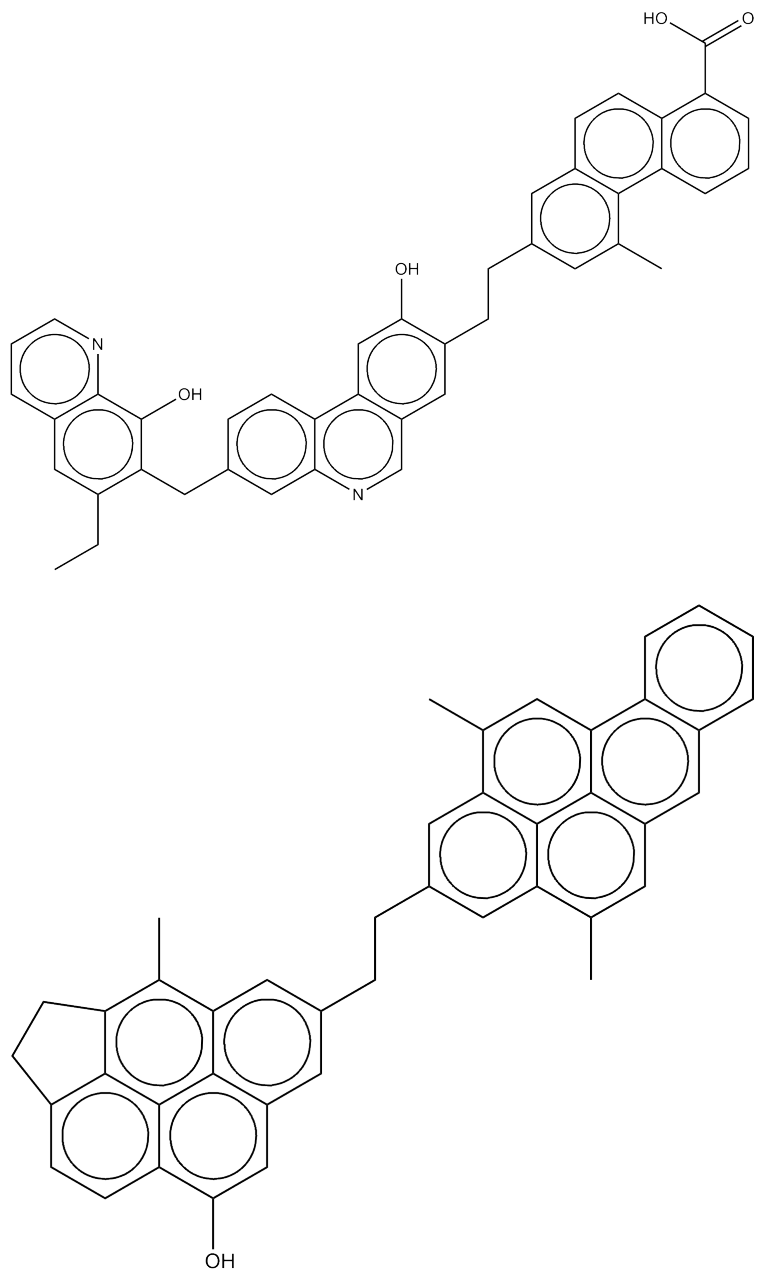
Figure 6.3 Macromolecules comprising the pyridine-soluble (PS) fraction of the associative Upper Freeport bituminous coal model. Adapted from Takanohashi and Kawashima (2002).
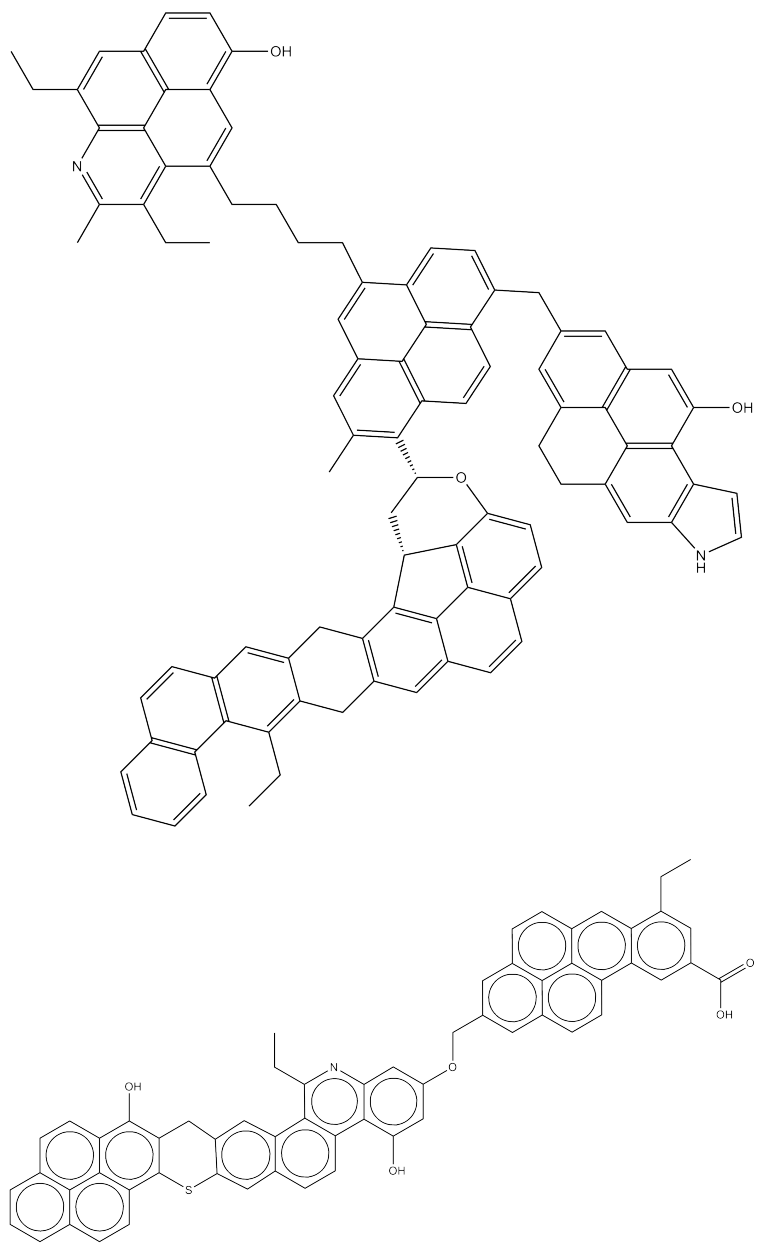
Figure 6.4 Macromolecules comprising the pyridine-insoluble (PI) fraction of the associative Upper Freeport bituminous coal model. Adapted from Takanohashi and Kawashima (2002).

equilibrium is achieved by either allowing the box volumes to vary according to a specified pressure (isothermal-isobaric or NPT GEMC ensemble) or by allowing volume exchange between the simulation boxes, while conserving total system volume (isothermal-isochoric or NVT GEMC ensemble).

Although grand canonical MC would be theoretically capable of simulating adsorption of multiple adsorbates into the coal matrix with a single simulation box by specifying the proper chemical potential for each adsorbate, knowledge of the non-adsorbed phases present would not be simultaneously available. Even more significantly, determination of the proper chemical potentials to specify for the adsorbates under the relevant temperature, pressure, and composition conditions would be problematic at best. In practice, because the non-adsorbed phases are highly non-ideal, the use of GCMC to simulate adsorption in this case would require prior Gibbs ensemble simulations of the non-adsorbed, multi-component phases at the desired state points to determine their chemical potentials. In addition to this not being an inherently more efficient strategy, it is well known that measurements of chemical potential of dense phases, such as liquid water and super-critical CO_2, are prone to error due to the difficulty of inserting test molecules into the fluid. Therefore, in the interest of efficiency, simplicity, elegance, and accuracy, the tools developed previously for hybrid grand canonical MC/MD simulations with MCCCS Towhee and DL_POLY were extended to permit alternate use of Gibbs ensemble MC.

GEMC simulation has previously been coupled with molecular dynamics in a hybrid technique (Kotelyanskii and Hentschke, 1995) to investigate swelling of polymer networks by solvents (Aydt and Hentschke, 2000) and binary Lennard-Jones mixtures (Oyen and Hentschke, 2005). Swelling of model polymeric gels (Escobedo and de Pablo, 1999; Kenkare et al., 2000) has also been simulated using hybrid MD/GCMC methodologies.

Similar to the hybrid grand-canonical-Monte-Carlo/molecular-dynamics scheme used previously, in this hybrid Gibbs-ensemble-Monte-Carlo/molecular-dynamics method, blocks of Gibbs ensemble MC steps are interspersed with blocks of MD steps. As with the usual NPT-GEMC algorithm, GEMC moves randomly translated and rotated adsorbate molecules within all simulation boxes and exchanged adsorbate molecules between all boxes. The GEMC portion of the simulation maintained mechanical equilibrium between the non-adsorbed simulation boxes by allowing the box volumes to vary according to the specified pressure. After a specified number of MC steps, random velocities were assigned to each particle in the coal-containing simulation cell using a distribution consistent with the desired temperature, and a specified number of MD steps were carried out using an NPT ensemble. These MD steps permitted the coal/adsorbate system to relax and the simulation box to expand or contract to maintain the pressure specified in the simulation. This alternating

70

pattern of blocks of MC and MD steps was repeated to allow equilibration of the system and collection of data.

For the most general simulations of ECBM operations, four simulation boxes were used in the NPT version of GEMC to account for intermixing of CO_2, methane, and water and adsorption and desorption to and from the coal matrix. Specifically, one box contained the coal matrix and any adsorbate molecules adsorbed to the coal. The additional three boxes allowed for the presence of a water-rich phase, a CO_2-rich phase (e.g. high-density, super-critical CO_2), and a methane-rich phase (e.g. gaseous methane). Exchange of all three adsorbate molecules was permitted between each of the six resulting pairs of boxes. Simulations involving fewer adsorbate molecules used appropriately fewer simulation boxes.

Isotherms for pure and mixed-gas adsorption into a flexible model of coal were generated via the GEMC/MD method described above using rectangular periodic boundary conditions. Each non-orthogonal simulation cell contained eight copies of each of the seven macromolecules composing the associated bituminous coal model described previously. The open-source MCCCS Towhee software package (http://towhee.sourceforge.net) (Martin and Siepmann, 1999) was used for the GEMC portion of the simulations. The DL_POLY software package (http://www.ccp5.ac.uk/DL_POLY/) was used for the MD portion of the simulations. Control and communication between Towhee and DL_POLY were handled by an external script developed by the author.

Typically, 1000-3000 GEMC moves with an inter-box exchange probability of 20% were interspersed with 100-500 1fs MD steps. Note that because each MD step is a global move, whereas each MC step is typically a local move, one MD step can be taken as roughly equivalent to N MC steps, where N is the number of atoms or molecules in the simulation cell. These alternating GEMC-MD blocks were repeated several hundred times until the number of molecules, system energy, and system volume of each simulation box stabilized. The MD simulations were carried out using Verlet leapfrog integration in the isothermal-isobaric ensemble (NPT) using a Berendeson thermostat and barostat.

The rigid, three-site TraPPE CO_2 model, which was optimized to reproduce pure-component, bulk vapor-liquid equilibria (Potoff and Siepmann, 2001), was used. Each atomic site in the TraPPE model is composed of a Lennard-Jones (LJ) sphere and a partial point charge. Water was simulated using the rigid, three-site TIP/3P model (Jorgensen et al., 1983), which is composed of a central LJ sphere and partial negative charge representing the oxygen atom, and two partial positive charges (and no LJ site) representing the hydrogen atoms. Methane was simulated using the single-site, united-atom representation of CH_4, which is a single LJ sphere without charge or explicit hydrogen atoms, from the DREIDING force field (Mayo et al., 1990). The DREIDING force field was also used to produce

an atomically explicit representation of the associative bituminous coal model described previously. In addition to non-bonded LJ and electrostatic interactions, the flexible coal model also includes vibration, bending, and torsion terms from DREIDING to account for the energy and forces associated with covalent bonding. Use of this force field allows deformation and swelling of the coal matrix upon solvation by carbon dioxide, methane, and/or water. During the course of the simulations, LJ interactions were truncated at 1.4 nm, and long-range electrostatic interactions were calculated using Ewald summation. Where applicable, excess adsorption versus pressure was calculated from absolute adsorption simulation results using the density of the non-adsorbed phase calculated during the GEMC portion of the simulations.

6.3   MD Simulation Results

Table 6.1 lists the bulk densities of randomized and relaxed assemblies of the associated bituminous coal model at temperatures of 295, 320, and 345K and pressures of 0.1, 1, 3, and 10 MPa. These temperatures and pressures were chosen as representative of a range of values found in laboratory experiments and actual sub-surface carbon dioxide sequestration and enhanced coalbed methane recovery operations. For example, taking 1000m as a realistic depth for an unmineable coal seam, the unperturbed hydrostatic pressure would be approximately 10 MPa. Following drawdown of formation water during methane extraction, formation pressure will be be reduced near extraction wells. Regarding temperature, 25 to 50 degrees C per km of depth is a realistic range of temperature gradients covering both "cold" and "warm" formations. Again assuming a depth of 1000m and a surface temperature in the neighborhood of 295K, 320 and 345K span a range of temperatures likely observed in an unmineable coal seam.

Bulk density was calculated by simply dividing the mass of atoms in the simulation cell by the simulation cell volume. As can be seen in Table 6.1, bulk coal density is predicted to be relatively insensitive to temperature and pressure within the range of conditions studied. This indicates that relatively strong intermolecular association and close-packing of relatively immobile coal macromolecules is the case when adsorbate molecules are absent. The average value for bulk density was approximately 1.24 g/ml. This is conistent with the range of values found experimentally (White et al., 2005) and compares favorably with the experimental value of 1.3 g/mol found for Upper Freeport coal (Takanohashi and Kawashima, 2002).

Figure 6.5 shows a simulation snapshot at 295K and 1MPa of a randomized and relaxed

assembly of eight copies each of the seven macromolecules comprising the associated Upper Freeport bituminous coal model desrcribed previously. Note that there appears to be significant association or layering of the graphitic or aromatic regions of different molecules. This is consistent with experimental results, which have found that higher-rank coals often contain crystalline regions composed of multiple, stacked, graphite-like layers, interspersed with amorphous, glassy regions (Marzec, 2002; Lu et al., 2001).

T, K	P, Mpa	density, g/ml
295	0.1	1.24
295	1	1.24
295	3	1.24
295	10	1.24
320	1	1.23
320	3	1.23
320	10	1.24
345	1	1.23
345	3	1.23
345	10	1.23

Table 6.1 Predicted bulk densities for random assemblies of Upper Freeport associated coal model fragments. Structures were relaxed using isothermal-isobaric (NPT) molecular dynamics simulations at the indicated temperatures and pressures.

6.4 Hybrid GEMC/MD Results

For simulations of adsorption into dry coal, three simulation boxes were used: one for coal and one each for potential CO_2- and CH_4-rich phases. Each simulation used eight copies each of the associated coal macromolecules described previously. A total of 1000 molecules each of CO_2 and CH_4 were used in the dry-coal simulations. For simulations in the presence of water, an additional box and 1000 water molecules were added to the system. For all of the conditions studied, with temperatures varying from 295 to 345K and pressures from 0.1 to 10MPa, CO_2 and CH_4 were predicted to form a single, perfectly miscible phase, resulting in two simulation boxes containing identical mixtures of CO_2 and CH_4 at identical densities. Slight CO_2 absorption and negligible CH_4 absorption into the water phase was predicted. This is consistent with what might be expected based upon the properties of water, carbon dioxide, and methane. It should be noted, however, that both the carbon dioxide and water models were originally developed to reproduce primarily pure-component behavior. There was no provision in the models or in the simulations to allow for reaction of carbon dioxide
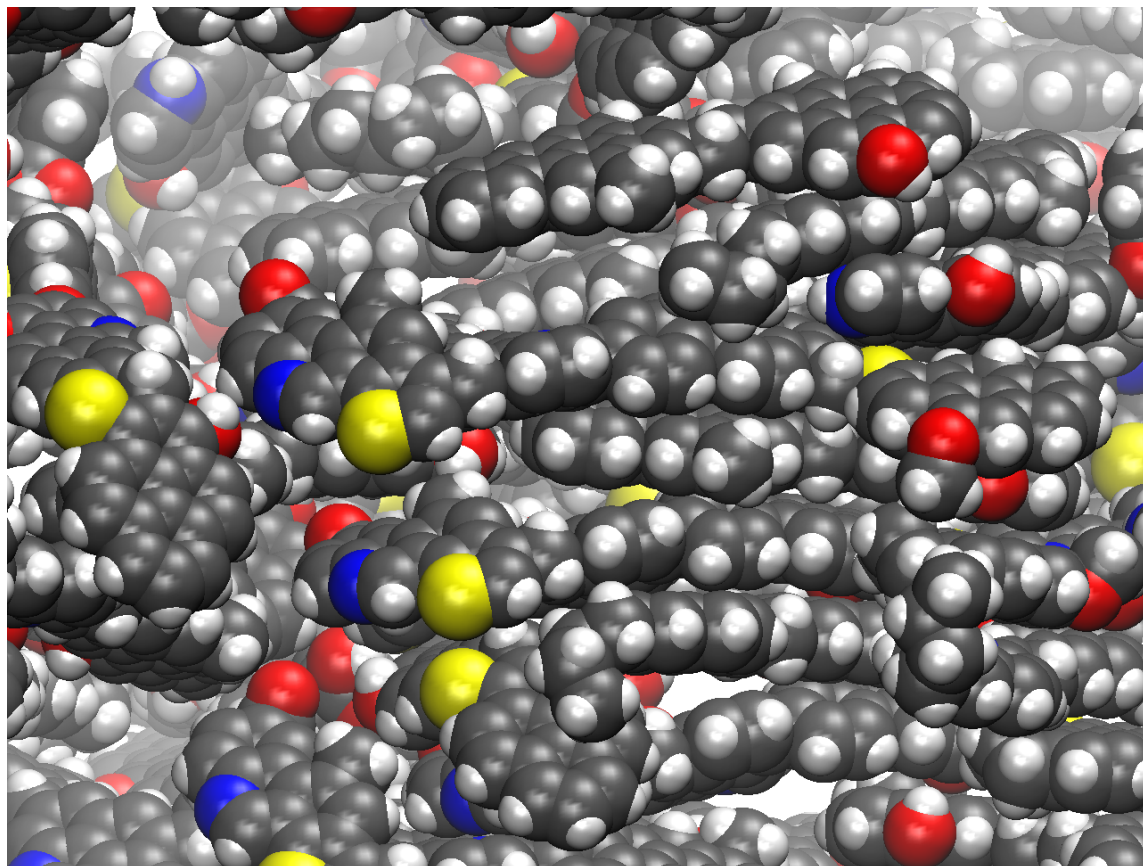
Figure 6.5 Simulation snapshot of associated coal model structure at 295K and 1MPa with no adsorbate present. The simulation cell is comprised of eight copies of each of the seven model coal macromolecules. The simulated bulk density is 1.24 g/ml. Carbon is shown in gray; oxygen, red; nitrogen, blue; sulfur, yellow; and hydrogen, white.

and water to form carbonic acid. Therefore actual CO_2 dissolution into the water phase may be greater than that predicted in these simulations, which may skew simulation results toward greater CO_2 availability for adsorption into the associated coal matrix.

Simulations consistently predicted relatively little water adsorption into this model coal. This is consistent with experimental results, in which less-evolved, lower-rank coals, which still possess significant heteroatom content, exhibit much greater loss of mass and volume upon drying relative to higher-rank coals with more graphite-like structure (White et al., 2005).

Selectivity of CO_2 over CH_4 is defined as

$$S_{CO_2/CH_4} = \frac{x_{CO_2}/y_{CO_2}}{x_{CH_4}/y_{CH_4}} \tag{6.1}$$

where x_a and y_a are the mole fractions of component a in the adsorbed and bulk gas phases, respectively. Table 6.2 lists CO_2/CH_4 selectivities calculated from hybrid GEMC-MD simulations at 345K for adsorption of carbon dioxide and methane into both dry coal and into coal in the presence of liquid water.

Pressure (MPa)	Moisture Content (wt% H_2O)	Selectivity
0.1	0	2.3
1	0	2.9
10	0	1.6
10	0.23	1.2

Table 6.2 Selectivity of CO_2 over CH_4 in the associated bituminous coal model at 345K.

Figure 6.6 is a simulation snapshot of the associated coal structure (depicted in ball-and-stick format) in equilibrium with an equimolar mixture of carbon dioxide and methane (both depicted according to their van der Waals radii) at 295K and 1MPa. The pore spaces in the coal structure have expanded as a result of adsorption of carbon dioxide and methane. Although not as easily seen as in Figure 6.5, stacking and association still occur between aromatic, graphitic regions of adjacent macromolecules. Adsorption is prevented within these regions. Based upon this observation, lower-rank coals (e.g. lignite), with fewer and/or smaller graphitic sections, and higher-rank coals (e.g. anthracite), with more and/or larger graphitic sections, would both be expected to exhibit different adsorption and swelling behavior relative to this bituminous coal under similar conditions. This is consistent with experimental results, which generally show that adsorption and swelling both depend strongly upon coal rank.
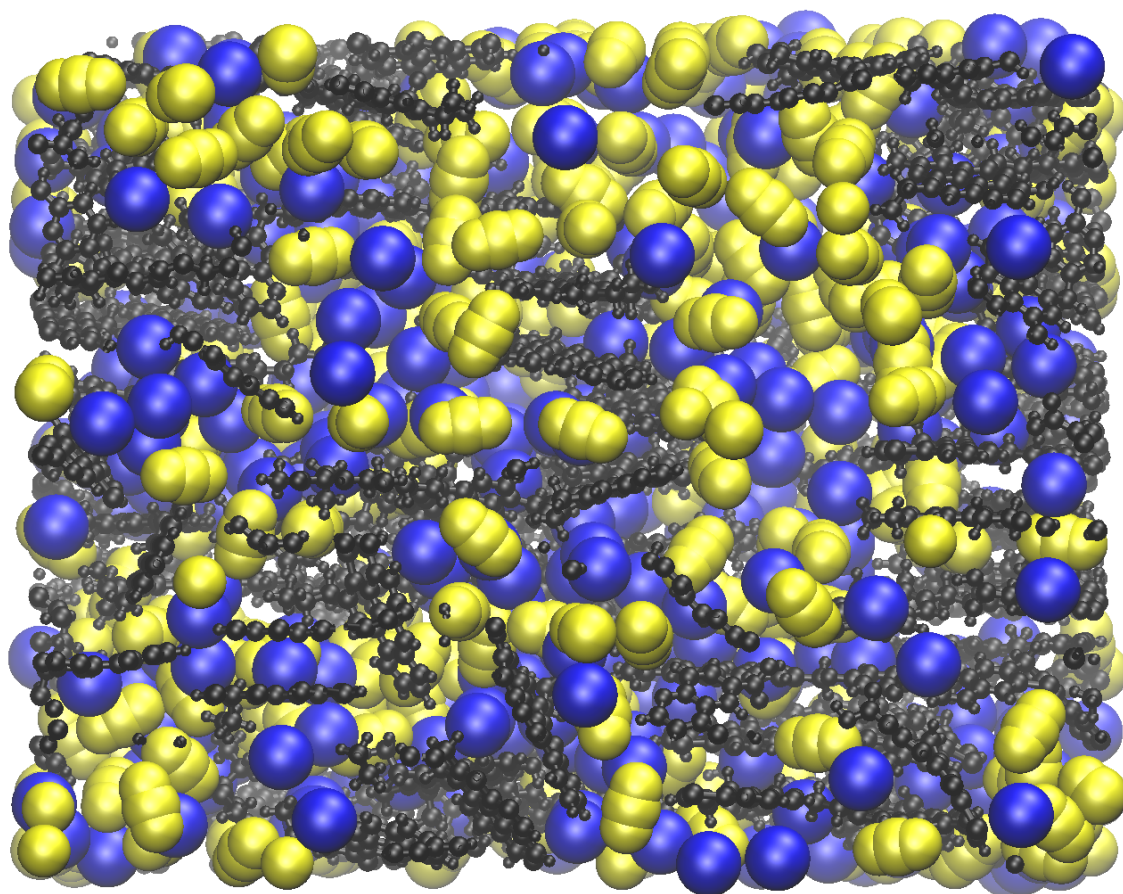
Figure 6.6 Simulation snapshot of associated coal model structure (black, ball-and-stick representation) in equilibrium with an equimolar mixture of carbon dioxide (yellow) and methane (blue) at 295K and 1MPa. The simulation cell is comprised of eight copies of each of the seven model coal macromolecules.

Chapter 7

Conclusion

Carbon dioxide is a greenhouse gas with a long residence time in the atmosphere, and it plays a significant role in determining the planet's climate. Atmospheric carbon dioxide concentrations have been steadily increasing since the start of the industrial age, and it is now widely accepted that anthropogenic emission of CO_2 to the atmosphere has contributed to a general warming of the Earth's temperature. Atmospheric CO_2 concentration is expected to continue to increase significantly as developed and developing nations burn fossil fuels to release energy and drive their economies. Although fossil fuels are an inherently finite resource, significant climate change is predicted to occur long before our fossil fuel resources are depleted. While climate models differ in the extent and details of their predictions, the threat of climate change should not be ignored.

As a modern society, we have built institutions and infrastructure to increase our efficiency and economic output; and we are now inherently dependent upon these inventions. The true threat of climate change isn't necessarily global catastrophe, although that has occasionally been forecast. Instead, we are probably more likely threatened by significant and sustained economic loss as shifts in climate make our current systems unsustainable. For example, rising sea levels and/or increased tropical storm intensities could force a choice between costly protection measures or abandonment of current coastal regions. Similarly, shifts in temperature and rainfall could render existing food-producing regions unproductive, causing significant social disruption and unrest.

Reducing atmospheric carbon dioxide emissions will undoubtedly require time, money, and commitment. It is suggested, however, that this may be overall less costly than the alternative scenario described above. The evolving social and political climate seems to share this perception, as legislation to limit and/or tax carbon emissions, particularly in developed nations, is expected to become more stringent over the next several years. As a result of such legislation, regardless of one's personal views regarding the spectre of

global warming, emitting carbon to the atmosphere will become increasingly expensive, which, along with concern for the environment, is driving renewed efforts to increase energy efficiency and develop renewable alternatives to fossil fuels.

However, the world's appetite for energy continues to grow, and improved efficiency and investment in renewable energy will not be able to satisfy that demand at any time in the foreseeable future. Further, our existing infrastructure investment and the continued abundance and relative low cost of fossil fuels guarantee that fossil fuels will continue to be used for energy for at least the next several decades. This reality provides significant motivation to develop and apply technologies that permit clean burning of fossil fuels with reduced atmospheric carbon dioxide emission.

Because fossil fuel electric power plants are responsible for approximately 30% of the total atmospheric carbon emission, and because they are large, stationary point sources, fossil fuel power plants, particularly coal-burning plants, are attractive initial targets for implementation of carbon dioxide capture and storage (CCS) strategies. In CCS carbon dioxide is separated, concentrated, and compressed from a process gas (e.g. from post-combustion flue gas in a conventional plant or from pre-combustion syngas at an advanced, IGCC facility) and then transported to a storage location (e.g. a deep saline aquifer, depleted oil or gas field, or unmineable coal seam), where it is sequestered away from the atmosphere for a geologically long time. Unfortunately, current CCS technology adds significantly to the cost of the electricity produced, with most of the increased cost resulting from the capture part of the operation.

Current CCS practice uses monoethanolamine (MEA) absorption to capture CO_2 from flue gas. MEA scrubbing is costly due to corrosion issues and the large amount of energy required to regenerate the solvent between cycles. As a result, significant research is underway to identify and develop alternatives to MEA absorption. One of these alternatives is CO_2 capture via selective adsorption onto porous solids. Although traditional industrial adsorbents do not provide a cost savings relative to MEA absorption, there exists a class of materials, referred to as metal-organic frameworks (MOFs), with the potential to be tuned to provide superior adsorption performance under specified process conditions. This tuning is facilitated by altering the chemical and structural properties of the metal-organic material, which is built from metallic or metal-containing vertices connected by organic linker molecules.

Literally hundreds of MOFs have been synthesized, and countless more have yet to even be imagined, but random synthesis and testing of these new materials is inherently slow and expensive. The pharmaceutical industry routinely uses molecular simulation tools for new drug research, because it allows them to more efficiently produce better drugs specifically

tailored to the desired application. With similar motivation, much of the research performed during the course of the work described herein was aimed at developing knowledge and tools necessary to rationally design new MOFs, in particular a novel class of flexible MOFs. At relevant process conditions, the flexible MOF studied was predicted to be comparable to current high-performance adsorbents with respect to CO_2 capacity and ease of regenerability. Selectivities of CO_2 relative to nitrogen (in flue gas) and hydrogen (in syngas), however, were predicted to be higher than most common adsorbents, suggesting that MOFs of similar design might provide high-performance CO_2 capture alternatives. As no MOF adsorbents have been synthesized or implemented at industrial scale, more extensive cost analysis would be required before a direct comparison with MEA absorption could be made.

After CO_2 is captured, it must be stored. An ideal storage location would be near the source, have a large CO_2 storage capacity, provide safe and reliable long-term storage of the injected CO_2, and be low-cost. Deep saline aquifers are widespread and generally possess the first three qualities, and they will likely be the typical storage location for CO_2 if CCS becomes widespread. Unmineable coal seams, however, also offer the potential for profit during CO_2 storage. Specifically, injection and adsorption of CO_2 into the coal induces desorption of methane, a valuable and relatively low-carbon energy source. Because fossil fuel power plants are frequently sited in regions possessing coal deposits, CO_2 storage within unmineable coal seams is an attractive option to pursue for early adoption of CCS.

The technology required for CO_2 injection is well-established in the oil and gas industries. The only significant barrier to large-scale implementation of CO_2 storage in unmineable coal seams is instead the need to understand coal behavior well enough to optimize the injection/extraction process and to validate the safety and effectiveness of long term CO_2 storage. Coal is an inherently complex, heterogeneous, and highly variable material. Methane and CO_2 capacities and diffusivities vary with temperature, pressure, moisture, coal rank, et cetera. Coal shrinks following methane loss, and CO_2 adsorption can cause the coal to swell and become flexible, inhibiting further injection and potentially destabilizing a geological formation. These behaviors must be better understood before unmineable coal seams can be confidently and reliably used for long term storage of CO_2. Complimenting laboratory experimentation and theory, computer simulation can help to achieve this understanding by permitting flexible investigation of injection/extraction behavior across a wide range of time- and length-scales and possible operating conditions. Because information at the molecular scale is needed to understand and better control behavior at larger scales, methods and models for the simulation of coal behavior at the molecular scale were developed as part of this work. Initial studies using these molecular simulation tools confirmed that they were able to reproduce the swelling and competitive adsorption behavior observed in real coals.

Further research should seek to further improve and validate these models and methods and then apply them to the optimization of field-scale operation and long-term CO_2 storage.

Detailed summaries describing the results of this body of work are provided in the following section. The last section suggests areas in which the current work can be beneficially extended.

7.1 Summary of Current Work

7.1.1 Adsorption on Heterogeneous Solids

To improve understanding of adsorption into heterogeneous, microporous solids such as coal and activated carbon, GCMC simulations were carried out to study adsorption of CO_2 into graphite-based model slit pores with surfaces of varying chemical and structural heterogeneity. The pressure at which pore filling with CO_2 occurred varied over approximately one order of magnitude for pores in the size range between 1.35 nm and 2.4 nm. Electrostatic adsorbate-adsorbent interactions significantly influenced adsorption onto model surfaces. Increasing the surface density of oxygen-containing functional groups generally increased CO_2 adsorption and lowered the pore filling pressure. However, exceptions were noted, and in some cases, outwardly small topological differences between surfaces resulted in very different isotherms. For coal-like model pores with explicit charge interactions, low-pressure CO_2 uptake was significantly enhanced, and excess adsorption at the saturation pressure was slightly increased, relative to CO_2 adsorption in comparably sized graphite slit pores.

7.1.2 Metal-Organic Frameworks and Carbon Dioxide Capture

To evaluate the potential use of novel metal-organic frameworks (MOFs) to capture CO_2 from fossil fuel power plants, GCMC simulation was used to analyze pure- and mixed-gas CO_2 adsorption into $Cu(BF_4)_2(bpy)_2$, a flexible metal-organic latent porous crystal adsorbent. Simulated adsorption capacity at 273K agreed well with experimental measurements. $Cu(BF_4)_2(bpy)_2$ was predicted to have CO_2 heats of adsorption comparable to other common physi-adsorbents. For post-combustion CO_2 capture at typical cooled flue gas temperatures and CO_2 partial pressures above the gate pressure, $Cu(BF_4)_2(bpy)_2$ was predicted to have CO_2 adsorption capacities comparable to current, high-performance, commercial adsorbents. CO_2 selectivities relative to N_2, however, were predicted to be much higher, suggesting that similar engineered adsorbents may permit lower-cost flue gas CO_2 capture.

For pre-combustion capture of CO_2 from syngas at integrated gasification combined-cycle (IGCC) power plants, simulation results generally predicted slightly lower capacities and much higher selectivities for CO_2 over H_2 relative to other high-performance microporous materials. For realistic pre- and post-combustion capture process conditions, predicted selectivities decreased significantly with increasing temperature and were relatively independent of composition.

Extending the previous GCMC study that used a rigid model of $Cu(BF_4)_2(bpy)_2$, a hybrid Monte-Carlo/molecular-dynamics (MCMD) method was developed to analyze pure- and mixed-gas CO_2 adsorption into a flexible model of $Cu(BF_4)_2(bpy)_2$. Simulated CO_2 adsorption at 273K closely followed experimental results. Consistent with experimental results, simulation predicted relatively negligible adsorbent swelling at low CO_2 pressures, followed by rapid swelling at higher pressures. However, simulation predicted greater MOF structure volumes relative to experiment for empty or low-pressure conditions. Simulation also predicted dissolution of the structure at 1MPa, a pressure for which experimental results were unavailable. Results from MCMD using the flexible adsorbent model differed significantly from GCMC predictions using a rigid model, indicating that careful selection of model and method are required when simulating complex adsorption behavior.

7.1.3 Carbon Dioxide Storage in Coal

To improve understanding of the molecular processes involved in the storage of carbon dioxide in unmineable coal seams with enhanced coalbed methane recovery, an atomically-realistic, associated, macromolecular model of Upper Freeport bituminous coal was simulated using both molecular dynamics (MD) and a hybrid Gibbs-ensemble-Monte-Carlo/MD method. Simulation conditions spanned a wide range of temperatures and pressures associated with CO_2 storage in unmineable coal seams. Predicted bulk densities for the dry coal structure were within the range of experimentally reported values. The relaxed structures showed evidence of association and stacking of graphitic regions on different macromolecules, which is expected for coals of bituminous rank. Consistent with known coal behavior, carbon dioxide was predicted to adsorb preferentially with respect to methane and induce significant swelling of the structure.

7.2 Suggestions for Future Work

7.2.1 MOF Simulation

Future work should explore how variations in the chemical and nano-structural properties of these engineered MOF adsorbents influence their capacity and selectivity for CO_2 adsorption. Of particular interest will be developing tools to predict and tune the gating behavior. Using predictive computer simulation, the CCS potential of numerous candidate MOF structures could be screened without resorting to costly laboratory synthesis and CO_2 uptake measurements for underperforming adsorbents. For those select adsorbents identified in the theoretical modeling as the most promising candidate materials, experimental sorption measurements could then be performed to validate their superior capabilities for CO_2 capture. Using this simulation-based, materials design approach, new adsorbents can be identified that offer great potential for enhancing energy sustainability through GHG emissions control.

Because MD simulation predicted larger MOF structure volumes relative to experiment for the empty or low-pressure MOF structure, force field improvement may be required to achieve more quantitatively accurate predictions of gating behavior. While tuning of LJ and/or partial charge parameters could likely result in more accurate behavior, capturing specific phenomena associated with, for example, $\pi - \pi$ bonding between aromatic rings and charge transfer may require the implementation of a more complex and computationally expensive force field.

7.2.2 Coal Simulation

Carrying forward from simulations using the associated bituminous coal model described in this work, the study should be extended to investigate and validate in more detail predictions of carbon dioxide and methane adsorption under *in situ* conditions. Direct application of the validated model would use molecular simulations to calculate diffusion coefficients for methane and carbon dioxide within the micropores of the equilibrated and solvated coal macromolecule. As noted earlier, the hindered diffusion of these gases within the coal matrix is hypothesized to be the rate limiting step in the loading and extraction of CO_2 and methane from coal basins. This would serve to generate physical property data would better inform the development of greenhouse gas fate models and engineered designs for the recovery of natural gas from coalbeds and underground storage of CO_2. To further validate the associated bituminous coal model, simulations of nitrogen adsorption at 77 K should

also be computed and compared to experimental isotherms, as N_2 sorption at cryogenic temperatures is commonly used to deduce the specific surface area and pore size distribution of carbonaceous adsorbents.

7.2.3   Hybrid MC/MD Method and Tools

Regarding the hybrid Monte Carlo/molecular dynamics (MCMD) methods used in this work, evolution of the simulated systems was influenced by the number and ratio of MC and MD moves in each cycle. Future work should explore this variation and its role in simulation efficiency and accuracy.

Also, although work with the MCMD method described above has already resulted in enhancements to the open-source Towhee MC simulation package and improved the availability of tools for use with hybrid MC/MD, further improvements are possible. In particular, instead of accepting all MD moves unconditionally, the final configuration resulting from the MD portion of the method could be accepted with a probability consistent with the osmotic thermodynamic ensemble (constant temperature, pressure, and adsorbate chemical potential), which would allow ensemble averaging and more rigorous prediction of thermodynamic properties.

To improve simulation efficiency, reduce overall computational cost, and enhance exploration of phase-space, hybrid MC/MD could be combined with replica-exchange or parallel-tempering methodologies. Using replica-exchange, multiple simulations at slightly different conditions (e.g. temperature) are carried out simultaneously. These simulations periodically attempt to swap configurations according to well-defined acceptance rules. This allows, for example, simulations at lower temperatures to explore regions of phase space that would not otherwise be reached within acceptable computation times due to the presence of local minima in the energy landscape.

To allow the study of complex sorption systems in which chemical reactions play a role, inclusion of reactive Monte Carlo (RMC) within the hybrid MC/MD scheme would permit studying the interplay of reaction and sorption processes. RMC is a Monte Carlo method in which chemical species present in a simulation are interconverted according to specified chemical reactions and well-defined acceptance rules. This enhancement would have direct applicability to the coal system considered here, where CO_2 is in the presence of water and various dissolved ionic mineral species.

Although described in the context of specific carbon dioxide capture and storage systems, hybrid MC/MD methods have the potential for general and high-value applicability throughout the molecular simulation community. There exist many very good, freely-available MD

simulation packages (e.g. LAMMPS, NAMD, Gromacs) and notably fewer MC simulation packages (e.g. MCCCS Towhee). Unfortunately, in spite of the fact that hybrid methods are not new, the author is unaware of any open-source molecular simulation packages capable of general, hybrid simulations. Much of this work regarding hybrid MC/MD results from a desire to rectify this situation.

Appendix

Hybrid MC/MD Code

The following is a listing of the bash script used to link the MCCCS Towhee Monte Carlo simulation package (v6.0) to the DL_POLY molecular dynamics simulation package (v2.19) for implementation of the hybrid MC/MD methods described in the text. The code is capable of handing either grand canonical MC or Gibbs ensemble MC. Other code necessary for hybrid MC/MD has already been implemented in the Towhee codebase. The Towhee package is open-source, free, and licensed under the GPL. At the time of this writing, DL_POLY is available free to academic researchers following registration and acceptance of their license.

```bash
1 #!/bin/bash
2 # This script alternates between towhee and dlpoly runs /
    $LOOPS times.
3 # The user is responsible for ensuring the various input /
    files are correct.
4 # Generally required are: CONTROL, FIELD, towhee_input, and/
    either towhee_coords or towhee_initial
5
6 usage="usage: hmc−wrapper loops [towhee_input_file]"
7 # if towhee_input file is not specified, script looks for "/
    towhee_input_run"
8
9 LOOPS=$1
10 # kludge to make sure LOOPS is a number
11 let "LOOPS += 0"
12
13 # confirm necessary files and other input are available
14 if [ ! −f FIELD ]; then
```

```
15    echo Need valid FIELD file to start
16    exit 1
17 fi
18
19 if [ ! $LOOPS −gt 0 ]; then
20    echo "Invalid number of loops"
21    echo $usage
22    exit 1
23 fi
24
25 if [ −n "$2" ]; then
26    echo "Using $2 for towhee_input−run"
27    cp "$2" towhee_input−run
28 else
29    if [ −f towhee_input−run ]; then
30       echo "Using existing towhee_input−run"
31    else
32       echo "Need existing towhee_input−run or name of /
             towhee_input file"
33       echo $usage
34       exit 1
35    fi
36 fi
37
38 # gather info and prepare for parsing towhee_{initial,final/
    } later
39 nmolty=`grep −i −A 1 "nmolty" towhee_input−run | tail −1`
40 nboxes=`grep −i −A 1 "numboxes" towhee_input−run | tail −1`
41 nboxpairs=$(( nboxes∗(nboxes−1)/2 ))
42 if [ $nboxes −gt $nboxpairs ]; then
43    maxnbox=$nboxes
44 else
45    maxnbox=$nboxpairs
46 fi
47
48 # output initial information and check several things
```

```
49 grep −i −A 1 "nmolty" towhee_input−run
50 grep −i −A 1 "numboxes" towhee_input−run
51
52 if [ 'grep −A 1 linit towhee_input−run | tail −1 | grep T' /
     ]; then
53   echo "linit = true"
54   # number of molecules and unit cell
55   grep −i −A 1 "^initmol" towhee_input−run
56   grep −i −A 30 "^hmatrix" towhee_input−run | grep ^[^#] | /
       head −4
57 else
58   echo "linit = false"
59   if [ −f towhee_initial ]; then
60     cp towhee_initial towhee_initial−start
61     # number of molecules and unit cell
62     echo "initmol"
63     echo "unknown"
64     echo "hmatrix"
65     # assume n=1 box and m=3 molecule types
66     # head −3+(n*m*3)+1+max(n,n(n−1)/2)*3+n*3
67     # tail −n*3
68 #    head −19 towhee_initial | tail −3
69     head −$(( 3 + nboxes*nmolty*3 + 1 + maxnbox*3 + nboxes/
         *3 )) towhee_initial | tail −$(( nboxes*3 ))
70   else
71     echo "Need towhee_initial"
72     exit 1
73   fi
74 fi
75
76 echo "$LOOPS loops started" 'date'
77 # main loop
78 for ((a=1; a <= LOOPS ; a++)); do  # Double parentheses, /
     and "LOOPS" with no "$".
79
80   # pre−run cleanup
```

```
81    cp  FIELD  FIELD−old
82    if  [  −f  CONFIG  ];  then
83      mv  CONFIG  CONFIG−old
84    fi
85    if  [  −f  CONFIG_1  ];  then
86      mv  CONFIG_1  CONFIG_1−old
87    fi
88    if  [  −f  FIELD_1  ];  then
89      mv  FIELD_1  FIELD_1−old
90    fi
91    if  [  −f  towhee_final  ];  then
92      mv  towhee_final  towhee_final−old
93    fi
94    if  [  −f  REVCON  ];  then
95      mv  REVCON  REVCON−old
96    fi
97
98    # run  towhee
99    towhee  towhee_input−run  >&  out−mc−$a.txt  ||  (echo  towhee /
          failed;  rm  core;  exit  1)
100   echo  "towhee  loop  $a  finished"  `date`
101
102   # check  for  successful  towhee  run
103   if  [  !  −f  CONFIG_1  ]  ||  [  `stat  −c%s  CONFIG_1`  =  0  ]; /
          then
104     echo  Problem  finding  CONFIG_1
105     exit  1
106   fi
107   if  [  !  −f  FIELD_1  ]  ||  [  `stat  −c%s  FIELD_1`  =  0  ];  then
108     echo  Problem  finding  FIELD_1
109     exit  1
110   fi
111   if  [  !  −f  towhee_final  ];  then
112     echo  Problem  finding  towhee_final
113     exit  1
114   fi
```

```
115
116    # make sure we're in restart mode for the next run
117    sed -i '/linit/,/initboxtype/ s/T/F/' towhee_input-run
118
119    # output current volumes and number of molecules for /
           posterity
120    grep '^ Volume ' out-mc-$a.txt
121    echo "Molecule counts, one line per box"
122    for name in FIELD_?; do
123      for nummol in 'grep -i "^nummols" $name | awk '{print$2/
             }''; do
124        echo -n $nummol " "
125      done
126      echo
127    done
128
129    # set up next DLPOLY run
130    # create new CONFIG file
131    cp CONFIG_1 CONFIG
132
133    # set new number of molecules in FIELD file
134    for molnum in 'grep -i "^Name\ of\ Molecule" FIELD | awk /
           '{print$4}''
135    do
136      nummol='grep -A 1 "^Name\ of\ Molecule.*$molnum" /
             FIELD_1 | tail -1 | awk '{print$2}''
137      sed -i "/^Name\ of\ Molecule.*$molnum/,/ATOMS/ s//
             NUMMOLS.*/NUMMOLS\ $nummol/" FIELD
138    done
139
140    # run DLPOLY
141    DLPOLY.X >& out-md.txt || (echo dlpoly failed; rm core; /
           exit 1)
142    mv OUTPUT out-md-$a.txt
143    echo "dlpoly loop $a finished" 'date'
144
```

```
145   # check for successful run
146   if [ ! -f REVCON ] || [ `stat -c%s REVCON` = 0 ]; then
147     echo Problem finding REVCON
148     exit 1
149   fi
150   cp REVCON CONFIG_1
151
152   # output unitcell data for posterity
153   for name in CONFIG_?; do
154     echo "final unitcell vectors for" $name
155     head -5 $name | tail -3
156   done
157
158   # set up next towhee run
159   # create towhee_initial
160   # front stuff
161   # assume n=1 box and m=3 molecule types
162   # head -3+(n*m*3)+1+max(n,n(n-1)/2)*3
163   # head -16 towhee_final > towhee_initial
164   head -$(( 3 + nboxes*nmolty*3 + 1 + maxnbox*3 )) /
          towhee_final > towhee_initial
165   # hmatrix
166   for name in CONFIG_?; do
167     head -5 $name | tail -3 >> towhee_initial
168   done
169   # assume n=1 box and m=3 molecule types
170   # head -3+(n*m*3)+1+max(n,n(n-1)/2)*3+n*3+2
171   # middle stuff
172   # head -21 towhee_final | tail -2 >> towhee_initial
173   head -$(( 3 + nboxes*nmolty*3 + 1 + maxnbox*3 + nboxes*3 /
          + 2 )) towhee_final | tail -2 >> towhee_initial
174   # chain molecule type
175   for name in FIELD_?; do
176     molnum=0
177     for nummol in `grep -i "^nummols" $name | awk '{print$2/
          }'`; do
```

```bash
178        (( molnum += 1 ))
179        for (( chain=1; chain <= nummol ; chain++)); do   # /
               Double parentheses , and "nummol" with no "$".
180          echo −n '' $molnum >> towhee_initial
181        done
182      done
183    done
184    echo >> towhee_initial
185    # chain box number
186    boxnum=0
187    for name in FIELD_?; do
188      (( boxnum += 1 ))
189      for nummol in `grep −i "^nummols" $name | awk '{ print$2/
             }'`; do
190        for (( chain=1; chain <= nummol ; chain++)); do   # /
               Double parentheses , and "nummol" with no "$".
191          echo −n '' $boxnum >> towhee_initial
192        done
193      done
194    done
195    echo >> towhee_initial
196    # coordinates
197    for name in CONFIG_?; do
198      tail +2 $name | grep −A 1 ^[A–Za–z] | grep ^[^A–Za–z−] /
             >> towhee_initial
199    done
200  done
201
202 echo "$LOOPS loops finished" `date`
203
204 # save some space from the HISTORY files
205 gzip −dcf HISTORY.gz HISTORY | gzip > HISTORYnew.gz && mv /
      HISTORYnew.gz HISTORY.gz && rm HISTORY
```

Bibliography

1998. Greenhouse Gas Control Technologies, in Pierce Riemer and Alexander Wokaun, (Eds.) *International Conference on Greenhouse Gas Control Technologies*, Elsevier Science Pub Co.

Aaron, D. and C. Tsouris. 2005. Separation of CO2 from flue gas: A review, *Separation Science and Technology*, 40(1-3), 321–348.

Akten, E. D., R. Siriwardane, and D. S. Sholl. 2003. Monte Carlo Simulation of Single- and Binary-Component Adsorption of CO2, N2, and H2 in Zeolite Na-4A, *Energy Fuels*, 17(4), 977–983.

Alavi, S., J. A. Ripmeester, and D. D. Klug. 2005. Molecular-dynamics study of structure II hydrogen clathrates, *Journal of Chemical Physics*, 123(2). Times Cited: 24.

Allen, M. P. and D. J. Tildesley. 1989. *Computer Simulation of Liquids*, Oxford: Oxford University Press.

Audus, H. 1997. Greenhouse gas mitigation technology: An overview of the CO2 capture and sequestration studies and further activities of the IEA Greenhouse Gas R&D Programme, *Energy*, 22(2-3), 217–221.

Aydt, E. M. and R. Hentschke. 2000. Swelling of a model network: A Gibbs-ensemble molecular dynamics study, *Journal Of Chemical Physics*, 112(12), 5480–5487.

Blake, A. J., S. J. Hill, P. Hubberstey, and W. S. Li. 1997. Rectangular grid two-dimensional sheets of copper(II) bridged by both co-ordinated and hydrogen bonded 4,4'-bipyridine (4,4'-bipy) in [Cu(mu-4,4'-bipy)(H2O)(2)(FBF3)(2)]center dot 4,4'-bipy, *Journal of the Chemical Society-Dalton Transactions*, 6, 913–914. 19.

Cao, Dapeng and Jianzhong Wu. 2005. Modeling the selectivity of activated carbons for efficient separation of hydrogen and carbon dioxide, *Carbon*, 43(7), 1364–1370.

Capehart, Barney L. 2007. *Encyclopedia of Energy Engineering and Technology*, CRC Press.

Chue, K. T., J. N. Kim, Y. J. Yoo, S. H. Cho, and R. T. Yang. 1995. COMPARISON OF ACTIVATED CARBON AND ZEOLITE 13X FOR CO2 RECOVERY FROM FLUE-GAS

BY PRESSURE SWING ADSORPTION, *Industrial & Engineering Chemistry Research*, 34(2), 591–598. 9.

Davies, G. M. and N. A. Seaton. 1998. The effect of the choice of pore model on the characterization of the internal structure of microporous carbons using pore size distributions, *Carbon*, 36(10), 1473–1490. Carbon.

Davies, G. M. and N. A. Seaton. 1999. Development and validation of pore structure models for adsorption in activated carbons, *Langmuir*, 15(19), 6263–6276. Langmuir.

Do, D. D., D. Nicholson, and H. D. Do. 2007. Heat of adsorption and density distribution in slit pores with defective walls: GCMC simulation studies and comparison with experimental data, *Applied Surface Science*, 253(13), 5580–5586.

Dombrowski, R. J., D. R. Hyduke, and C. M. Lastoskie. 2000. Pore size analysis of activated carbons from argon and nitrogen porosimetry using density functional theory, *Langmuir*, 16(11), 5041–5050.

Dombrowski, R. J. and C. M. Lastoskie. 2002. A two-stage Horvath-Kawazoe adsorption model, *Studies in Surface Science & Catalysis*, 144, 99–106.

Dombrowski, R. J., C. M. Lastoskie, and D. R. Hyduke. 2001. The Horvath-Kawazoe method revisited, *Colloids and Surfaces a-Physicochemical and Engineering Aspects*, 187, 23–39.

EIA Energy Information Administration, U.S. Department of Energy. 2003. Emissions of Greenhouse Gases in the United States.

Escobedo, F. A. and J. J. de Pablo. 1999. Simulation of swelling of model polymeric gels by subcritical and supercritical solvents, *Journal Of Chemical Physics*, 110(2), 1290–1298.

Faulon, J. L. 1994. Calculating The Number Averaged Molecular-Weight (M(0)) Of Aromatic And Hydroaromatic Clusters In Coal Using Rubber Elasticity Theory, *Energy & Fuels*, 8(5), 1020–1023.

Faulon, J. L., G. A. Carlson, and P. G. Hatcher. 1993. Statistical-Models For Bituminous Coal - A 3-Dimensional Evaluation Of Structural And Physical-Properties Based On Computer-Generated Structures, *Energy & Fuels*, 7(6), 1062–1072.

Fitzgerald, J. E., M. Sudibandriyo, Z. Pan, R. L. Robinson, and K. A. M. Gasem. 2003. Modeling the adsorption of pure gases on coals with the SLD model, *Carbon*, 41(12), 2203–2216.

Freindorf, M. and J. L. Gao. 1996. Optimization of the Lennard-Jones parameters for a combined ab initio quantum mechanical and molecular mechanical potential using the 3-21G basis set, *Journal of Computational Chemistry*, 17(4), 386–395.

Frenkel, D. and B. Smit. 1996. *Understanding Molecular Simulation*, San Diego, CA: Academic Press.

Frisch, M. J., G. W. Trucks, H. B. Schlegel, G. E. Scuseria, M. A. Robb, J. R. Cheeseman, J. A. Montgomery, Jr., T. Vreven, K. N. Kudin, J. C. Burant, J. M. Millam, S. S. Iyengar, J. Tomasi, V. Barone, B. Mennucci, M. Cossi, G. Scalmani, N. Rega, G. A. Petersson, H. Nakatsuji, M. Hada, M. Ehara, K. Toyota, R. Fukuda, J. Hasegawa, M. Ishida, T. Nakajima, Y. Honda, O. Kitao, H. Nakai, M. Klene, X. Li, J. E. Knox, H. P. Hratchian, J. B. Cross, V. Bakken, C. Adamo, J. Jaramillo, R. Gomperts, R. E. Stratmann, O. Yazyev, A. J. Austin, R. Cammi, C. Pomelli, J. W. Ochterski, P. Y. Ayala, K. Morokuma, G. A. Voth, P. Salvador, J. J. Dannenberg, V. G. Zakrzewski, S. Dapprich, A. D. Daniels, M. C. Strain, O. Farkas, D. K. Malick, A. D. Rabuck, K. Raghavachari, J. B. Foresman, J. V. Ortiz, Q. Cui, A. G. Baboul, S. Clifford, J. Cioslowski, B. B. Stefanov, G. Liu, A. Liashenko, P. Piskorz, I. Komaromi, R. L. Martin, D. J. Fox, T. Keith, M. A. Al-Laham, C. Y. Peng, A. Nanayakkara, M. Challacombe, P. M. W. Gill, B. Johnson, W. Chen, M. W. Wong, C. Gonzalez, and J. A. Pople. 2003. Gaussian 03, Revision C.02. Gaussian, Inc., Wallingford, CT, 2004.

Gallo, M., T. M. Nenoff, and M. C. Mitchell. 2006. Selectivities for binary mixtures of hydrogen/methane and hydrogen/carbon dioxide in silicalite and ETS-10 by Grand Canonical Monte Carlo techniques, *Fluid Phase Equilibria*, 247(1-2), 135–142. Times Cited: 2.

Garberoglio, G., A. I. Skoulidas, and J. K. Johnson. 2005. Adsorption of gases in metal organic materials: Comparison of simulations and experiments, *Journal Of Physical Chemistry B*, 109(27), 13094–13103.

Goj, A., D. S. Sholl, E. D. Akten, and D. Kohen. 2002. Atomistic Simulations of CO2 and N2 Adsorption in Silica Zeolites: The Impact of Pore Size and Shape, *J. Phys. Chem. B*, 106(33), 8367–8375.

Goodman, A. L., A. Busch, G. J. Duffy, J. E. Fitzgerald, K. A. M. Gasem, Y. Gensterblum, B. M. Krooss, J. Levy, E. Ozdemir, Z. Pan, R. L. Robinson, K. Schroeder, M. Sudibandriyo, and C. M. White. 2004. An inter-laboratory comparison of CO2 isotherms measured on argonne premium coal samples, *Energy & Fuels*, 18(4), 1175–1182.

Gunter, W. D., T. Gentzis, B. A. Rottenfusser, and R. J. H. Richardson. 1997. Deep coalbed methane in Alberta, Canada: A fuel resource with the potential of zero greenhouse gas emissions, *Energy Conv. Manag.*, 38, S217–S222–.

Herzog, H. 2001. What future for carbon capture and sequestration?, *Environmental Science & Technology*, 35(7), 148A–153A. 12 AMER CHEMICAL SOC.

Heuchel, M., G. M. Davies, E. Buss, and N. A. Seaton. 1999. Adsorption of carbon dioxide and methane and their mixtures on an activated carbon: Simulation and experiment, *Langmuir*, 15(25), 8695–8705. Langmuir.

Hitchon, B., W. D. Gunter, T. Gentzis, and R. T. Bailey. 1999. Sedimentary basins and greenhouse gases: a serendipitous association, *Energy Conversion and Management*, 40(8), 825–843. Energy Conv. Manag.

Houghton, J.T., Y. Ding, D. J. Griggs, M. Noguer, P. J. van der Linden, X. Dai, K. Maskell, and C.A. Johnson, (Eds.) . 2001. *Climate Change 2001: The Scientific Basis. Contribution of Working Group 1 to the Third Assessment Report of the Intergovernmental Panel on Climate Change*, Cambridge: Cambridge University Press.

Jorgensen, W. L., J. Chandrasekhar, J. D. Madura, R. W. Impey, and M. L. Klein. 1983. Comparison of simple potential functions for simulating liquid water, *J. Chem. Phys.*, 79, 926–935.

Karacan, C. O. 2003. An effective method for resolving spatial distribution of adsorption kinetics in heterogeneous porous media: application for carbon dioxide sequestration in coal, *Chemical Engineering Science*, 58(20), 4681–4693.

Karacan, C. O. and G. D. Mitchell. 2003. Behavior and effect of different coal microlithotypes during gas transport for carbon dioxide sequestration into coal seams, *International Journal Of Coal Geology*, 53(4), 201–217.

Kenkare, N. R., C. K. Hall, and S. A. Khan. 2000. Theory and simulation of the swelling of polymer gels, *Journal Of Chemical Physics*, 113(1), 404–418.

Kondo, A., H. Noguchi, S. Ohnishi, H. Kajiro, A. Tohdoh, Y. Hattori, W. C. Xu, H. Tanaka, H. Kanoh, and K. Kaneko. 2006. Novel Expansion/Shrinkage Modulation of 2D Layered MOF Triggered by Clathrate Formation with CO2 Molecules, *Nano Lett.*, 6(11), 2581–2584.

Kotelyanskii, M. J. and R. Hentschke. 1995. GIBBS-ENSEMBLE MOLECULAR-DYNAMICS - LIQUID-GAS EQUILIBRIUM IN A LENNARD-JONES SYSTEM, *Physical Review E*, 51(5), 5116–5119. 17 Part B.

Krooss, B. M., F. van Bergen, Y. Gensterblum, N. Siemons, H. J. M. Pagnier, and P. David. 2002. High-pressure methane and carbon dioxide adsorption on dry and moisture-equilibrated Pennsylvanian coals, *International Journal Of Coal Geology*, 51(2), 69–92.

Larsen, J. W., R. A. Flowers, P. J. Hall, and G. Carlson. 1997. Structural rearrangement of strained coals, *Energy & Fuels*, 11(5), 998–1002.

Lastoskie, C., K. E. Gubbins, and N. Quirke. 1993a. PORE-SIZE DISTRIBUTION ANALYSIS OF MICROPOROUS CARBONS - A DENSITY-FUNCTIONAL THEORY APPROACH, *Journal of Physical Chemistry*, 97(18), 4786–4796.

Lastoskie, C., K. E. Gubbins, and N. Quirke. 1993b. PORE-SIZE HETEROGENEITY AND THE CARBON SLIT PORE - A DENSITY-FUNCTIONAL THEORY MODEL, *Langmuir*, 9(10), 2693–2702.

Lastoskie, C., K. E. Gubbins, and N. Quirke. 1994. Pore size distribution analysis and networking studies of microporous sorbents, *Studies in Surface Science & Catalysis*, 87, 51–60.

Lastoskie, C. M. 2000. A modified Horvath-Kawazoe method for micropore size analysis, *Studies in Surface Science & Catalysis*, 128, 475–484.

Lastoskie, C. M. and K. E. Gubbins. 2000. Characterization of porous materials using density functional theory and molecular simulation, *Studies in Surface Science & Catalysis*, 128, 41–50.

Lastoskie, C. M., N. Quirke, and K. E. Gubbins. 1997. Structure of porous adsorbents: Analysis using density functional theory and molecular simulation, *Studies in Surface Science & Catalysis*, 104, 745–775.

Lastoskie, C.M. and K.E. Gubbins. 2001. Characterization of porous materials using molecular theory and simulation, *Advances in Chemical Engineering*, 28, 203–250–.

Lemmon, E.W., M.O. McLinden, and D.G. Friend. 2005. Thermophysical properties of fluid systems, in P.J. Linstrom Mallard and W.G., (Eds.) *NIST chemistry webbook*, Gaithersburg, MD: National Institute of Standards and Technology, vol. NIST standard reference database number 69.

Li, D. and K. Kaneko. 2001. Hydrogen bond-regulated microporous nature of copper complex-assembled microcrystals, *Chemical Physics Letters*, 335(1-2), 50–56.

Lu, L., V. Sahajwalla, C. Kong, and D. Harris. 2001. Quantitative X-ray diffraction analysis and its application to various coals, *Carbon*, 39(12), 1821–1833.

Mahajan, O.P. 1991. *Carbon*, 29, 735–742.

Martin, M. G. and J. I. Siepmann. 1999. Novel configurational-bias Monte Carlo method for branched molecules. Transferable potentials for phase equilibria. 2. united-atom description of branched alkanes, *J. Phys. Chem. B*, 103, 4508–4517.

Marzec, A. 2002. Towards an understanding of the coal structure: a review, *Fuel Processing Technology*, 77, 25–32. Sp. Iss. SI.

Mastalerz, M., H. Gluskoter, and J. Rupp. 2004. Carbon dioxide and methane sorption in high volatile bituminous coals from Indiana, USA, *International Journal Of Coal Geology*, 60(1), 43–55.

Mayo, S. L., B. D. Olafson, and W. A. Goddard. 1990. Dreiding - A Generic Force-Field For Molecular Simulations, *Journal Of Physical Chemistry*, 94(26), 8897–8909.

Metz, B., O. Davidson, H. Coninck, M. Loos, and L. Meyer, (Eds.) . 2005. *IPCC Special Report on Carbon dioxide Capture and Storage*, Cambridge: Cambridge University Press.

Milewska-Duda, J., J. Duda, A. Nodzenski, and J. Lakatos. 2000. Absorption and adsorption of methane and carbon dioxide in hard coal and active carbon, *Langmuir*, 16(12), 5458–5466.

Millward, A. R. and O. M. Yaghi. 2005. Metal-organic frameworks with exceptionally high capacity for storage of carbon dioxide at room temperature, *Journal Of The American Chemical Society*, 127(51), 17998–17999.

Myers, A. L. and J. M. Prausnitz. 1965. Thermodynamics of mixed-gas adsorption, *AIChE Journal*, 11(1), 121–127. 10.1002/aic.690110125.

Nicholson, D. and N. G. Parsonage. 1982. *Computer Simulation and the Statistical Mechanics of Adsorption*, London: Academic Press.

Noguchi, H., A. Kondoh, Y. Hattori, H. Kanoh, H. Kajiro, and K. Kaneko. 2005. Clathrate-formation mediated adsorption of methane on Cu-complex crystals, *Journal Of Physical Chemistry B*, 109(29), 13851–13853.

Ohba, T., Y. Inaguma, A. Kondo, H. Kanoh, H. Noguchi, K. E. Gubbins, H. Kajiro, and K. Kaneko. 2006. GCMC simulations of dynamic structural change of Cu-organic crystals with N-2 adsorption, *Journal of Experimental Nanoscience*, 1(1), 91–95. Ohba, T. Inaguma, Y. Kondo, A. Kanoh, H. Noguchi, H. Gubbins, K. E. Kajiro, H. Kaneko, K.

Onishi, S., T. Ohmori, T. Ohkubo, H. Noguchi, L. Di, Y. Hanzawa, H. Kanoh, and K. Kaneko. 2002. Hydrogen-bond change-associated gas adsorption in inorganic-organic hybrid microporous crystals, *Applied Surface Science*, 196(1-4), 81–88.

Oyen, E. and R. Hentschke. 2005. Computer simulation of polymer networks: Swelling by binary Lennard-Jones mixtures, *Journal Of Chemical Physics*, 123(5). 054902.

Ozdemir, E., B. I. Morsi, and K. Schroeder. 2003. Importance of volume effects to adsorption isotherms of carbon dioxide on coals, *Langmuir*, 19(23), 9764–9773.

Panagiotopoulos, A. Z. 1987. Direct determination of phase coexistence properties of fluids by Monte Carlo simulation in a new ensemble, *Molecular Physics*, 61, 813–826.

Pashin, J. C. and M. R. McIntyre. 2003. Temperature-pressure conditions in coalbed methane reservoirs of the Black Warrior basin: implications for carbon sequestration and enhanced coalbed methane recovery, *International Journal of Coal Geology*, 54(3-4), 167–183. Int. J. Coal Geol.

Pashin, J.C., R.H. Groshong Jr., and R.E Carroll. 2001. Carbon sequestration potential of coalbed methane reservoirs in the Black Warrior basin: a preliminary look, in *Int. Coalbed Methane Symp. Proc.*, Tuscaloosa, AL, 5162–.

Pikunic, J., C. Clinard, N. Cohaut, K. E. Gubbins, J. M. Guet, R. J. M. Pellenq, I. Rannou, and J. N. Rouzaud. 2003. Structural Modeling of porous carbons: Constrained reverse Monte Carlo method, *Langmuir*, 19(20), 8565–8582. Langmuir.

Pikunic, J., C.M. Lastoskie, and K.E. Gubbins. 2002. Molecular modeling of adsorption from the gas phase, in F. Schth, K.S.W. Sing, and J. Weitkamp, (Eds.) *Handbook of Porous Solids*, Weinheim: Wiley-VCH, 182–236.

Potoff, JJ and JI Siepmann. 2001. Vapor-liquid equilibria of mixtures containing alkanes, carbon dioxide, and nitrogen, *AICHE JOURNAL*, 47(7), 1676–1682. Cited References Count:34.

Quirke, N. and S. R. R. Tennison. 1996. The interpretation of pore size distributions of microporous carbons, *Carbon*, 34(10), 1281–1286. Carbon.

Ramanathan, C. and M. Bencsik. 2001. Measuring spatially resolved gas transport and adsorption in coal using MRI, *Magnetic Resonance Imaging*, 19(3-4), 555–559.

Ravikovitch, P. I., A. Vishnyakov, R. Russo, and A. V. Neimark. 2000. Unified approach to pore size characterization of microporous carbonaceous materials from N-2, Ar, and CO2 adsorption isotherms, *Langmuir*, 16(5), 2311–2320. Langmuir.

Remner, D.J., T. Ertekin, and G.R. King. 1984. A parametric study of the effects of coal seam properties on gas drainage efficiency, in *Proceedings of the SPE Eastern Regional Meeting, Charleston, WV*. Paper SPE 13366.

Samios, S., A. K. Stubos, G. K. Papadopoulos, N. K. Kanellopoulos, and F. Rigas. 2000. The structure of adsorbed CO2 in slitlike micropores at low and high temperature and the resulting micropore size distribution based on GCMC simulations, *Journal of Colloid and Interface Science*, 224(2), 272–290. J. Colloid Interface Sci.

Sams, W.N., G. Bromhal, S. Jikich, T. Ertekin, and D.H. Smith. 2005. Field-project designs for carbon dioxide sequestration and enhanced coalbed methane production, *Energy & Fuels*, 19, 2287–2297.

Schoen, M. 2002. Capillary condensation between mesocopically rough surfaces, *Colloids and Surfaces a-Physicochemical and Engineering Aspects*, 206(1-3), 253–266. Colloid Surf. A-Physicochem. Eng. Asp.

Silvera, I. F. and V. V. Goldman. 1978. The isotropic intermolecular potential for H2 and D2 in the solid and gas phases, *J. Chem. Phys.*, 69(9), 4209.

Sircar, S., T. C. Golden, and M. B. Rao. 1996. Activated carbon for gas separation and storage, *Carbon*, 34(1), 1–12. Times Cited: 84.

Siriwardane, R., M. Shen, E. Fisher, J. Poston, and A. Shamsi. ???? Adsorption and Desporption of CO2 on Solid Sorbents, Tech. rep., National Energy Technology Laboratory.

Steele, W.A. 1974. *The interaction of gases with solid surfaces*, New York, NY: Pergamon.

Sweatman, M. B. and N. Quirke. 2001. Characterization of porous materials by gas adsorption: Comparison of nitrogen at 77 K and carbon dioxide at 298 K for activated carbon, *Langmuir*, 17(16), 5011–5020. Langmuir.

Takanohashi, T. and H. Kawashima. 2002. Construction of a model structure for upper freeport coal using C-13 NMR chemical shift calculations, *Energy & Fuels*, 16(2), 379–387.

Takanohashi, T., K. Nakamura, and M. Iino. 1999. Computer simulation of methanol swelling of coal molecules, *Energy & Fuels*, 13(4), 922–926.

Takanohashi, T., K. Nakamura, Y. Terao, and M. Iino. 2000. Computer simulation of solvent swelling of coal molecules: Effect of different solvents, *Energy & Fuels*, 14(2), 393–399.

Tsotsis, T. T., H. Patel, B. F. Najafi, D. Racherla, M. A. Knackstedt, and M. Sahimi. 2004. Overview of laboratory and modeling studies of carbon dioxide sequestration in coal beds, *Industrial & Engineering Chemistry Research*, 43(12), 2887–2901.

van Tassel, Paul R., H. Ted Davis, and Alon V. McCormick. 1994. Adsorption Simulations of Small Molecules and Their Mixtures in a Zeolite Micropore, *Langmuir*, 10(4), 1257–1267.

Vishnyakov, A., E. M. Piotrovskaya, and E. N. Brodskaya. 1998. Capillary condensation and melting/freezing transitions for methane in slit coal pores, *Adsorption-Journal Of The International Adsorption Society*, 4(3-4), 207–224.

Vuong, T. and P. A. Monson. 1996. Monte Carlo simulation studies of heats of adsorption in heterogeneous solids, *Langmuir*, 12(22), 5425–5432. 38.

White, C. M., D. H. Smith, K. L. Jones, A. L. Goodman, S. A. Jikich, R. B. LaCount, S. B. DuBose, E. Ozdemir, B. I. Morsi, and K. T. Schroeder. 2005. Sequestration of carbon dioxide in coal with enhanced coalbed methane recovery - A review, *Energy & Fuels*, 19(3), 659–724.

Yang, Q. and C. Zhong. 2006. Molecular Simulation of Carbon Dioxide/Methane/Hydrogen Mixture Adsorption in Metal-Organic Frameworks, *J. Phys. Chem. B*, 110(36), 17776–17783.